

## REPORT DOCUMENTATION PAGE

AFRL-SR-BL-TR-01-

ources,  
of this  
erson

NOV 13 2001

**Final Report**

**on**

**Effect of Damage Processes on Spallation Life in Thermal Barrier Coatings**

*(AFOSR Grant # F49620-98-1-0390 ; Program Monitor – Dr. H. Thomas Hahn)*

**by**

**Golam Newaz (PI)  
Professor of Mechanical Engineering  
5050 Anthony Wayne Drive  
Wayne State University  
Detroit, Michigan 48202**

**(Tel: 313-577-3877; Fax: 313-577-8789; e-mail: gnewaz@eng.wayne.edu)**

**November 9, 2001**

## **ACKNOWLEDGMENTS**

Funding for this research was provided through a grant (# F49620-98-1-0390) from the Air Force of Scientific Research (AFOSR). Dr. H. Thomas Hahn was the program monitor. Discussion and interaction with Dr. P. K. Wright of General Electric Aircraft Engines (GEAE) are gratefully acknowledged.

## TABLE OF CONTENTS

<b>ACKNOWLEDGMENTS .....</b>	<b>ii</b>
<b>ABSTARCT</b>	<b>vi</b>
<b>1. INTRODUCTION .....</b>	<b>1</b>
1.1 GENERAL REMARKS .....	1
1.2 MATERIALS OF THERMAL BARRIER COATINGS.....	2
1.3 MANUFACTURING PROCESS OF THERMAL BARRIER COATINGS .....	4
1.4 OXIDATION OF BOND COAT (NI-AL SYSTEM) .....	7
1.5 DIFFUSION OF METALS .....	9
1.6 FAILURE MECHANISMS .....	11
1.7 OBJECTIVES .....	14
<b>2. EXPERIMENTAL ASPECTS .....</b>	<b>22</b>
2.1 SPECIMEN PREPARATION .....	22
2.2 THERMAL TEST .....	23
2.3 MATERIAL CHARACTERIZATIONS .....	23
<b>3 RESIDUAL STRESS ANALYSIS IN THERMAL BARRIER COATINGS .....</b>	<b>29</b>
3.1 RESIDUAL STRESS AND STRAIN ANALYTICAL BASED ON AN ELASTIC MODEL .....	29
3.2 DIGITAL SPECKLE CORRELATION .....	31
3.3 FINITE ELEMENT ANALYSIS .....	32
3.4 RESULTS .....	32
3.5 SUMMARY .....	34

<b>STRUCTURE CHANGE OF BOND COAT LAYER AND ITS EFFECTS</b>	
<b>4.1 EXPERIMENTAL ASPECTS</b>	43
<b>4.2 RESULTS AND DISCUSSION</b>	44
<b>4.3 SUMMARY</b>	50
<b>5 PROGRESSIVE DAMAGE EVOLUTION IN THERMAL BARRIER COATINGS</b>	64
<b>5.1 EXPERIMENTAL ASPECTS</b>	64
<b>5.2 RESULTS</b>	65
<b>5.3 DISCUSSION</b>	68
<b>5.4 SUMMARY</b>	72
<b>6 NONDESTRUCTIVE EVALUATION</b>	89
<b>6.1 PRINCIPLE OF THERMAL WAVE IMAGING</b>	89
<b>6.2 THERMAL CONTACT RESISTANCE CONCEPT IN BI-MATERIAL</b>	91
<b>6.3 EXPERIMENTAL ASPECTS</b>	93
<b>6.4 RESULTS AND DISCUSSION</b>	94
<b>6.5 SUMMARY</b>	98
<b>7 FAILURE MODES AND VACUUM HEAT TREATMENT TO IMPROVE PERFORMANCE OF THERMAL BARRIER COATINGS</b>	113
<b>7.1 EXPERIMENTAL PROCEDURE</b>	113
<b>7.2 RESULTS AND DISCUSSION</b>	114
<b>7.3 SUMMARY</b>	120
<b>8 SUMMARY AND CONCLUSIONS</b>	129

8.1 SUMMARY .....	129
<b>REFERENCES .....</b>	<b>132</b>

## ABSTRACT

Thermal barrier coatings (TBCs) provide thermal insulation to high temperature superalloys. TBCs consist of an outer ceramic layer that provides good thermal insulation due to the low thermal conductivity of the ceramic used, and the inner metallic bond coat layer that provides needed oxidation resistance to the underlying superalloy. The microstructure of the bond coat changed from high aluminum concentration  $\beta$ -(Ni, Pt)Al phase, which has a very good oxidation resistance, to  $\beta$ -(Ni, Pt)Al plus  $\gamma'$ -(Ni, Pt)<sub>3</sub>Al dual phase microstructure due to oxidation and interdiffusion between the bond coat and the substrate during the thermal test in air. The microstructure change influenced the oxidation behaviors of the bond coat. Less protective oxide (Ni-rich) formed on  $\gamma'$ -(Ni, Pt)<sub>3</sub>Al due to depletion of aluminum, and the oxide scale on  $\gamma'$ -(Ni, Pt)<sub>3</sub>Al had less adhesion to the bond coat.

The TGO layer and bond coat was subjected to high residual radial stresses during cool down from oxidation temperature due to the thermal expansion mismatch between the different layers. The high residual stress initiated the damages in TGO layer, the TBC/TGO interface and the TGO/bond coat interface as well. The evolution of the damages in TBCs resulted in local loss in adhesion of the coating during thermal cycling. The formation and evolution of micro-decohesion was the key failure mechanism of TBC for long term thermal cycling. Thermal wave imaging technique as non-destructive and non-contact method was successfully used to monitor the health of TBC. The results reveal that there was no major delamination in TBC specimens during thermal tests.

instead of increase of thermal signal amplitude of TBCs with number of cycles. Buckling and spalling processes were final events at thermal tests and did not control the lifetime of TBC.

Thermal wave imaging technique as non-destructive and non-contact method was successfully used to monitor the health of TBC. The results reveal that there was no major delamination in TBC specimens during thermal tests, instead of increase of thermal signal amplitude of TBCs with number of cycles. When the increase of the thermal signal amplitude tended to be very slow i.e., when saturation is reached, it indicated TBC was close to failure. Thus, thermal wave imaging can be a reliable NDE technique for assessment of life of TBCs. The increase of the thermal signal amplitude contributed to an increase of thermal contact resistance in the TBC system, which was induced by micro-decohesions at interfaces. The TBC finally failed by buckling and spalling. However, buckling, buckle propagation and spalling performed in very short time compared to the whole lifetime of TBC. It was proposed that the buckling and spalling processes were final events at thermal tests and did not control the lifetime of TBC. The formation and evolution of micro-decohesion was the key failure mechanism of TBC for long term thermal cycling.

leads to a better thermal fatigue capability. Soechting (1995) presents a comparison of the uncoated and coated transient thermal response during rapid engine acceleration transients. Designing with a TBC for its full thermal insulating benefit requires a very high degree of confidence since loss of the TBC could result in rapid component degradation. The payoff in increased engine thrust or fuel efficiency is significant and therefore much effort is currently being focused on improvements in the reliability of TBC. Additional efforts are being expended to further the understanding of the behavior of TBC.

## **1.2 MATERIALS OF THERMAL BARRIER COATINGS**

A typical thermal barrier coating system consists of a ceramic topcoat and a metallic bond coat.

### **1.2.1 THERMAL BARRIER COATING**

It was recognized early on that to be useful as a high temperature thermal barrier coating a material must meet these fundamental requirements: (1) high melting point; (2) low density; (3) high surface emissivity; (4) high thermal shock resistance; (low vapor pressure; (6) resistance to oxidation or chemical environment; (7) low thermal conductivity; (8) high coefficient of thermal expansion; and (9) resistance to gaseous and particulate erosion. (Jones, 1996). When these requisites are all considered, very few ceramics are found that meet the criteria. The best is zirconium dioxide which is

outstanding in terms of low thermal conductivity and has the highest coefficient of thermal expansion (CTE) of all the common ceramic oxides (except for MgO), with a CTE about  $\sim 11 \times 10^{-6} \text{K}^{-1}$  at 1000 °C.

Although  $\text{ZrO}_2$  has many properties well suited for thermal barrier use, pure  $\text{ZrO}_2$  transforms from the monoclinic to tetragonal phase at about 1180 °C, and from the tetragonal to cubic phase at about 2370 °C. The harmful effect of the phase transformations is that a contraction in volume. This change of volume causes damage of the coating during thermal cycling. Recent investigations (Jones, 1996) have shown that the addition of  $\text{Y}_2\text{O}_3$  can stabilize  $\text{ZrO}_2$  in its high temperature. The optimum content of  $\text{Y}_2\text{O}_3$  is 6-8 wt.%.

### 1.2.2 Bond Coat

Zirconia thermal barriers are permeable to oxygen at high temperature, and must therefore be backed by an oxidation-resistant bond coat. The choice of the bond coat has been found to be as critical as the choice of the zirconia outer coating in determining the success of the TBC. It was earlier thought that the bond coat should be of low strength so as to relieve stress resulting from the difference in the coefficients of thermal expansion for the zirconia ceramic and the superalloy substrate. However, current results suggest that strengthened bond coats with great creep resistance may be the routes to improved thermal cycle life.

Two general types of bond coat have been used: overlaid MCrAlY, where M is typically Ni or NiCo, and diffusion aluminide (or Pt-aluminide). The first coating is

alumina-spraying directly on to the component, while the second is formed by diffusion of aluminum into the alloy substrate ( Parks et. al. 1995).

The fundamental function of the bond coat layer is to provide a good oxidation resistance and to form an adhesive alumina domain oxide film between the top layer and the bond coat layer. The ability of the bond coat to continue to support the growth of an adhesive alumina scale depends on the total amount of aluminum available; the effective reservoir of aluminum in the bond coat is depleted not only by consumption by the growth of the alumina scale but also by diffusion into the alloy substrate. If a point is reached where the aluminum level of the bond coat falls below that at which alumina can be formed preferentially, oxides of the other constituents of the bond coat will form, and the adherence of the TBC could be significantly degraded.

### **1.3 MANUFACTURING PROCESS OF THERMAL BARRIER COATINGS**

Several coating methods for ceramic coat are available. Plasma spray and electron-beam physical vapor deposition (EB-PVD) processes are popular for their various advantages.

### 1.3.1 PLASMA SPRAY DEPOSITION

Plasma spray deposition is widely used in the coating industry. A schematic diagram of a plasma spraying process is shown in figure 1.2. A DC arc is struck (using typically on the order of 30 V and 300-800A) between the cathode and anode to generate a plasma in the carrier gas, which is usually a mixture of Ar plus H<sub>2</sub> or H<sub>2</sub> and N<sub>2</sub>. Heat is transferred from the plasma to melt the particles of the injected powdered material. Velocity of the plasma can be as high as the order of 200—600 m/s. The plasma spray powder particles are accelerated by the high velocity plasma and then impacted on the surface of the component to build up the coating

Plasma-spray factors associated with the degree of particle melting and subsequent particle velocity include the particle size and feed rate, plasma gas composition, electric current strength, and standoff distance to the component. The section of specific coating parameters depends on the material being sprayed, microstructural requirements, and the equipment design.

The mechanical interlocking of the ceramic and metallic layers is the initial adhesion mechanism. Thus, a properly applied TBC system has a bond coat/zirconia interface with a high roughness. This interface provides a tortuous path for cracks to follow, and cracks are forced to propagate within the ceramic layer (Strangman, 1987).

### 1.3.2 ELECTRON BEAM-PHYSICAL VAPOR DEPOSITION (EB-PVD)

EB-PVD has been successfully used to coat turbine airfoils. Figure 1.3 shows the schematic drawing of an EB-PVD process. This method is a modification of the high-rate vapor deposition process for metallic coatings that has been successfully used to coat turbine airfoils. The power to evaporate the ceramic coating material is provided by a high-energy electron beam gun. Oxygen is also bled into the yttria-stabilized zirconia vapor cloud to minimize any deviations from stoichiometry during coating. This process feature is required since zirconia becomes somewhat oxygen deficient due to partial dissociation during evaporation in a vacuum. Vapor from this cloud condenses onto the turbine airfoil to form the coating. Feeders, electron beam gun, temperature, and gas should be controlled very carefully (Unal et al, 1994, Rigney et al, 1995).

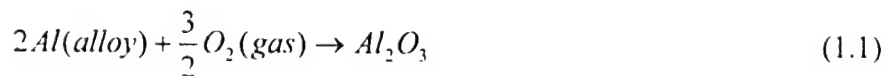
For best adhesion, the bond coat surface should be smooth, or preferably polished, in contrast to plasma sprayed TBCs, which require a rough bond coat. The adhesion of EB-PVD thermal barrier coatings involves a chemical bond coat between the zirconia and bond coat surfaces. High deposition temperatures in the 870 °C to 1090 °C range are typically used to achieve the required bond quality. A clean surface that is free of absorbed gases (e.g., water vapor) and loose oxides is also required to obtain an adequate ceramic-to-metal bond during coating.

The microstructure of EB-PVD ceramic is fundamentally different from that of plasma sprayed ceramic. As shown in figure 1.4 the EB-PVD ceramic grows in columnar form when processed under the appropriate conditions. Ideally, individual ceramic columns are poorly bonded to adjacent columns but are tightly bonded to the underlying

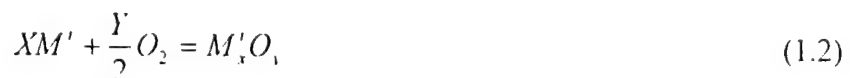
bond coat. This columnar structure is highly tolerant of thermal strains induced by differential expansion of the underlying substrate. The columnar structure of ceramic produced by EB-PVD can significantly improve thermal spallation life of TBCs (Meier, 1991).

#### 1.4 OXIDATION OF BOND COAT (NI-AL SYSTEM)

The development of continuous  $\text{Al}_2\text{O}_3$  scales on bond coat is an extremely effective approach to obtain high temperature oxidation resistance. One of the most effective methods to develop oxidation resistance in alloys and coatings at high temperatures above 900 °C is to form continuous scales of  $\alpha$ -  $\text{Al}_2\text{O}_3$  via selective oxidation. Transport of reactants, namely aluminum and oxygen, through  $\alpha$ -  $\text{Al}_2\text{O}_3$  is slow compared to transport through most other oxides (Doychak, 1994). In order for a  $\alpha$ -  $\text{Al}_2\text{O}_3$  scale to form the thermodynamic conditions must be such that the following reaction is favorable on the surface of the alloy:



When an alloy containing a number of elements,  $M'$ , is exposed to oxygen at elevated temperature, it must initially be determined which element in the alloy will react with the oxygen to form products  $M'_x\text{O}_y$ . This inquiry may be addressed in equations such as the following (Birks et. al., 1987)



With the equilibrium conditions defined by

$$K = \frac{^aM_x^iO_y}{^aM_x^i} P_{O_2} \frac{Y}{2} \quad (1.3)$$

Where K is the equilibrium constant for the reaction,  $^aM_x^iO_y$  and  $^aM_x^i$  are the activities of  $M_x^iO_y$  and  $M_x^i$ , respectively, and  $P_{O_2}$  is the pressure of oxygen required to form the oxide on the alloy containing  $M^i$ . The value of K can be obtained from the standard free energy of formation of the oxide  $M_x^iO_y$

$$K = \exp[-\Delta G^0 M_x^iO_y / RT] \quad (1.4)$$

Wagner (1959) proposed that a critical mole fraction of the more reactive solute phase B in AB solid solution is required before a complete external oxide scale can form. The critical mole fraction,  $N^*$ , is given by:

$$N^* = \left( \frac{\pi g N_0 D_0 V_m}{2 \nu D_B V_{ox}} \right)^{1/2} \quad (1.5)$$

Where  $N_0 D_0$  is the oxygen permeability in the alloy,  $D_B$  is the diffusivity of B in the alloy,  $g$  is a factor related to the volume fraction of internal oxide precipitates required for transition from internal to external oxidation,  $V_m$  and  $V_{ox}$  are the molar volumes of alloy and oxide, respectively, and  $\nu$  is the stoichiometry factor in a  $BO_\nu$  oxide. B is Aluminum and A is nickel in Ni-Al system.

Oxidation of nickel-aluminum alloys at temperature between 900 and 1300 °C was extensively studied by Pettit (1967). He obtained an oxide phase map that indicates the predominant external scales to form over the Ni-Al alloys as a function of temperature and composition (figure 1.5). The map indicates that  $Al_2O_3$  forms readily over the majority of the alloys within the binary Ni-Al system, with the cut-off to a mixed  $NiO$ -

$\text{Al}_2\text{O}_3$  external scale being approximately 25 at. % Al for temperatures below approximately 1200 °C. This implies that  $N^*$  (from equation 1.5) to form external  $\text{Al}_2\text{O}_3$  is approximately 0.25 at elevated temperatures and ambient oxygen partial pressures. The shaded bands indicate the ranges of variation observed in the transition from  $\text{Al}_2\text{O}_3$  to mixed  $\text{NiO- Al}_2\text{O}_3$  external scales and from mixed  $\text{NiO- Al}_2\text{O}_3$  to  $\text{NiO}$  external scales.

Oxidation reactions of protective oxide scales generally follow a parabolic rate equation given by Smallman, 1985

$$x^2 = k_p t \quad (1.6)$$

Where  $x$  is scale thickness,  $t$  is time, and  $k_p$  the parabolic-growth-rate constant in dimensions of length<sup>2</sup>/time. Wagner (1959) has shown that the oxidation process is a thermally activated process and the rate constant  $k_p$  equate

$$k_p = k_0 \exp[-Q/RT] \quad (1.7)$$

where  $Q$  is the activation energy for rate controlling diffusion process.  $T$  is temperature,  $R$  is universal gas constant.

## 1.5 DIFFUSION OF METALS

### 1.5.1 DIFFUSION LAWS

If a bar of an alloy, along which there is a concentration gradient, is heated at a temperature where atomic migration is fast, i.e. near the melting point, the solute atoms are redistributed until the bar becomes uniform in composition. For a an ideal solid solution, Fick's first law of diffusion can be applied as

$$J_x = -D(dc/dx) \quad (1.8)$$

Where  $J_x$  is the flux of diffusing atoms, D is the diffusivity,  $dc/dx$  is concentration gradient of diffusing atoms.

For self-diffusion where no complications exist, the diffusivity is given by

$$D = D_0 \exp[-Q/RT] \quad (1.9)$$

where Q is the activation energy for self-diffusion.

Fick's second law of diffusion is used to described a non-stationary diffusion in which the concentration at a point changes with time,

$$\frac{dc}{dt} = -\frac{dJ_x}{dx} = \frac{d}{dx}(D \frac{dc}{dx}) \quad (1.10)$$

When D is independent of concentration, it can be written as

$$\frac{dc}{dt} = -D \frac{d^2c}{dx^2} \quad (1.11)$$

Fick's second law is the basic equation for the experimental study of isothermal diffusion. Solutions of this second-order partial differential equation have been derived corresponding to the boundary conditions found in many types of diffusion samples (Hill, 1973).

### 1.5.2 THE KIRKENDALL EFFECT OF INTERDIFFUSION

A pure metal A and pure metal B are welded together to form a diffusion couple. When the diffusion couple is heated to a high temperature for diffusing, the interface of the diffusion couple moves during the diffusion process. The nature of this movement is shown in figure 1.6, where the (A) figure represents the diffusion couple before the

ment, and the (B) figure represents the same bar after diffusion has occurred. The latter figure shows that the interface has moved to the right through the bar. The distance has been found to vary as the square root of the time during which the specimen was maintained at the diffusion temperature. The first experiment was performed by Smigelskas and Kirkendall (Smigelskas and Kirkendall, 1947). The Kirkendall experiment demonstrates that the velocity at which the two types of atoms of a binary solution diffuse is not the same. Experimental measurements have shown that the element with the lower melting point diffuses fast (Hill, 1973).

## 1.6 FAILURE MECHANISMS

### 1.6.1 OXIDATION-BASED MODEL

High residual compressions (4~6 GPa) (Clarks, 1999) in the thermally grown oxide (TGO) at ambient and a pressure across interface (Nusier and Newaz, 1998) are induced due to the thermal expansion misfit and volume change. The TGO adhesion is compromised by S segregation, which happens at concentrations exceeding 0.3ppmw. Such segregation typically limits TBC spall life, especially in aero-components (Evans and Wang, 1998). Nusier et. al. (1998) observed the relationship between TGO thickness and damage accumulation during thermal cycling and proposed that the characteristic TGO which thickness led to TBC failure is 12  $\mu\text{m}$ .

A critical thickness related life model of TBCs at thermal cycling (thermal fatigue) is proposed by Meier et. al., (1991):

$$N = [(\Delta\epsilon_f / \Delta\epsilon)(1 - \delta / \delta_c)^c + (\delta / \delta_c)^c]^b \quad (1.12)$$

Where:  $\delta_c$  = critical TGO thickness which cause TBC spallation;  $b=7.64$ ;  $\Delta\epsilon_f$  = constant = 0.016 mm/mm;  $\Delta\epsilon$  = mechanical strain in TGO;  $c=1.0$ ;  $\delta$  = TGO thickness at a particular cyclic number.

### 1.6.2 DELAMINATION-BUCKLING MODEL

The delamination-buckling failure model (Figure 1.7) of TBCs has been extensively studied by researchers (Evans, 1998, Wang and Evans, 1998, He, et. al., 1998). Wright and Evans(1999) provide a comprehensive review. The following is a summary of this model:

#### 1. Separation nucleation in TBCs

An initial delamination is required for buckling and spallation for TBCs. It has been revealed that interface imperfection such as interface undulation or asperity plays a very important role on interface separation nucleation. Both mechanics (Hutchinson,1999; Evans, 1999; He, 1998) and numerical analyses (Nusier, 1997) indicated that imperfections result in redistribution of residual stresses and induce local tensile stresses normal to the interface, large enough and over sufficient spatial extent to cause the formation of separations. The interface imperfection could be result of oxidation (Wang,1998; Tolpygo and Clarke, 2000) or ridges of grain boundary of bond coat (Gell, 1999).

#### 2. Separation propagation

When the separation becomes large enough to satisfy buckling requirements, TBC will buckle. The buckle propagation inherently involves mode mixity effects and associated changes in the interface toughness. There is a critical stress,  $\sigma_p$  above which buckles always propagate.

### 3. Failure

Whether a buckle either continues to propagate or fractures the TBC, resulting in a spall, depends on the ration of the fracture toughness of the interface  $\Gamma_i$ , and the TBC,  $\Gamma_c$ , as well as the mixity angle. Spalling, rather than continued propagation along the interface, happens when the interface is relatively tough. This failure model proposed that TBC life is dominated by growth and coalescence of delaminations.

#### 1.6.3 THROUGH-THICKNESS SHEAR MODEL

Evans (1989) proposed that through-thickness shear cracks are developed in the TBC layer under compressive conditions in the TBC as shown in Figure 1.8.

#### 1.6.4 WRINKLE MODEL

Suo (1995) proposed this model, which was addressed earlier by a number of researchers as well (Siegler, 1993; Tolpygo and Grabke, 1994). According to this failure model, there is void formation under the TBC layer and folding effects may occur that lead to the cracking of the TBC layer at various locations. The mechanism is illustrated in Figure 1.9.

## 1.7 OBJECTIVES

The development of an initial separation constitutes an important prerequisite for the failure models; an understanding of its development needs further clarification. This dissertation further attempts

1. To evaluate progressive damage mechanisms and microstructural evolution for long-term durability of EB-PVD TBCs;
2. To identify key degradation mechanisms that control TBC life;
3. To assess the role of thermal wave imaging as a non-destructive evaluation technique which can determine the remaining life of TBCs.

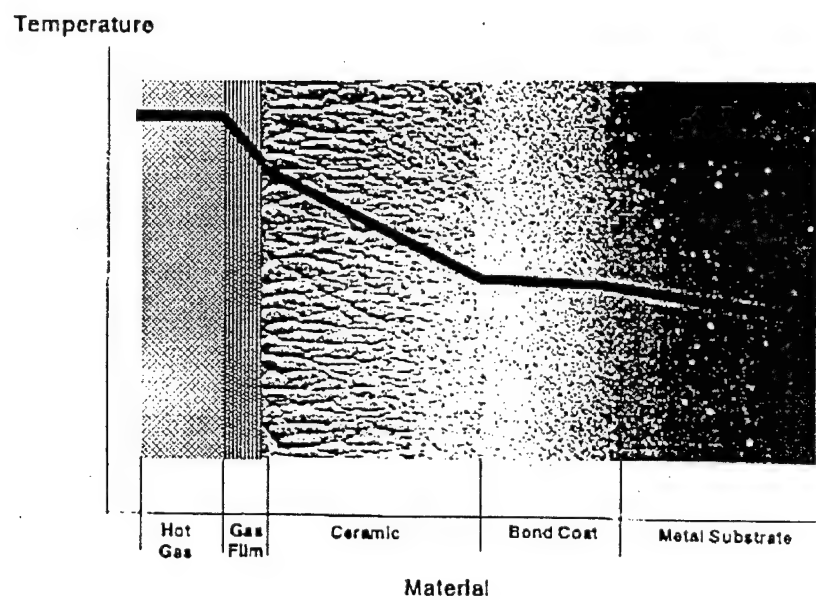
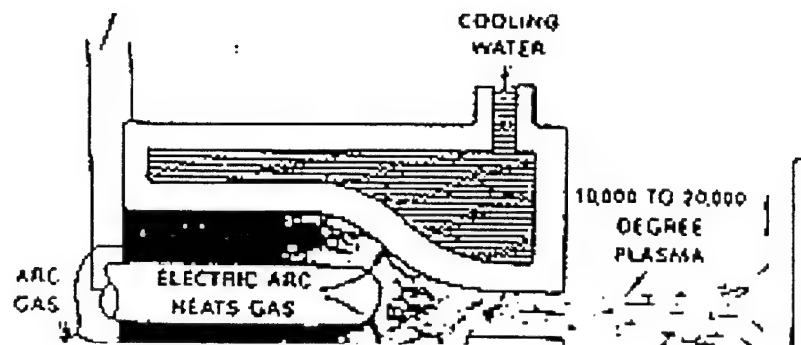


Figure 1.1 shows the temperature distribution across a TBCs. (Gupta, 1992)



**@PJL USTATUS JOB = ON**  
**@PJL USTATUS PAGE = OFF**  
**@PJL USTATUS DEVICE = ON**  
**@PJL USTATUS TIMED = 0**

Figure 1.2 shows a schematic diagram of plasma spray coating processing.

## 2.0 EXPERIMENTAL ASPECTS

### PREPARATION

The Pt-Al/EB-PVD TBC specimens in the form of round disks were supplied for this study by General Electric Aircraft Engines. The TBC system consisted of a Pt-Al bond coat deposited on a single crystal superalloy RENE N5 substrate by electro-plating with platinum followed by aluminization via chemical vapor deposition. Subsequent vacuum heat treating was performed to form a diffusion bond coat layer (Gell, et al., 1999). The 8 wt. % yttria-partially-stabilized zirconia (YSZ) layer was deposited by Electron Beam Physical Vapor Deposition (EB-PVD). The substrate was maintained at a constant temperature of  $\sim 1050^{\circ}\text{C}$  during the deposition. The diameter of the disk specimen was 24.5 mm, the thicknesses of TBC, bond coat and substrate were 0.127mm, 0.065 mm and 3.175 mm, respectively. The compositions of various layers are shown in table 2.1. A typical cross section of the Pt-Al/EB-PVD coating system is shown in Figure 2.1.

Two types of specimen were used in the study. Type 1 specimen is regular TBC specimen, which consisted of TBC topcoat, Pt-Al bond coat and substrate. The type 2 specimen is the same as Type 1 except that there is no TBC coat. Figure 2.2 schematically shows the geometry of the two types of specimen.

## 2.2 THERMAL TEST

Isothermal and thermal cycling tests of TBCs were performed in this study. Thermal test profiles are given in Figure 2.3. Rapid temperature furnaces CM 1610 BL (figure 2.4) and CARBOLITE RHF 1400 (Figure 2.5) were used for thermal cycling and isothermal tests, respectively. To insure the uniformity of the temperature during thermal cycle tests, four different thermocouples (Type K) were used, two of them located at the bottom of the furnace and they are very close to the samples. The other two thermocouples were located at the top of the furnace. Specimens were put on a movable stage. Specimens were moved up to heating chamber for high temperature exposure and moved down for rapid cooling by an air fan. A digital recorder (Honeywell) was used to record the temperature variation (Figure 2.4). A sample of this reordering is shown in Figure 2.6. A microstar controller was used to set the parameters used to define a thermal cycle, such as heat up time, hold time, cool down time, minimum temperature and maximum temperature, etc.

## 2.3 MATERIAL CHARACTERIZATION

Microstructure and damage process of the specimens were observed and monitored by on optical microscope, a scanning electron microscope (SEM) and a thermal wave image (TWI). Composition analysis was performed by Energy Dispersive Spectrum of X-ray (EDS). Phase identification was performed by x-ray diffraction. Specimens for metallograph observation were prepared by standard metallurgy methods.

Table 2.1 Composition of TBC system

Layer	material	composition (wt.%)
Substrate	RENE N5	7.5Co, 7.0Cr, 6.5Ta, 6.2Al, 5.0W, 3.0Re, 1.5Mo, 0.16Hf, 0.05C, 0.02Ti, bal Ni
Bond coat	Pt-Al	35Pt, 25Al, bal Ni
Ceramic TBC	YSZ	8Y <sub>2</sub> O <sub>3</sub> in ZrO <sub>2</sub>

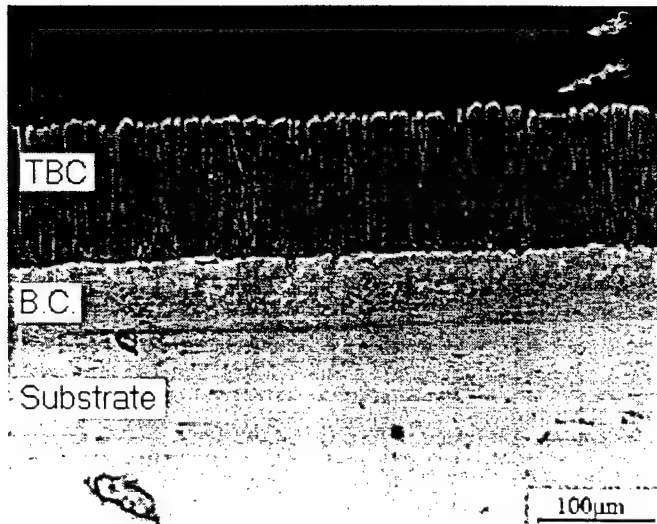
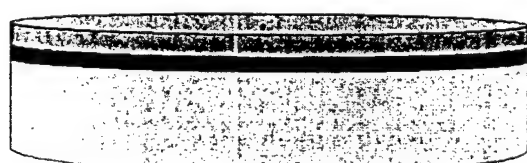


Figure 2.1 shows a typical cross section of a TBC specimen.

Type 1 (TBC/BC/Sub.)

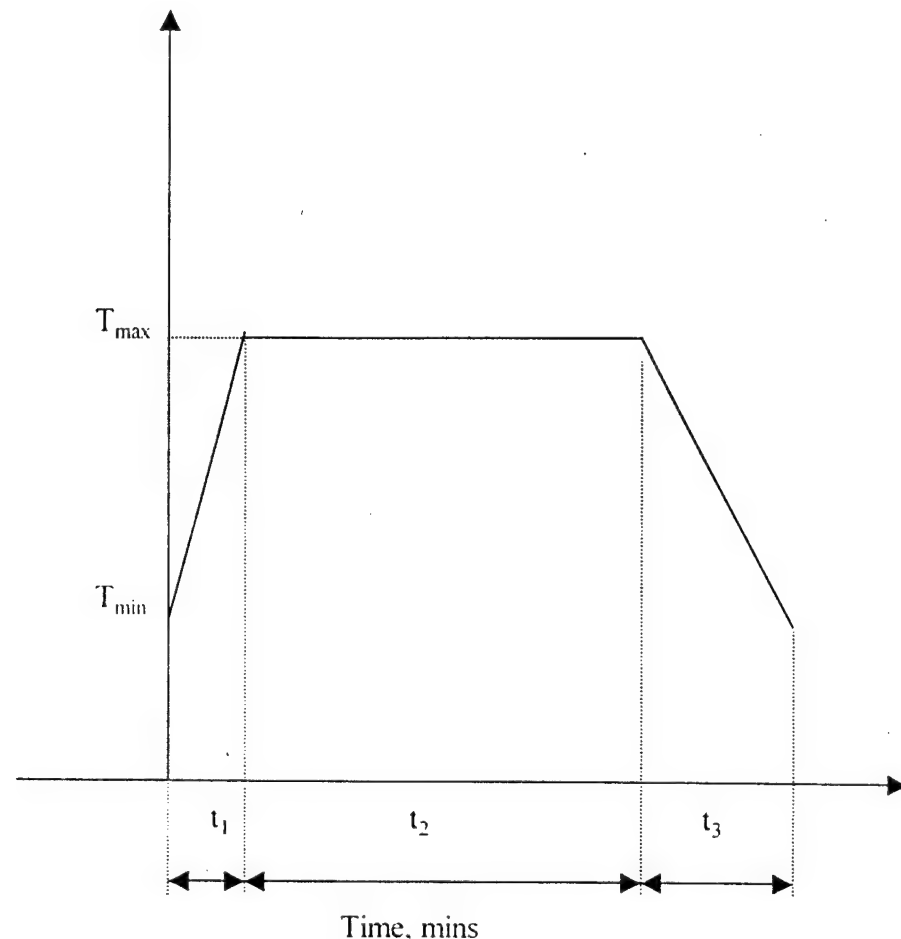


Type 2 (BC/Sub.)



Figure 2.2 shows the two types of specimen used in the study. Thickness: TBC/0.127mm; bond coat/0.65mm; substrate/3.175mm. Diameter:24.5 mm.

Temperature C



Thermal test	$T_{\min}$ (°C)	$T_{\max}$ (°C)	$t_1$ (min)	$t_2$ (min)	$t_3$ (min)
A	25	1177	9		Isothermal
B	200	1177	9	45	10
C	500	1177	5	10	2
D	200	1135	8	45	9

Figure 2.3. Thermal test profiles

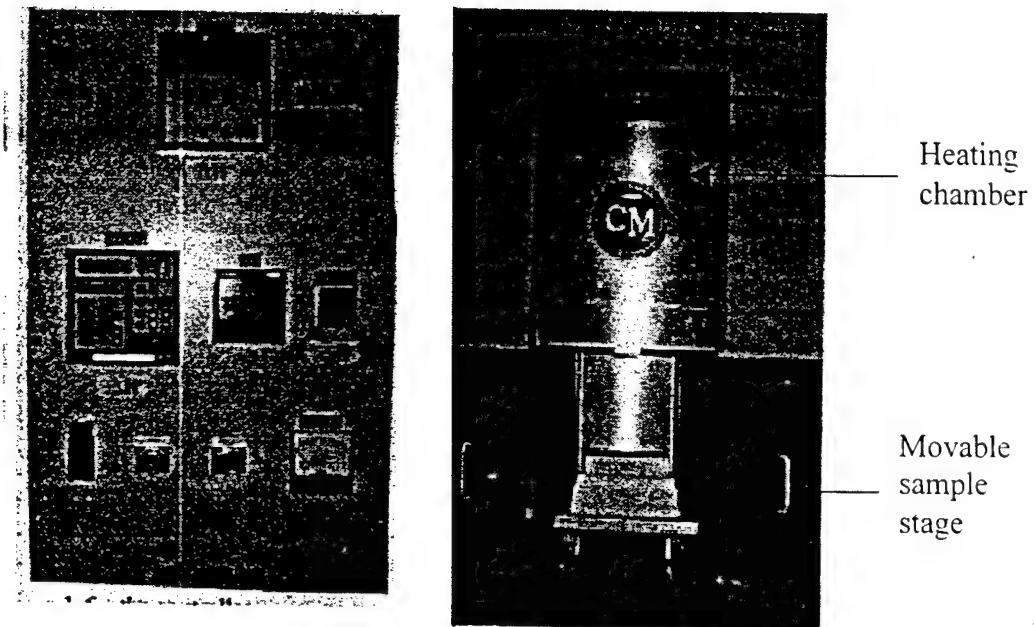


Figure 2.4 shows photograph of CM 1610 BL system for thermal cyclic test. (a) controller; (b) furnace.

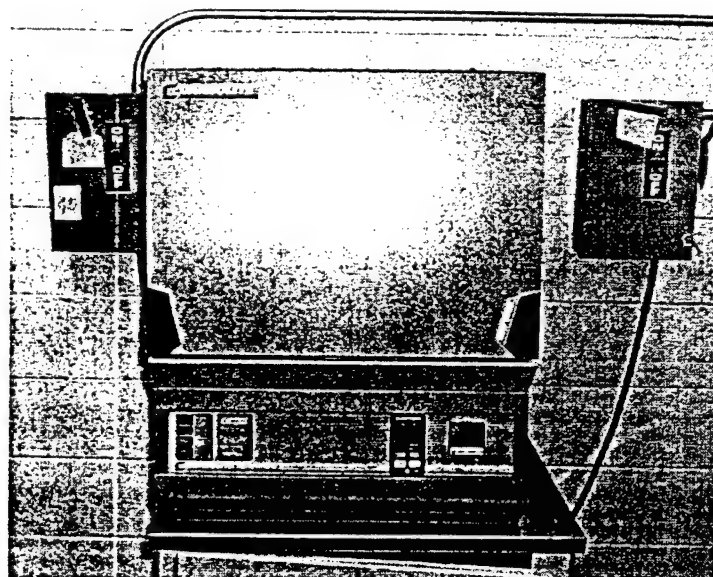


Figure 2.5 shows CARALITE RHF 1400 furnace for isothermal test.

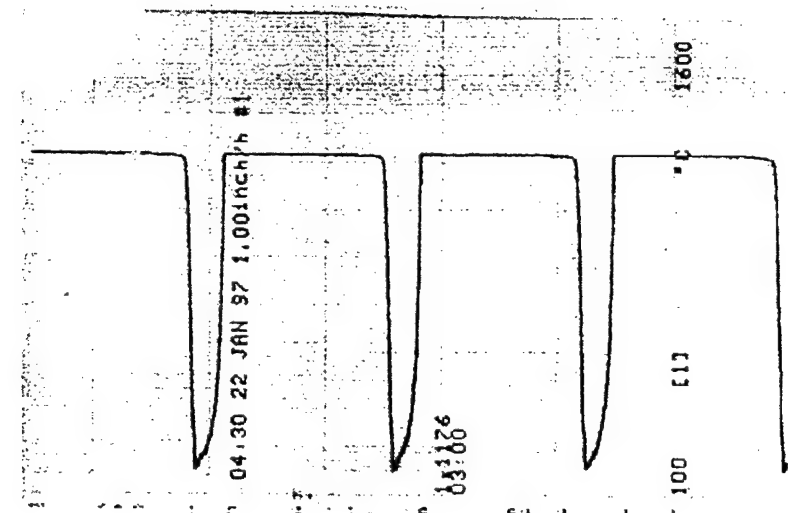


Figure 2.6 shows a sample of recorder print out for one of the thermal cycles.

### 3.0 RESIDUAL STRESS ANALYSIS IN THERAML BARRIER COATINGS

Residual stresses develop in TBCs during cool down from processing temperatures due to the thermal expansion mismatch between the different layers (substrate, bond coat, oxide and ceramic). These residual stresses could initiate damages at the TBC/TGO and /or TGO bond coat interfaces and finally leads spallation of TBC (Newaz, 1998, Nusier et al., 1998, 1999, 2000).

#### 3.1 RESIDUAL STRESS AND STRAIN ANALYTICAL BASED ON AN ELASTIC MODEL

When temperature is changed from  $T_0$  to  $T_1$ , the thermal strains  $\varepsilon_c^{th}$ ,  $\varepsilon_o^{th}$ ,  $\varepsilon_b^{th}$  and  $\varepsilon_s^{th}$  for ceramic coating, oxide(TGO layer), bond coat and substrate are given by

$$\varepsilon_c^{th} = \alpha_c (T_1 - T_0) \quad (3.1)$$

$$\varepsilon_o^{th} = \alpha_o (T_1 - T_0) \quad (3.2)$$

$$\varepsilon_b^{th} = \alpha_b (T_1 - T_0) \quad (3.3)$$

$$\varepsilon_s^{th} = \alpha_s (T_1 - T_0) \quad (3.4)$$

where  $\alpha_c$ ,  $\alpha_o$ ,  $\alpha_b$  and  $\alpha_s$  are the thermal expansion coefficients of ceramic, oxide, bond coat and substrate, respectively. Providing no bending is present in the

system, the elastic strain  $\varepsilon_c^e$ ,  $\varepsilon_o^e$ ,  $\varepsilon_b^e$  and  $\varepsilon_s^e$  in the constrained thermal barrier coating system can be expressed as

$$\varepsilon_c^e = \sigma_c \left[ \frac{1-\nu_c}{E_c} \right] \quad (3.5)$$

$$\varepsilon_o^e = \sigma_o \left[ \frac{1-\nu_o}{E_o} \right] \quad (3.6)$$

$$\varepsilon_b^e = \sigma_b \left[ \frac{1-\nu_b}{E_b} \right] \quad (3.7)$$

$$\varepsilon_s^e = \sigma_s \left[ \frac{1-\nu_s}{E_s} \right] \quad (3.8)$$

where  $\sigma_c$ ,  $\sigma_o$ ,  $\sigma_b$  and  $\sigma_s$  are stresses in the ceramic, oxide, bond coat and the substrate, respectively.: E and v with subscripts c, o, b and s are the Young's Moduli and the Poisson's ratios of the ceramic, oxide bond and substrate. Strain compatibility and force balance result in the following relations

$$\begin{aligned} \sigma_c \left[ \frac{1-\nu_c}{E_c} \right] + \alpha_c \Delta T &= \sigma_o \left[ \frac{1-\nu_o}{E_o} \right] + \alpha_o \Delta T = \sigma_b \left[ \frac{1-\nu_b}{E_b} \right] + \alpha_b \Delta T \\ &= \sigma_s \left[ \frac{1-\nu_s}{E_s} \right] + \alpha_s \Delta T \end{aligned} \quad (3.9)$$

$$\int_0^{t_c} \sigma_c \cdot dt + \int_0^{t_o} \sigma_o \cdot dt + \int_0^{t_b} \sigma_b \cdot dt + \int_0^{t_s} \sigma_s \cdot dt = 0 \quad (3.10)$$

where  $t_c$ ,  $t_o$ ,  $t_b$  and  $t_s$  are thickness of the ceramic coating, oxide layer, bond coat and substrate, respectively. For solving the problem, the summations are suggested. 1) the residual radial stress is constant in each layer; 2) the properties of the materials

are constant too. From equations 3.9 and 3.10, the elastic radial stress and elastic strain in each layer can be obtained

$$\sigma_c = \frac{\Delta TE_c E_b t_b (\alpha_b - \alpha_c)(1 - \nu_o)(1 - \nu_s) + \Delta TE_c E_o t_o (\alpha_o - \alpha_c)(1 - \nu_b)(1 - \nu_s) + \Delta TE_s E_s t_s (\alpha_s - \alpha_c)(1 - \nu_o)(1 - \nu_b)}{E_c t_c (1 - \nu_b)(1 - \nu_o)(1 - \nu_s) + E_o t_o (1 - \nu_b)(1 - \nu_c)(1 - \nu_s) + E_b t_b (1 - \nu_c)(1 - \nu_o)(1 - \nu_s) + E_s t_s (1 - \nu_b)(1 - \nu_o)(1 - \nu_c)} \quad (3.11)$$

$$\varepsilon_c^e = \frac{\{\Delta TE_b t_b (\alpha_b - \alpha_c)(1 - \nu_o)(1 - \nu_s) + \Delta TE_o t_o (\alpha_o - \alpha_c)(1 - \nu_b)(1 - \nu_s) + \Delta TE_s t_s (\alpha_s - \alpha_c)(1 - \nu_o)(1 - \nu_b)\}(1 - \nu_c)}{E_c t_c (1 - \nu_b)(1 - \nu_o)(1 - \nu_s) + E_o t_o (1 - \nu_b)(1 - \nu_c)(1 - \nu_s) + E_b t_b (1 - \nu_c)(1 - \nu_o)(1 - \nu_s) + E_s t_s (1 - \nu_b)(1 - \nu_o)(1 - \nu_c)} \quad (3.12)$$

The total strain of TBC is

$$\varepsilon = \varepsilon_c^e + \alpha_c \Delta T \quad (3.13)$$

The properties of materials used for the calculation of stresses and strains of TBCs were summarized in (Table 3.1).

### 3.2 DIGITAL SPECKLE CORRELATION

Speckle technical, which is non-contact strain measurement method, was used to measure the strain of the TBC surface and verify the result of FEA modelling. This technique is based on a high-speed image processor. The experimental set up is shown in figure 3.3. TBC specimens that were cycled in the furnace were taken out about 560 °C and cooling down to room temperature. Strain measurements were taken from 450 °C to 50 °C. A digital pyrometer was used on the TBC specimen to monitor temperature.

### 3.3 FINITE ELEMENT STRESS ANALYSIS

The finite element analysis was implemented in the ABAQUS (1998) general-purpose program. A half two-dimensional model was used since the specimen is axsymmetric. The boundary condition was that the nodes along the axsymmetric axis were allowed to move in the axial direction only and the left bottom corner was fixed to prevent rigid body motion. Continuum axisymmetric element was used to generate two-dimensional FEA meshes. Elastic and elastic-plastic analyses were executed. Temperature-dependent material properties used in the analysis were given in Table 3.1 and Table 3.2.

The geometry of the specimen has been shown in chapter 2. The specimen was cooled down from a processing temperature of 1025 °C to room temperature 25 °C and then elevated to a temperature of 1177 °C at which the oxide layer was generated by oxidation. Residual stresses built between processing temperature and oxidation temperature would release and was ignored since creeping at higher temperature (Ali, 1999). Therefore, the stress free temperature was assumed to be 1177 °C. The stresses in each layer of TBCs were obtained during cooling from 1177 °C to 500 °C, 200°C and 25 °C.

### 3.4 RESULTS

Figure 3.2 shows the compares of result of total strain (thermal expansion strain plus mechanical strain) of TBC surface of the specimen computed by

analytical, FEA and measured by Digital Speckle Correlation method, respectively. Strain free temperature was assumed at 450 °C. In generally speaking, the results have shown a very good agreement among FEA, theoretical and speckle technical method. The result measured by Digital Speckle Correlation method shows a slightly lower value compared with two results. The assumption of perfect interface bond of TBCs in FEA and theoretical analytical may result in the difference of results. The results indicate that FEA modeling is acceptable.

The radial stresses in each layer of TBCs computed by finite element analysis of elastic model are shown in Figure 3.3 after cooling down to 500 °C, 2000 °C and 25 °C. The very high compressive residual stress (-6.05 GPa) in TGO was predicted when cooled down to room temperature. It compared with value (4-6 GPa) measured by photostimulated luminescence spectroscopy (Tolpygo and Clarke, 2000). The stress distributions near the edge of the specimen are shown in Figure 3.4-3.6 after cooling down to room temperature. The in-plane radial stress at edge area is very low (figure 3.4), while axial normal tensile stress and shear stress appear high at top coat/TGO interface and TGO/bond coat interface (Figure 3.5 and 3.6).

The bond coat layer also was predicted to subject to a relatively high residual in-plane stress (~350MPa) during cooling. Such high stress could lead bond coat to plastically deform at specific temperature according to temperature dependent material property of bond coat Figure 3.1. An elastic-plastic model was used to predict the stress distribution during thermal cycling. The result (figure 3.7) shows that an in-plane tensile stress is predicted in bond coat and at TGO/bond coat interface when temperature back to the peak temperature (1177 °C) during the

a 500-1177 °C thermal cycle (figure 3.4). The results reveal that bond coat and bond coat were predicted to be under tension-loaded during thermal cycling at thermal test C.

### 3.5 SUMMARY

The following summary can be made:

1. The very high residual radial stress was built in the TGO and the bond coat layers during cooling from high temperature. Those high residual stresses will result in damage in TBC system.
2. The bond coat and the TGO/bond coat interface was subjected to a radial tension stress at peak temperature during thermal test C.

**TABLE 3.1**  
**Material properties at 22, 566, and 1149 °C**

Material	Young's Modulus (Gpa)	Poisson's ration	Coefficient of Thermal expansion ( $\times 10^{-6} \cdot ^\circ\text{C}^{-1}$ )
Substrate	175.8	0.25	13.91
	150.4	0.2566	15.36
	94.1	0.3244	19.52
Bond coat	133.9	0.27	15.16
	121.4	0.27	15.37
	93.8	0.27	13.48
TBC	23.6	0.25	10.01
	6.9	0.25	11.01
	1.84	0.25	13.41
Oxide	386	0.257	6.00
	349	0.257	8.00
	311	0.257	8.90

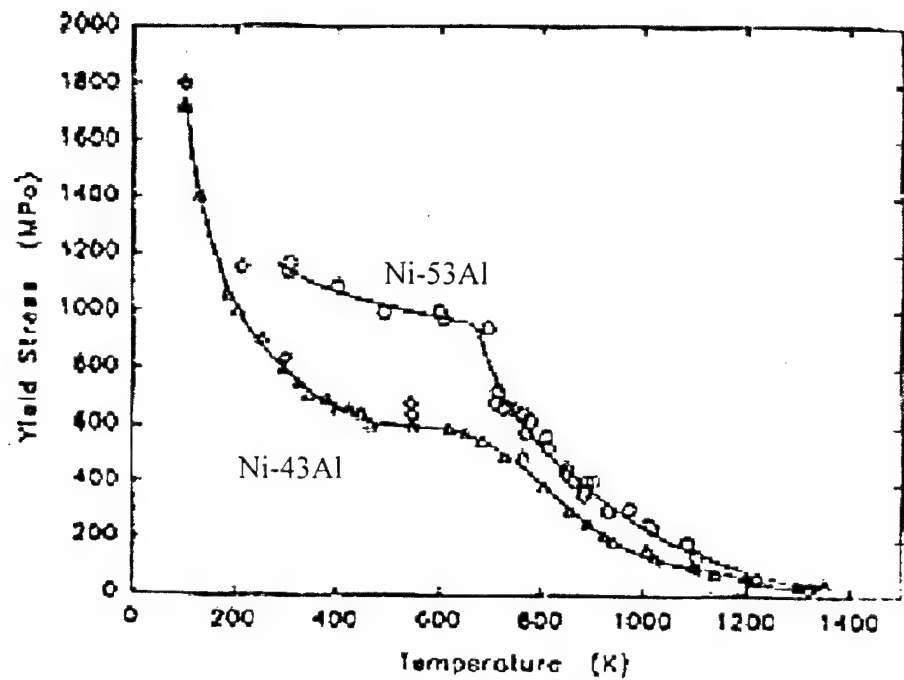


Figure 3.1 Temperature dependence of compressive yield strength of polycrystalline NiAl. (from Pascoe and Newey, 1968)

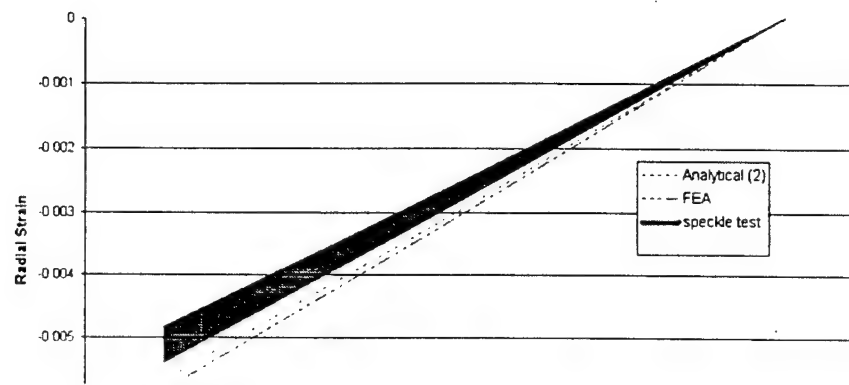


Figure 3.20 radial strains of TBC obtained by Digital Speckle Correlation, FEA and analytical methods, respectively.

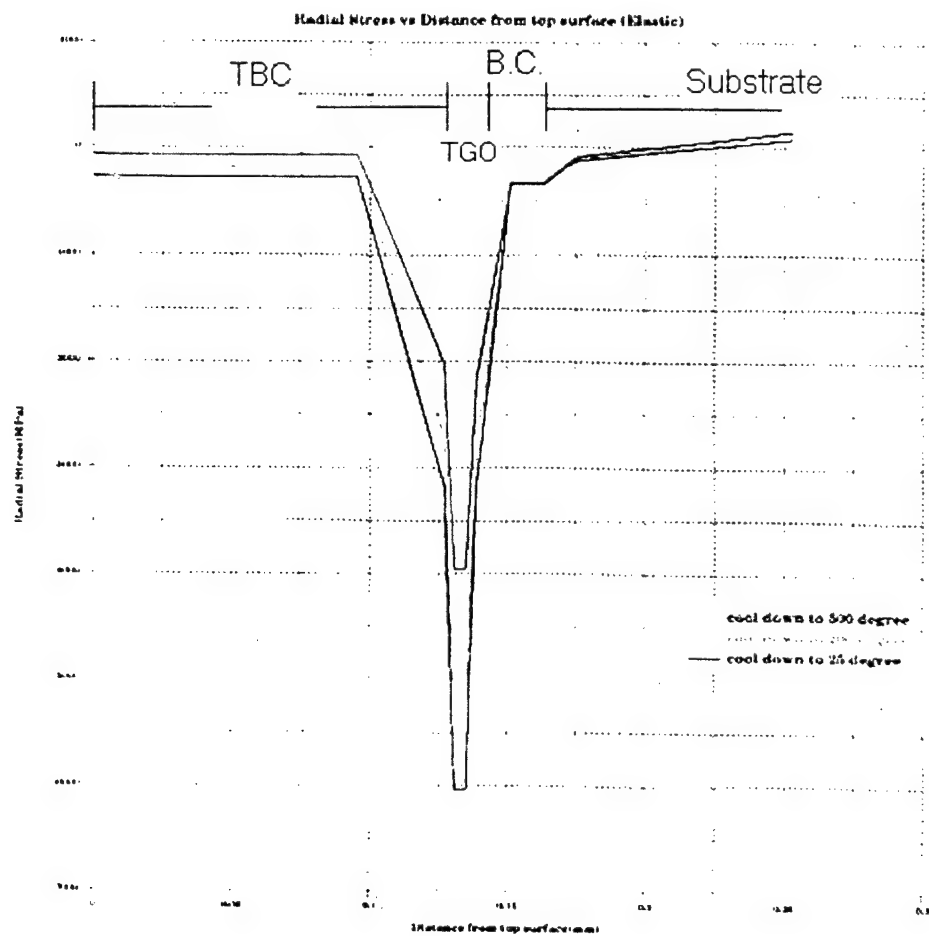


Figure 3.3 shows residual radial stresses at all layers in TBC system at temperature dropping from 1177 °C to 500 °C, 200 °C and 25 °C, Using elastic FEA modeling.

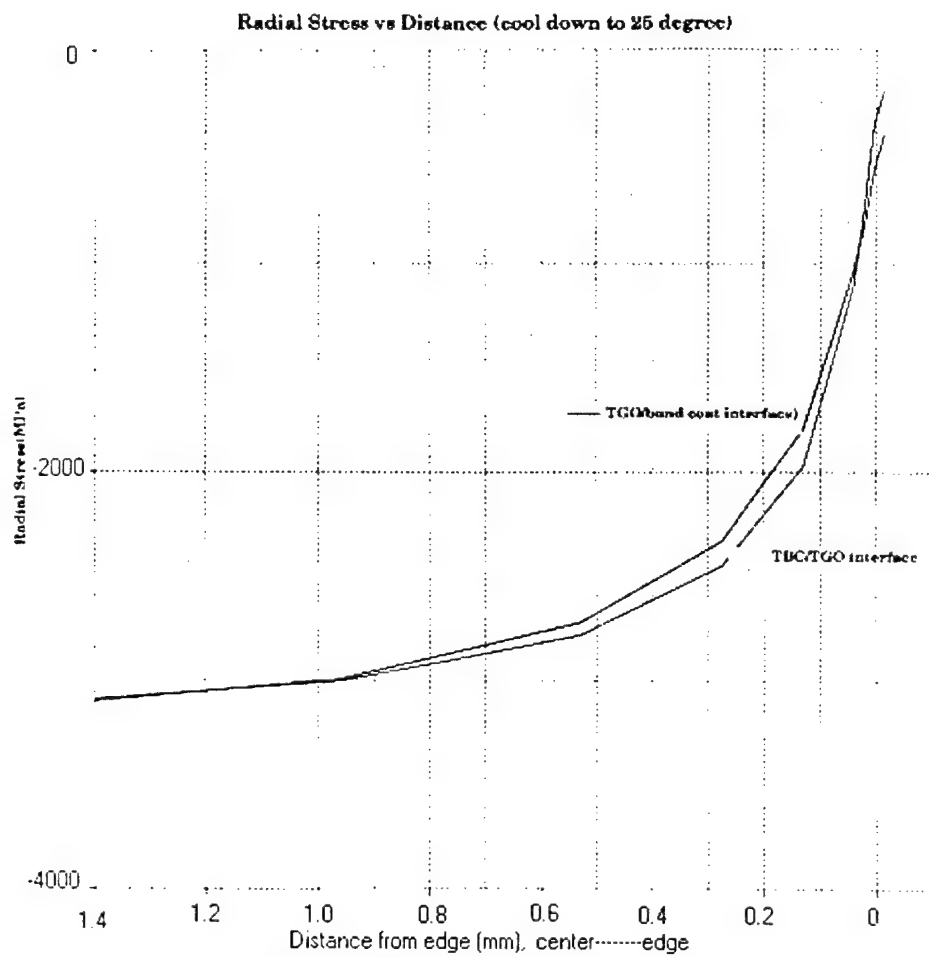


Figure 3.4 shows radial stress distribution along TBC/TGO and TGO/bond coat interfaces at edge area of a specimen cooling from 1177 °C to 25 °C.

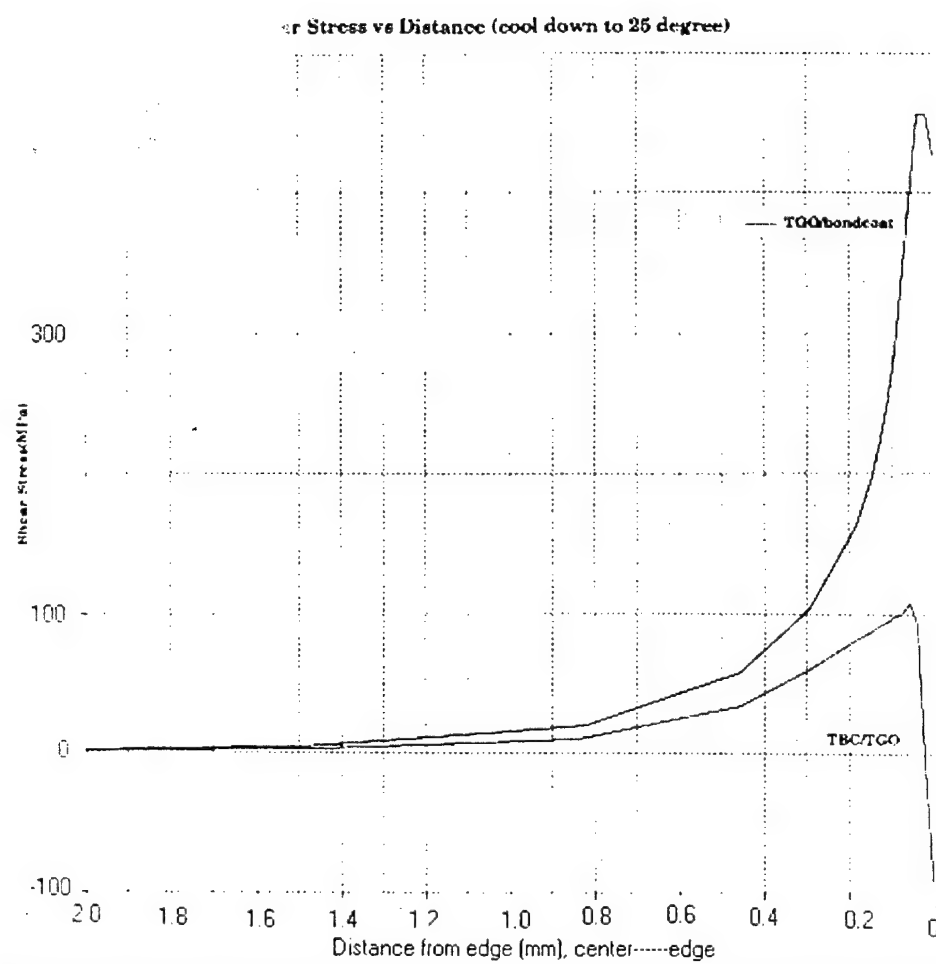


Figure 3.5 shows shear stress distribution along TBC/TGO and TGO/bond coat interfaces at edge area of a specimen cooling from 1177 °C to 25 °C.

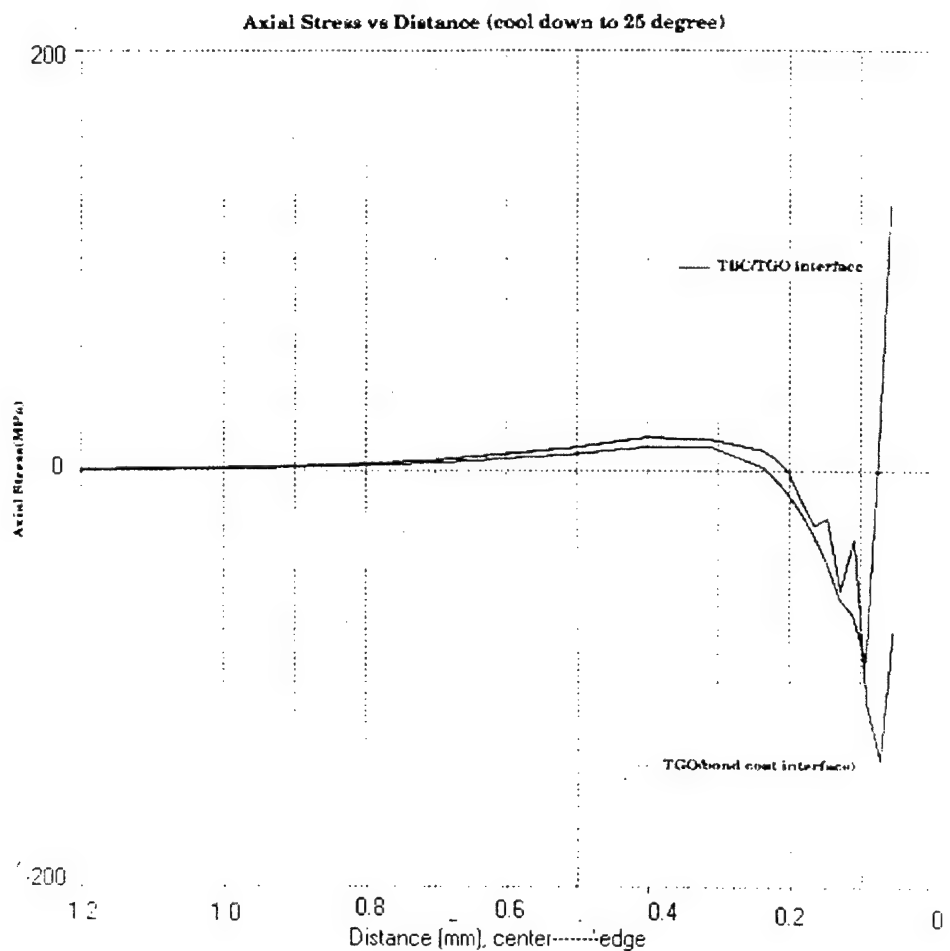


Figure 3.6 shows nominal out-of-plane stress distribution along TBC/TGO and TGO/bond coat interfaces at edge area of a specimen cooling from 1177 °C to 25 °C.

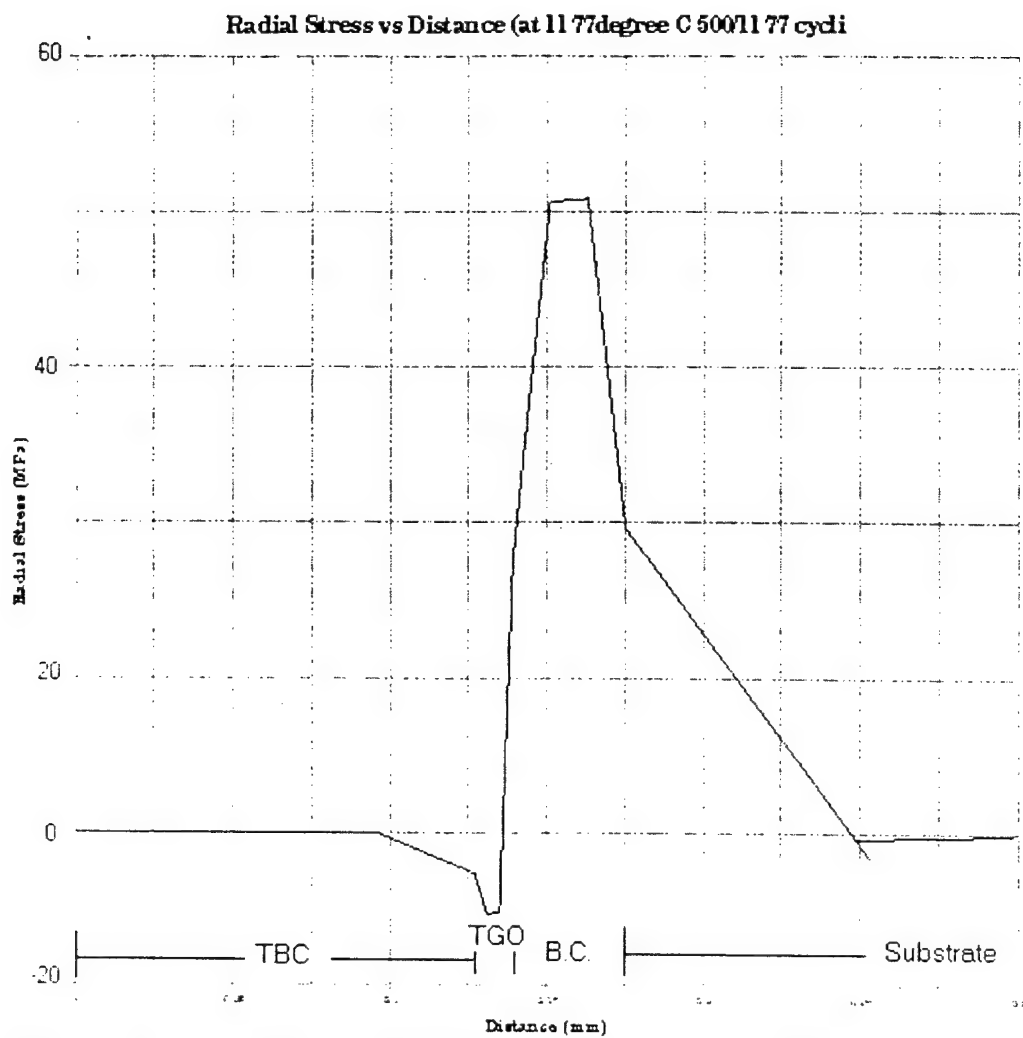


Figure 3.7 shows prediction of radial stress at all layers at 1177 °C during thermal cycling between 1177 °C and 500 °C, using elastic-plastic FEA modeling.

## 4.0 MICROSTRUCTURE CHANGE OF BOND COAT LAYER AND ITS EFFECTS ON OXIDE SCALE

The bond coat helps to provide higher oxidation/corrosion resistance of the superalloy substrate and also provides accommodation of thermal expansion mismatch effect between the ceramic TBC and the superalloy. Previous work has shown that the TBC lifetime is limited by the oxidation kinetics of the bond coat, and that the spallation of TBC occurs via cracking at the thermally grown oxide (TGO) layer (Newaz et al., 1998, Nusier et al., 1997). The TGO layer is essentially alumina oxide ( $Al_2O_3$ ). It is the objective of this chapter to determine the microstructural changes due to diffusion and oxidation of the bond coat, and their influence on oxidation behaviors during thermal cycling.

### 4.1 EXPERIMENTAL ASPECTS

TBC (type 1) specimens were used in this chapter. The specimens were thermally tested at thermal test A, B, C and D, respectively. The thermal cycled samples were cold mounted by using epoxy resin and cut. Standard metallurgical procedures were used to prepare the samples. Some of the specimens were etched in a solution consisting of 2% hydrofluoric acid, 8% nitric acid and 90%  $H_2O$  by volume. All specimens were investigated by optical and electron microscope combined with energy dispersive X-ray spectroscope (EDS). The average chemical composition analysis by using SEM/EDS was

performed with an area of  $20 \times 10\mu\text{m}^2$ . Phase identification was performed by X-ray diffraction.

## 4.2 RESULTS AND DISCUSSION

### 4.2.1 MICROSTRUCTURE OF BOND COAT IN THE AS-RECEIVE

Characteristic microstructure features of the coating system of a TBC sample in the as-received condition (without any thermal cycling) are shown in Figure 4.1(a). No oxidation product was observed at the bond coat/topcoat interface, and there was no cracking at the interface. The bond coat consisted of two distinct zones. The outer one is a single phase zone (zone 1) about 0.032 mm in thickness. X-ray diffraction analysis (Figure 4.2) of bond coat surface shows the phase structure is the same as  $\beta$ -NiAl (B2 ordered body centered cubic structure, CsCl type). The composition determined by EDAX (Figure 4.1 (b)) indicated that Pt atoms partially replaced the Ni atoms in this phase structure. The phase was named as  $\beta$ -(Ni, Pt)Al in this dissertation. The other zone (named as zone 2) is a two-phase zone about 0.028 mm in thickness where fine W and Ta-rich phases dispersed in a matrix  $\beta$  phase (Figure 4.1(c)). The average chemical compositions of the two zones are given in Table 1.

#### 4.2.2 MICROSTRUCTURES OF BOND COAT AT THERMAL CYCLING

The variations of the average concentration of Ni, Al and Pt in the bond coat layer as a function of thermal cycles are summarized in Figure 4.4. At first stage (before 25 cycles), the concentration of Al and Pt decrease rapidly while the Ni concentration increases quickly. After that, the rate of decrease of the Al and Pt concentration and the rate of increase of the Ni concentration tend to slow down. Change of Cr, Co, W, and Ta concentrations are similar to that of Ni.

The microstructural characteristics of the bond coat also change during thermal cycling. With increasing thermal cycles, new precipitates form on the grain boundaries [Figure 4.4 (a)-(d)]. The precipitates continuously grow. The volume percentage of the precipitates is about 40% of the bond coat after 175 cycles. The chemical composition of the precipitates is (in mass%) 65.51Ni, 7.60 Al, 5.33 Pt, 5.70 Cr, 8.59 Co, 5.26 Ta and 2.83 W. EDAX spectrums of the two phases in the bond coat are shown in Figure 3-4(e) and (f), respectively. The X-ray diffraction pattern of the bond coat after 175 cycles at thermal test B and standard pattern of  $\gamma'$ -Ni<sub>3</sub>Al are shown in Figure 3-5. Overall, the new precipitates are identified as  $\gamma'$ -(Ni, Pt)<sub>3</sub>Al phase (Li<sub>2</sub> ordered face centered cubic structure, AuCu<sub>3</sub> type). The selective oxidation of aluminum of the bond coat at high temperature resulted in aluminum depletion and nickel rich (Meier and Pettit, 1992). At same time, Ni, Cr, Co...diffused along grain boundaries into the bond coat. When the composition at the grain boundary in the bond coat reached the composition of  $\beta/\gamma'$  phase boundary (see Ni-Al phase diagram, Figure 3-6),  $\gamma'$  precipitated at the grain boundaries

The recrystallization of W and Ta-rich phase in zone 2 of the bond coat identified, and its percentage of volume gradually decreases.

Thickness of the bond coat (i.e.  $\beta$  phase layer) against the number of cycles at thermal test B is shown in Figure 3-7. The enlargement of  $\beta$ -(Ni, Pt)Al layer occurred rapidly at the first 25 cycles then subsequently receded. The layer did not change apparently after 50 cycles.

The thickness change of the bond coat layer was contributed to interdiffusion of bond coat/substrate and oxidation of bond coat. The driving force for bond coat/substrate interdiffusion is the differences in thermodynamic activities of the elements in the bond coat and substrate. Unfortunately, activity data are not available for this system. It is assumed that concentration differences are approximately proportional to the activity differences, and the diffusion of a given element occurs down its concentration gradient (Basuki et al., 1997). The diffusion follows Fick's first law:

$$J_i = D_i \left( \frac{dC_i}{dx} \right) \quad (4.1)$$

Where  $J_i$  is the flux of component i;  $C_i$  is concentration of I; and x is distance.

The Al and Pt diffused inwards while Ni, Cr, Co, W and Ta diffused outwards during thermal cycling. Two types of phase transformation occurred in bond coat because of the interdiffusion and oxidation. (1)  $\gamma + \gamma' \rightarrow \beta$  transformation at interface of bond coat/substrate due to the Kirkendall effect (see chapter 1). In other words, the rate of Ni diffusion from substrate to the bond coat was greater than the rate of Al diffusion from the bond coat to the substrate ( $D_{Ni}/D_{Al} > 1$ ). The Kirkendall effect led Ni depletion in the substrate near the interface of bond coat/substrate and led phase transformation (1) to

occur. After the  $\beta$  layer in the bond coat had enlarged to a maximum level of nickel enrichment, the  $\beta$  layer began to recede by the transformation (2)  $\beta \rightarrow \gamma$ . Since selective oxidation of aluminum of the bond coat at the high temperature resulted in aluminum depletion and nickel rich, the nickel concentration gradient between bond coat and substrate decreased. It led to greatly decease  $D_{Ni}$  (diffusivity of nickel) and  $D_{Ni}/D_{Al} < 1$ . The phase transformation (2) took place (Basuki et al, 1997). After 50 cycles, the interdiffusion of nickel and aluminum tended to balance, and  $D_{Ni}/D_{Al} \sim 1$ . The thickness of the  $\beta$ -(Ni, Pt)Al layer (bond coat) did not change apparently.

#### 4.2.3 EFFECT OF THERMAL TEST CONDITIONS ON MICRSTRUCTURES OF BOND COAT

**Effect of maximum temperature:** Figure 4.8 shows the microstructure of cross sections of specimens after 25 and 100 thermal cycles at thermal test D, at which the maximum temperature was 1135 °C. The  $\gamma$  precipitates could not be observed obviously at lower magnification, and they appeared after 100 cycles. The result indicated that the dynamics of phase transformation at 1135 °C were much lower than these at 1177 °C due to lower diffusivity at lower temperature. According to diffusion theory, the diffusivities, which govern diffusion and oxidation processes generally, increase exponentially with increasing maximum temperature (Nesbitt, 1984). However, the thickness of the bond coat at thermal test D was greater than that at thermal test B after the same number of thermal cycles (figure 4.7). The bond coat enlargement was related to the ratio of intrinsic

diffusivity  $D_{Ni}/D_{Al}$  (Janssen, 1972). It reveals that the ratio of intrinsic diffusivity  $D_{Ni}/D_{Al}$  was greater at temperature 1135 °C than the ratio at temperature 1177 °C.

**Effect of holding time:** The microstructure of bond coat experimented at isothermal test (thermal test A) for 50 hours is shown in figure 3-9. The feature of microstructures in the bond coat at isothermal test (thermal test A) was different from the feature of microstructures at thermal cycling test (figure 4.4). The  $\gamma'$  phase dispersed in the bond coat at the isothermal test, while the  $\gamma'$  phase formed preferentially at grain boundaries of the bond coat at thermal cycling. Janssen (1967, 1972) systematically investigated the interdiffusion and  $Ni_3Al$  growth mechanisms in the nickel-rich part of the Ni-Al system at 400 °C to 1300 °C isothermal diffusion in a vacuum. According to his results, it was concluded that at temperatures of 1100 to 1300 °C bulk diffusion is the main process determining the growth of the  $\gamma'$ - $Ni_3Al$  layer in NiAl-Ni diffusion couples.  $\gamma'$ - $Ni_3Al$  does form at the grain boundaries preferentially. Similar results were shown by Basuki et al. (1996). Ni concentration enriched continuously and distributed uniformly in the bond coat due to aluminum selective oxidation and interdiffusion at isothermal oxidation at 1177 °C. When the composition of the bond coat reached the composition of  $\beta/\gamma'$  phase boundary (figure 4.6),  $\gamma'$  precipitated and dispersed in the bond coat.

In the thermal cycling test, the Ni atoms segregated to grain boundary due to vacancy-solute atom pair diffusion to the grain boundary during cooling (Doig, 1987, Xu, 2000). The diffusion rate of the grain boundary increased since the defects at the grain boundary increased due to grain boundary sliding at high residual stress during cooling (see chapter 4). Therefore, Ni atoms segregated at grain boundaries of the bond coat and resulted in  $\gamma'$  precipitated at the grain boundaries preferentially.

Figure 4.10 shows the highest volume fraction of the  $\gamma'$  phase in the bond coat layer after 550 cycles at thermal test C (the shortest holding time at peak temperature 1177 °C). It reveals that the higher frequency of thermal cycling led to move rapid Ni enrichment and Al depletion due to the acceleration of oxidation and grain boundary diffusion.

#### 4.2.4 THE EFFECT OF MICROSTRUCTURES ON OXIDE SCALE

The PtAl as a desirable bond coat layer has a very good oxidation resistance (Pettit, 1988). However, the composition and microstructure of the bond coat will change due to oxidation and interdiffusion between the bond coat and the substrate during service at high temperature. As demonstrated above, the microstructures of the bond coat layer changed from single  $\beta$ -(Ni,Pt)Al phase to  $\beta$ -(Ni,Pt)Al plus  $\gamma'$ -(Ni,Pt)<sub>3</sub>Al at the thermal test at high temperature. EDS analysis indicated that Ni rich oxide existed in the TGO layer in the failed specimen (Figure 4.11). In order to investigate the effects of the microstructure of the bond coat on the oxide scale, a failed TBC specimen after 175 cycles at thermal test B was used. TBC coat and the TGO layer were carefully removed by polishing. Figure 4.12(a) shows the surface microstructure of the bond coat. The bond coat consisted of two phases,  $\beta$ -(Ni,Pt)Al (dark area in the picture) and  $\gamma'$ -(Ni,Pt)<sub>3</sub>Al (white area in the picture). The sample was oxidized at 1177 °C in air. The microstructure of oxide on the two phases was different after two hours of oxidation (Figure 4.12(b)). Oxide on  $\beta$ -(Ni,Pt)Al had the ridged morphology, while oxide on  $\gamma'$ -(Ni,Pt)<sub>3</sub>Al had equiaxed grains which contained Ni rich oxide (Figure 4.12 (c)). After 48 hours oxidation, the oxide on  $\gamma'$ -(Ni,Pt)<sub>3</sub>Al spalled during cooling from 1177 °C to room

temperature and cavities existed at the oxide/bond coat interface (Figure 4.12 (d)), while oxide layer on  $\beta$ -(Ni, Pt)Al still adhered to the bond coat well. The results indicated that the oxide scales formed on  $\gamma'$ -(Ni, Pt)<sub>3</sub>Al are not adherent. Previous research in oxidation of the Ni-Al system (Pettit, 1967, Pettit et al. 1994, Nesbitt and Barrett, 1993, Doychak, 1994) indicated that  $\beta$ -NiAl has a very good oxidation resistant, and a continuous  $\alpha$ -Al<sub>2</sub>O<sub>3</sub> scale can form on  $\beta$ -NiAl at temperature above 900 °C. The less protective oxides NiO/NiAl<sub>2</sub>O<sub>4</sub> will form on the  $\gamma'$ -Ni<sub>3</sub>Al at temperature above 1000 °C in air as a result of the lack of sufficient Al flux to the oxide/bond coat interface. The formation of the less protective oxides is commonly referred to as breakaway oxidation (Tawancy, 1998, Nesbitt, 1993, Nesbitt, 1984). The latest investigation (Schilbe, 2000) has shown that Ni and Cr oxide could formed not only at TGO/bond coat interface and also at TBC/TGO interface. The adhesion of TBC to bond coat gradually lost with thermal cycling (Gell et al., 1999).

### 4.3 SUMMARY

The following summary can be made based on current investigations:

1. Microstructures and the thickness of the bond coat changed due to oxidation and interdiffusion during thermal testing.
2. Thermal test conditions influenced the changes of both microstructure and thickness in the bond coat.

3. Oxidation behaviors of the bond coat were influenced due to microstructure change of the bond coat. Less protective oxide Ni oxide formed in TGO layer and affected the adhesion of TBC to the bond coat.

**Elemental composition of bond coat of untested sample. (wt%)**

	Ni	Al	Pt	Cr	Co	Ta	W	Mo
Zone 1	34.23	25.09	35.69	0.72	4.53	<0.1	0.5	<0.1
Zone 2	40.00	14.94	4.97	9.14	9.21	12.04	10.72	1.02

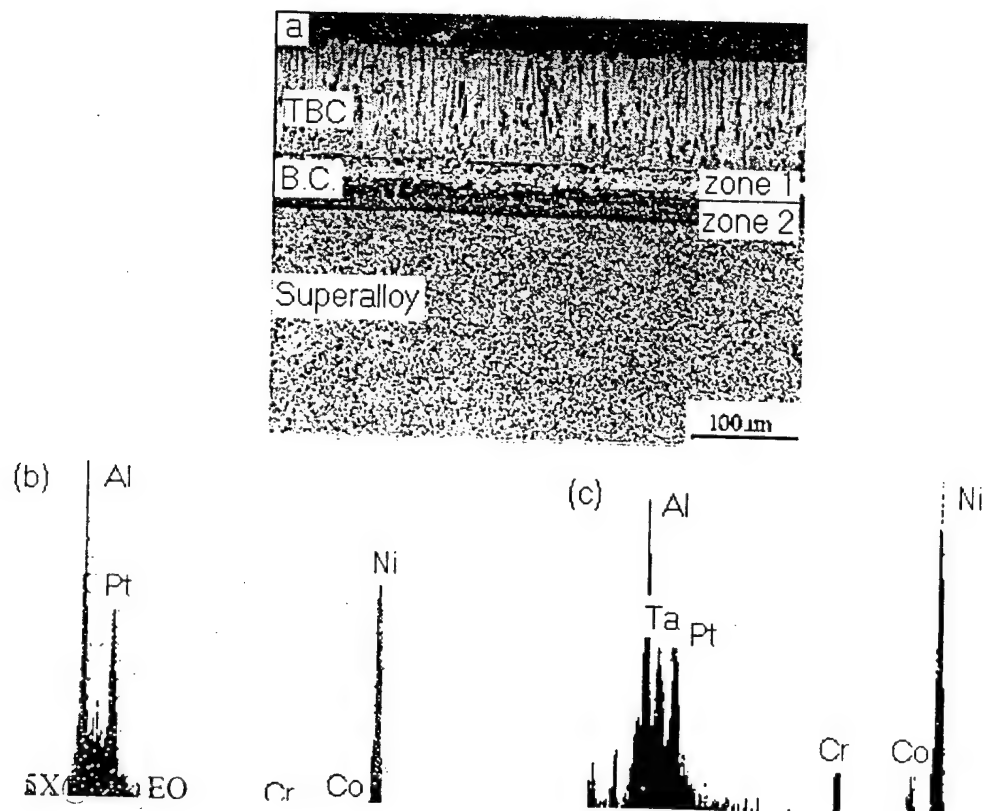


Figure 4.1 shows a typical TBCs microstructure at as-received condition (a). TBC coat has a columnar structure. Bond coat layer consists of two distingsh zones. (b) and (c) are composition of zone 1 and zone 2, respectively.

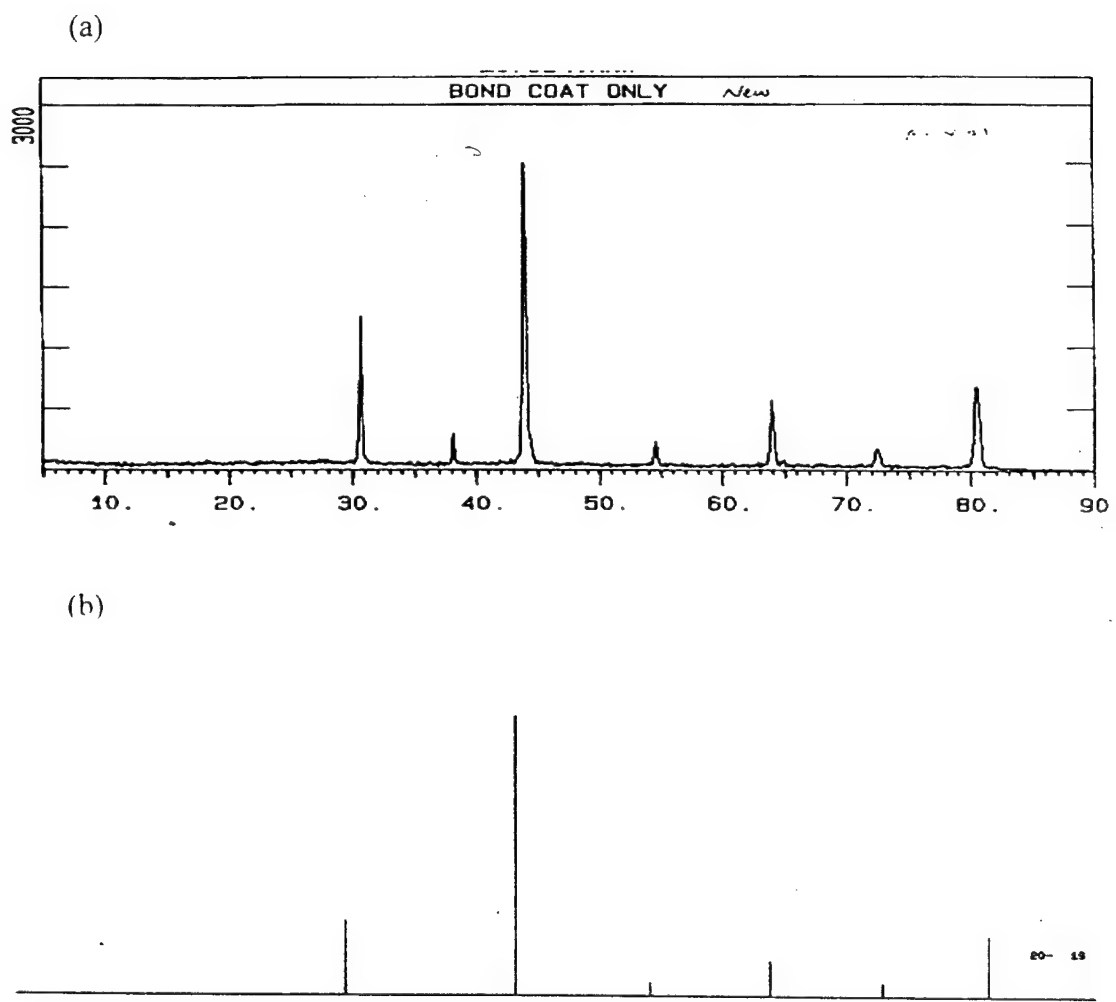


Figure 4.2 is x-ray diffraction pattern derived from the bond coat surface as-received condition (a). (b) is a standard pattern of  $\beta$ -NiAl phase (reference card number is 20-19).

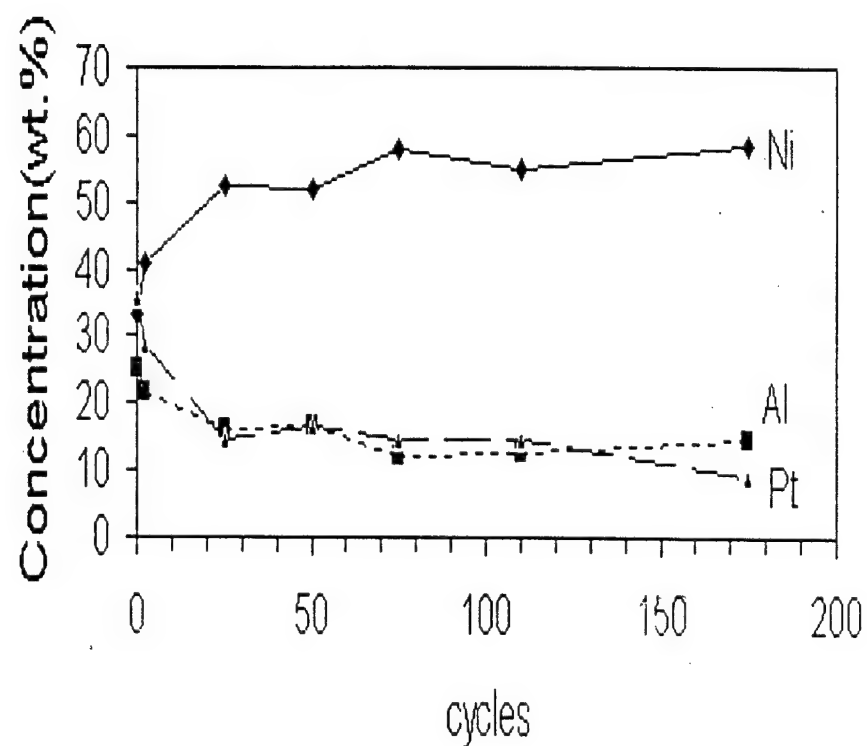


Figure 4.3 shows concentrations of AL, Ni and Pt in the bond coat change with number of cycles at thermal test B.

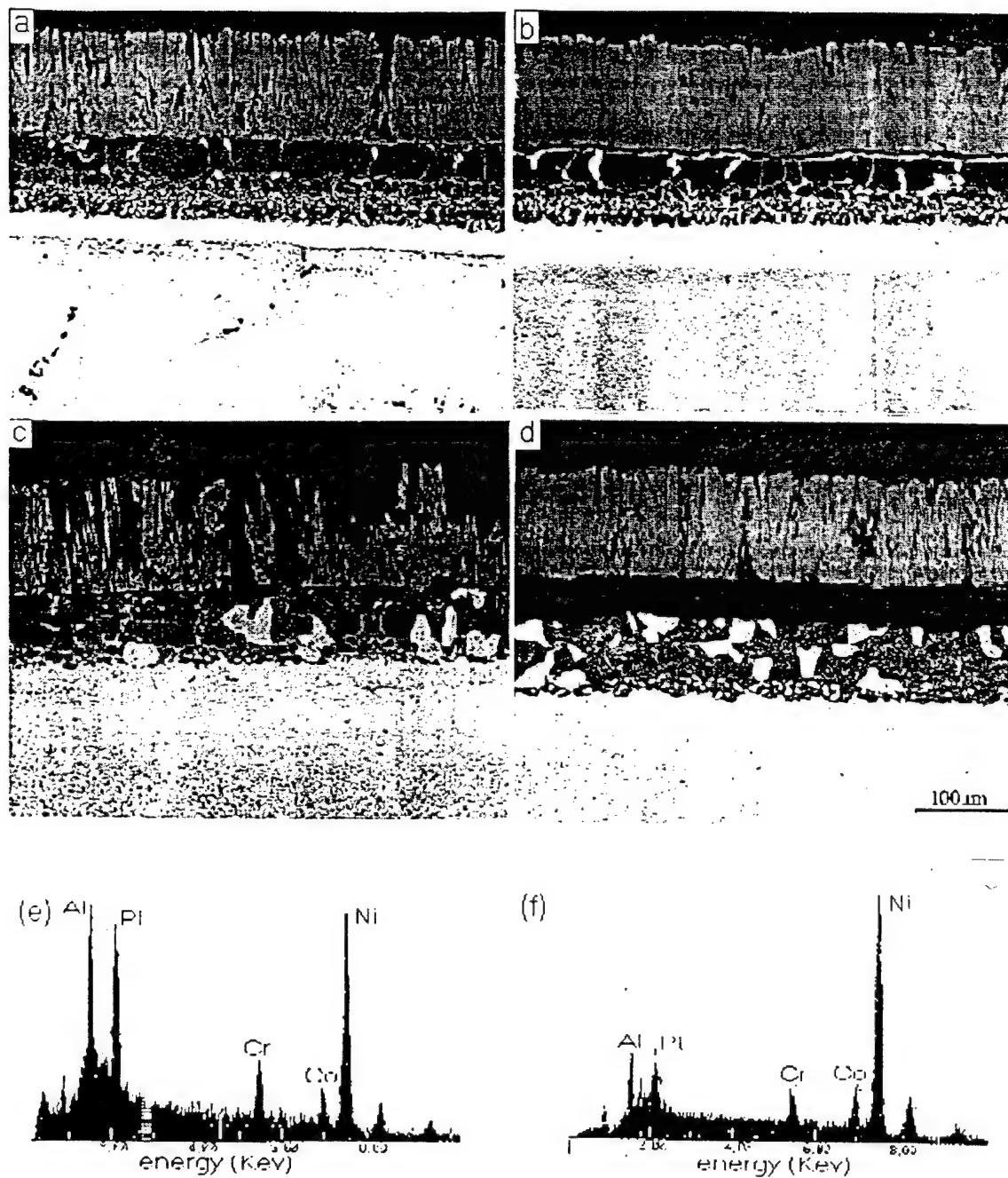


Figure 4.4 shows microstructure and composition of bond coat layer changed with increased thermal cycling at thermal test B. (a) 18 cycles, (b) 25 cycles, (c) 110 cycles, (d) 175 cycles, (e) composition of bond coat matrix, (f) composition of white precipitates.

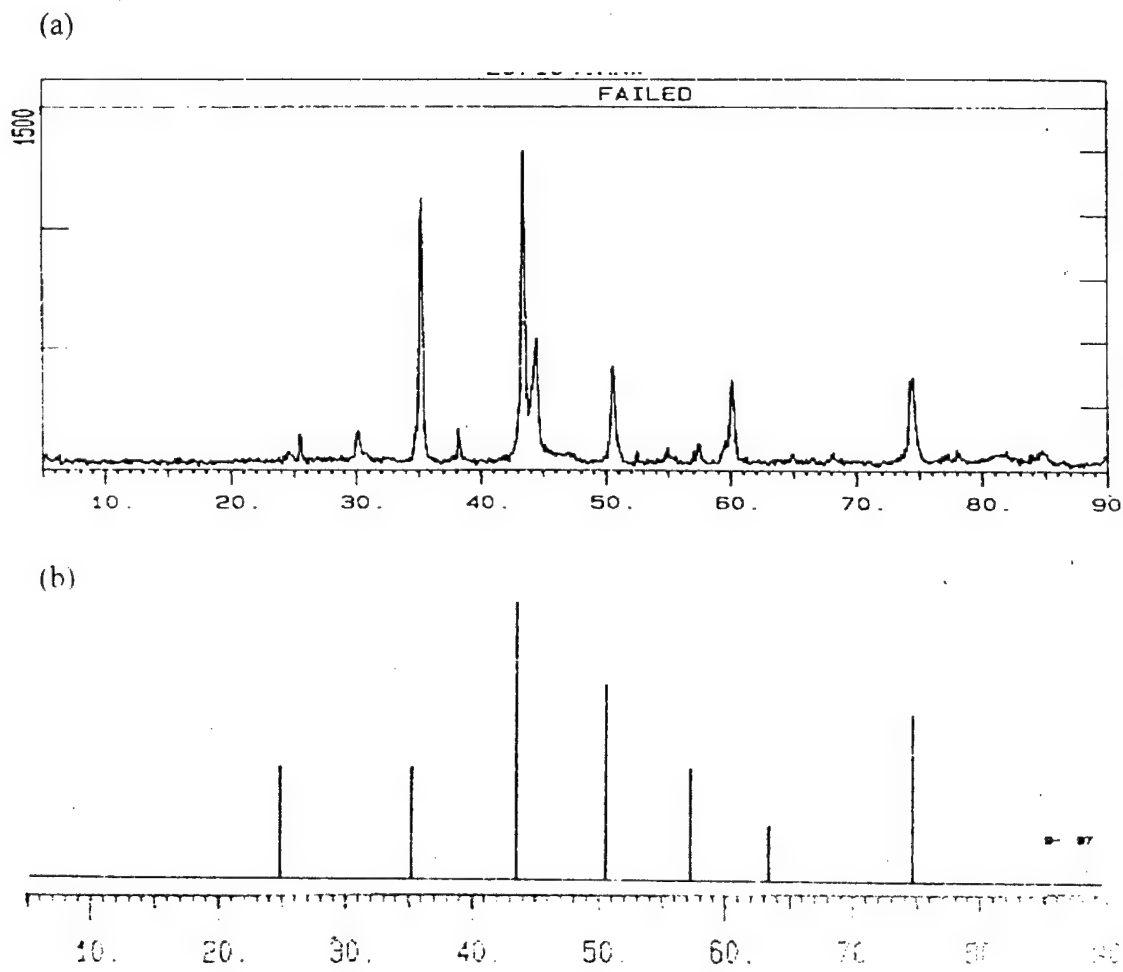


Figure 4.5 is x-ray diffraction pattern derived from the bond coat surface after TBC and TGO were removed at 180 cycles of thermal test B (a). (b) is standard pattern of  $\gamma'$ -Ni<sub>3</sub>Al phase (reference card number is 9-97).

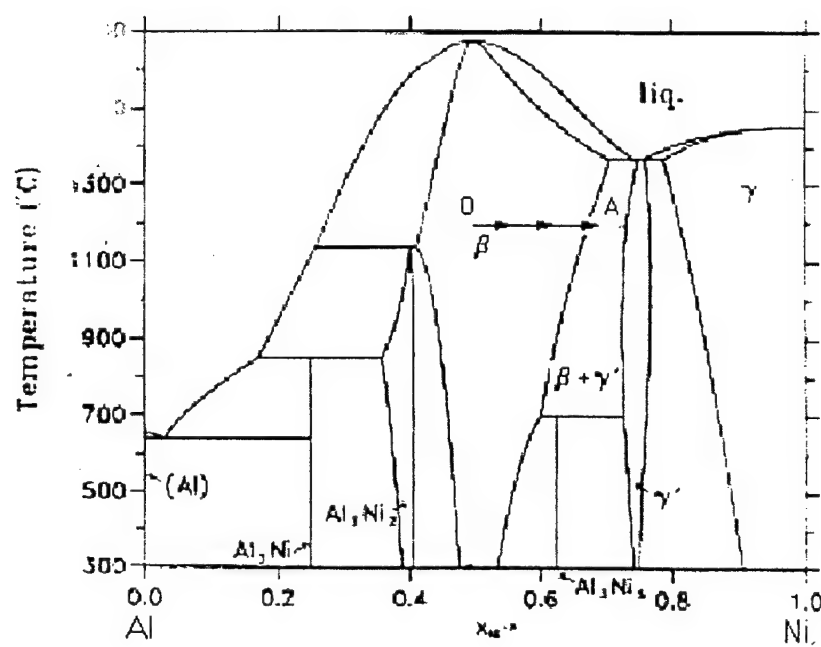


Figure 4.6 is Ni-Al system phase diagram. Composition of bond coat changed along  $O \rightarrow A$  path during thermal cycling at thermal test B.

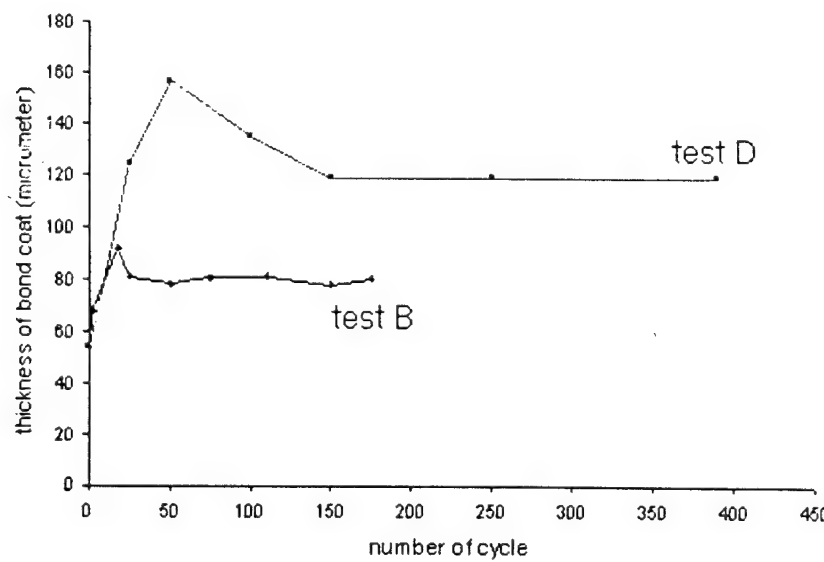


Figure 4.7 shows thickness of bond coat layer changed with increased thermal cycling at thermal test B and D.

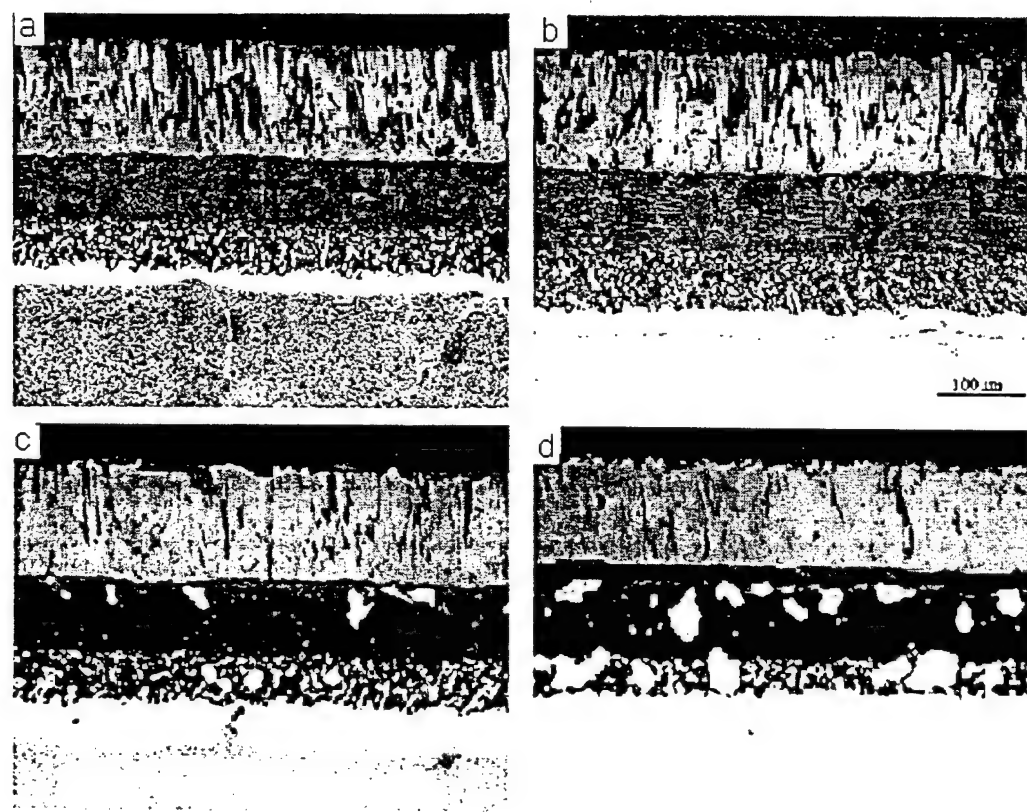


Figure 4.8 shows the microstructure evolves with thermal cycling at thermal test D  
(a) 25 cycles, (b) 50 cycles, (c) 100 cycles (d) 390 cycles.

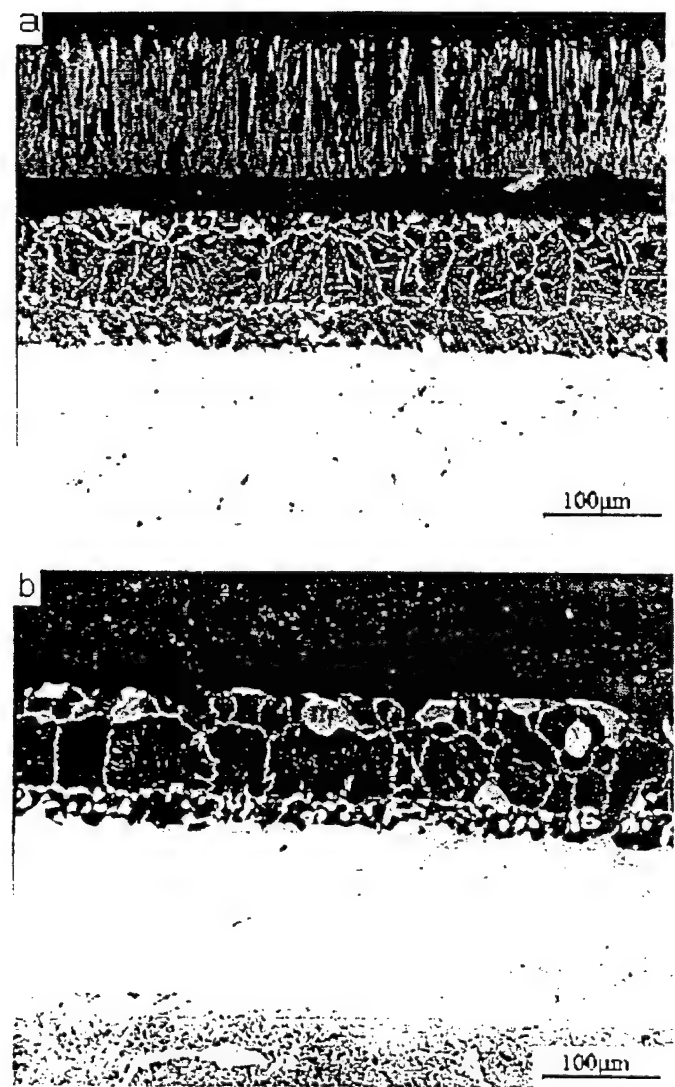


Figure 4.9 shows microstructure of bond coat at isothermal test. (a) 80 hours. (b) 150 hours at which the TBC spalled off.

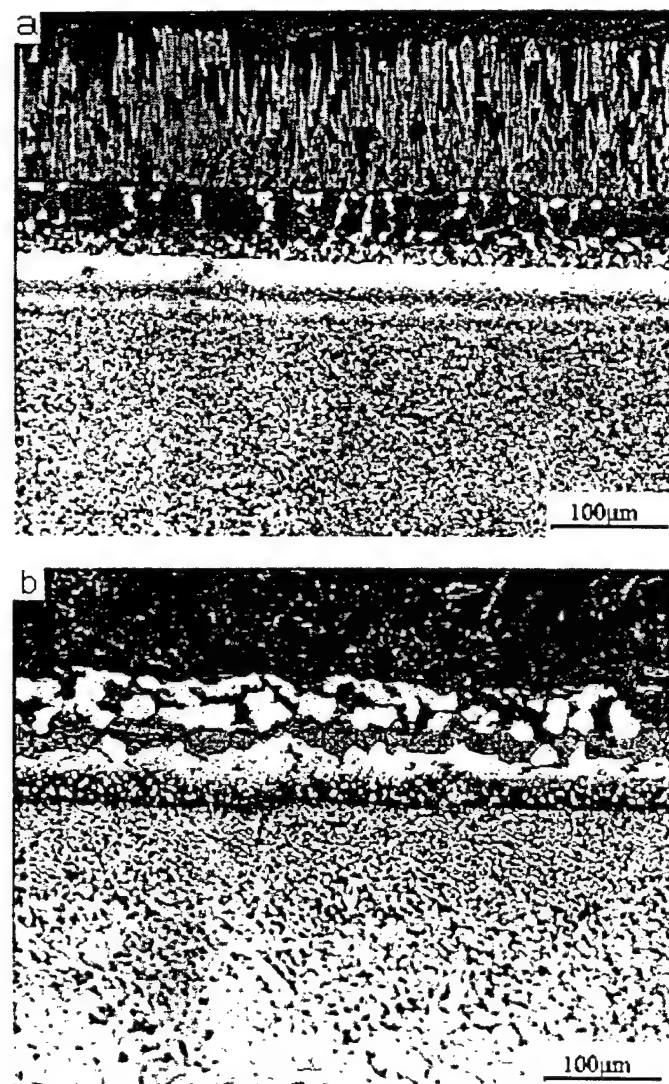


Figure 4.10 shows microstructure evolutes at thermal test C.  
(a) 100 cycles. (b) 550 cycles.

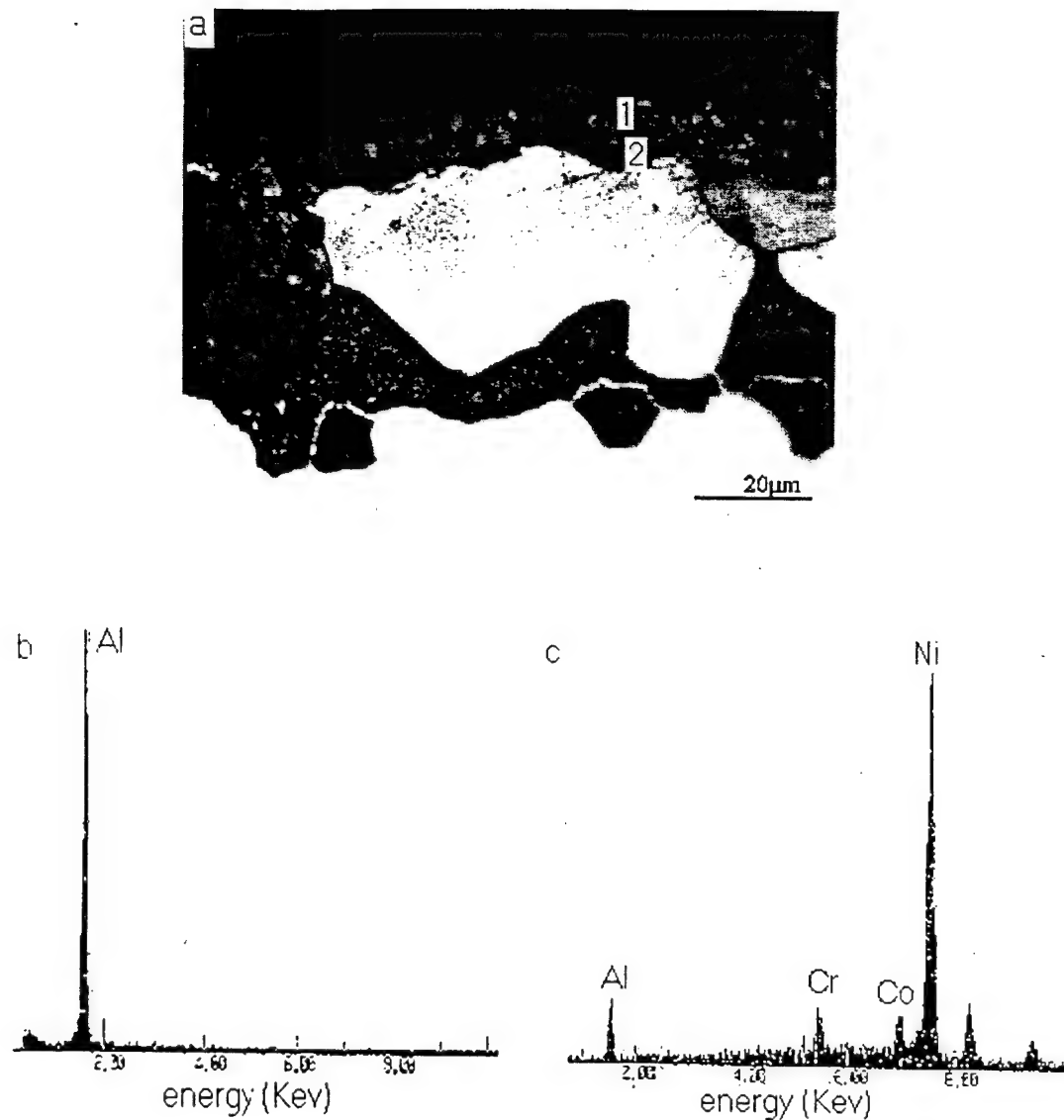


Figure 4.11 shows the microstructure of the cross section and EDS analysis after TBC spallation. (a) oxide formed at grain boundary of  $\beta/\gamma'$  (b) (c) are oxide composition of point 1 and 2, respectively. It shows Ni-rich oxide spinel formed in TGO layer.

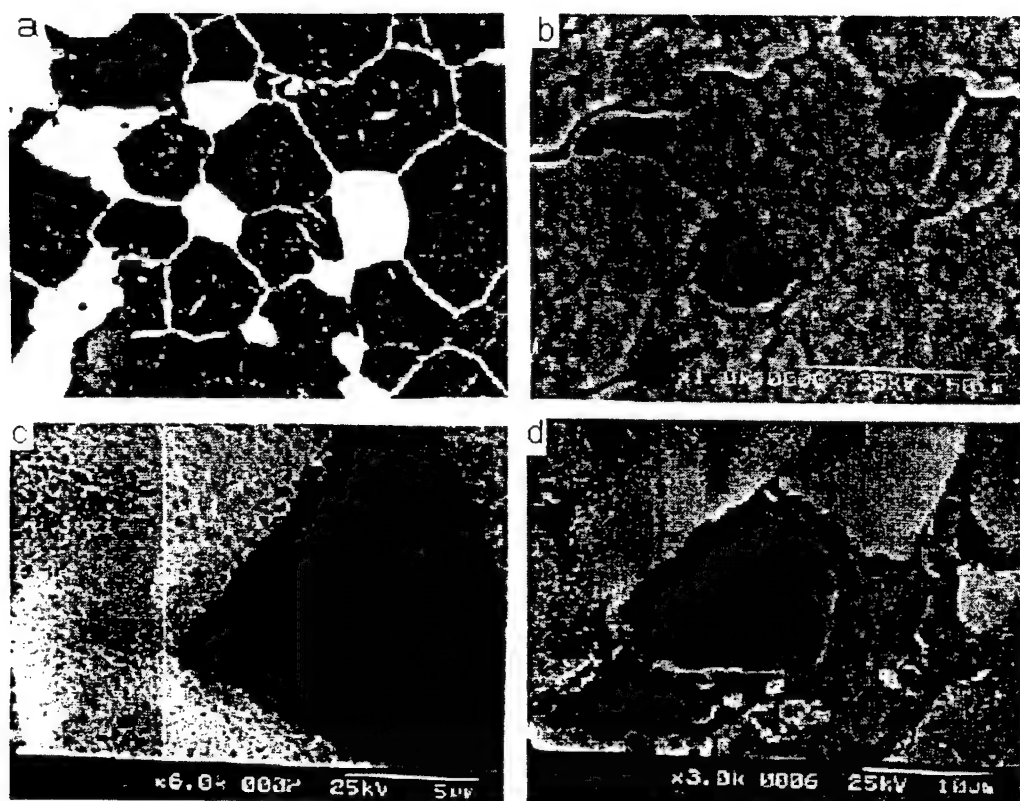


Figure 4.12 shows the effects of microstructure of bond coat on oxidation. (a) bond coat surface consisted of both  $\beta$ -(Ni, Pt)Al (dark) and  $\gamma'$ -(Ni, Pt)<sub>3</sub>Al (white) phases after 175 cycles at thermal test B. TBC and TGO layers were removed by polishing. (b) and (c) are microstructure of oxide scale at lower and higher magnification after 2 hours oxidation at 1177 °C. they show different microstructures of oxide on  $\beta$  and  $\gamma'$  phases. (d) Oxide spalled off from  $\gamma'$  phase and a cavity formed at interface, while oxide on  $\beta$  phase could survive.

## SSIVE DAMAGE EVOLUTION IN THERMAL BARRIER COATINGS

It is a common understanding that TBC fails by spallation along TBC/TGO or TGO/bond coat interface or in TGO layer. Although mechanics models are proposed to describe this condition in literature, the progressive nature of damage evolution leading to spallation has not been addressed adequately. In this chapter, damage evolution in the TBC system of partially stabilized zirconia /Pt-Al bond coat/ Nickel-based single crystal superalloy, Rene N5 will be investigated. In order to directly observe damage evolution in oxide, specimens without top TBC coating were used. Thermal cycles were imposed on button specimens. Different thermal cycles profile were used for damage evolution purposes. Progressive damage evolution was tracked using microscopy.

### 5.1 EXPERIMENTAL ASPECTS

Type 1 and type 2 specimen were used in this chapter. The purpose of using Type 2 specimen was to directly investigate the damage process of the oxide layer and associated microstructural features for different types of cycling condition. Specimens named as Type 3 were cut by half before the test. Type 3 specimens are used to directly observe the interface damage and prevent the effect of mounting and polishing.

Microstructures and damages of specimens were observed under Hitachi S-2400 Scanning Electron Microscope (SEM). To prevent an electron charge, a lower accelerate voltage and low filament current were used during observation.

## 5.2 RESULTS

Figure 5.1 shows the top surface of a type 2 specimen (without TBC coating) as received status (before thermal test). Grains of bond coat had a regular polyhedral shape. Thermally grown oxide (TGO) formed during the thermal cycle test. The oxide was identified as  $\alpha$ -Al<sub>2</sub>O<sub>3</sub> by x-ray diffraction (see chapter 5). The top surface of TGO shows different damage feature at different thermal test.

**1177-200 °C/45min thermal cyclic test.** Micrographs (Figure 5.2) of the top surface of the TGO layer at the type B thermal cyclic test (200-1177 °C/45-minute holding time at maximum temperature) show the initiation and evolution of large cracks at the impressions of the grain boundary of the bond coat with increased thermal cycles. The crack initiated at the very beginning of the thermal test. The cracks widened and propagated along the impression of the grain boundary of the bond coat with increased cycles. The lately formed oxide grew in the cracks (Figure 5.3). The thickness of the oxide around cracks was bigger than that of rest area and top surface of TGO layer became undulated. Similar cracks could be found at fracture surface of a failed TBC sample (Figure 5.4). At high magnification, the microcracks can be seen after 175 cycles

(Figure 5.5). However, no crack can be captured at top ceramic surface of typical TBC samples until failure (Figure 5.6).

The crack also can be observed from a cross section of typical TBC samples (Figure 5.7). The intergranular cracks of the bond coat layer can also be found after 110 cycles (Figure 5.8).

Type 3 specimens (cut by half before the test) were used to monitor the damage processing in TBCs. A non-thermally tested sample shows there was not any damage or interfacial separation in the sample after cutting. Local decohesions (separation) formed at the TBC/TGO interface (Figure 5.9), and there were intergranular cracks in bond coat layer (Figure 5.10). However, major delamination cannot be found in this thermal test.

A sample which experienced 50 thermal cycles in air was put into a vacuum tube and was thermally cycled at cycle B again. The top ceramic surface shows cracks at the impressions of the grain boundary of the bond coat the same as those in TGO (Figure 5.11).

**1177-500 °C/10min thermal cyclic test.** The top surface of the TGO layer at type C thermal test (500-1177 °C / 10 minutes holding time at peak temperature) shows microcracking was a major damage in TGO, while large cracks were not a major damage at this thermal test (Figure 5.12). The microcracks formed at the grain boundary of oxide and developed with thermal cycles, and finally, grains of oxide separate from each other.

The cross section of a type-3 sample (cut by half before the test) after 250 cycles shows local separations between TBC/TGO, and there were apparent marks of plastic deformation in the sample. The cross section surface of the sample was slightly polished

to remove oxide on the surface. Then it is clear that the deformation region was in the bond coat layer (Figure 5.13).

**Isothermal test.** The top surface of the TGO shows that the TGO was a very dense oxide layer, and few cracks can be observed at the top surface before failure (Figure 5.14). A cross section of a type 1 sample (normal TBCs) after an 80-hour thermal test shows voids and cavities formed at the TGO/bond coat interface (Figure 5.15), and those defects grew with increased oxidation time (Figure 5.16). Spallation of TBC occurred through the TGO/bond coat. Figure 5.17 also shows many voids and cavities at the fracture surface of failed TBC samples after 180 hours of isothermal exposure at 1177 °C

A type-3 sample (cut by half before the test) after 150 hours of isothermal oxidation at 1177 °C shows the TGO/bond coat interface cracked and the interfacial cracks associated with the grain boundary sliding of the bond coat.

**Interfacial separation of TBCs.** Pictures of the edge and the center of the TBC specimens at 0, 50, 75, 110 and 175 cycles of type-2 thermal test have been shown in Figure 5.18, respectively. All of those specimens were mounted by epoxy. The TBC started to bend at 75 cycles then the bend curvature increased with the number of cycles. A gap occurred in the TBC because of the separation between the TBC and the bond coat, and most of the oxide was lost by sample preparation after 50 cycles.

## 5.3 DISCUSSION

### 5.3.1 The Effect Of Plastic Deformation Of Bond Coat

The results have shown that the conditions of thermal test and bond coat plastic deformation strongly influence the damage characteristics in TBCs. It has been reported that the material of bond coat (NiAl) is an ordered intermetallic with a B2 (CsCl) crystal structure. It has been reported that a brittle-to-ductile transition (BDT) temperature is around 300 °C for polycrystalline NiAl (Noebe et. al., 1992; Miracle, 1993). Because of its high ordering energy, only three independent slip systems are available with  $\langle 100 \rangle \{0kl\}$  slip system below the BDT (Ball and Smallman, 1996), which is the primary slip mode in NiAl, while five independent slip systems are necessary for compatible deformation of neighboring grains (Bayer, et. al., 1999). Lack of enough independent slip systems leads to strain incompatibility between grains in polycrystalline NiAl. (Kad et. al. 1995) proposed that levels of deformation and stress of a polycrystalline microstructure, which has three allowed slip systems, can be orders of magnitude higher close to grain boundaries, and the degree of deformation inhomogeneity increases with an increase in the applied plastic strain. On the other hand, NiAl has an open grain boundary structure (Nadarzinski and Ernest, 1996; Yan, Vitek and Chen, 1996). This was attributed to the high ordering energy and caused low grain boundary strength in NiAl. The higher stress and low grain boundary strength led grains to slide into each other and even crack at grain boundaries while deforming below the BDT.

At temperatures above BDT temperature, dislocation climb and the activation of  $\langle 100 \rangle \{0kl\}$  slip system allows the strain compatibility problem to be overcome, and ductile deformation is expected (Noebe, et. al., 1991, Ebrahimi, 1997, Bayer et. al, 1999).

The difference of the plastic deformation mechanism of the bond coat due to BDT results in different damage characteristics of TGO.

When specimens were cooled from the peak temperature of the thermal test (1177 °C) to the temperature (200 °C or room temperature) below BDT temperature (~300 °C) of the bond coat (NiAl), sliding of the grain boundaries of the bond coat induced the stress concentration at the TGO/bond coat interface. The stress concentration at TGO/bond coat interface can be released by either interface cracking or TGO shear cracking. How the cracking develops depends on interfacial bond strength and the properties of oxide. At the early thermal cycle test, the TGO adhered to bond coat layer well the intergrainular cracks in the bond coat extended into TGO when the stress exceeded the shear strength of oxide and resulted in the TGO cracking at impression of the grain boundary of the bond coat. The oxide grew into cracks at high temperature and upon cooling the compressive stress in the far side of crack tip to develop a tensile stress at the crack tip. The cracks grew under thermal load. At the end of the isothermal test, the TGO/bond coat interface became very weak due to formation of voids, cavities and non-protective oxide at the interface (see chapter 3). The stress concentration released by interfacial cracking and debonding between TGO and the bond coat. The Figure 5.20 illuminates relationship between tendency of crack development and interfacial strength.

The cracking of TGO accelerated the inward diffusion of oxygen and outward diffusion of metallic elements (AL, Ni, ect.) along the cracks, which led to formation of

around the cracked area. Therefore, the interface undulation formed interface. The interface undulations could result in failure of et. al., 1998; Evans et al., 1999).

The accumulation of the local separation or decohesion during the thermal cycle test will gradually damage the TBC/TGO interface, weaken the interfacial strength and eventually result in TBC failure by buckling.

When specimens were cooled down to the 500 °C at thermal test C, which is above the BDT temperature of NiAl, the bond coat (NiAl) deformed uniformly under high residual stress. The cyclic deformation of the bond coat resulted in a rumpling of the bond coat and oxide. Tolpygo and Clarke (2000) investigated the effect of the surface rumpling of the bond coat and oxide layer during thermal cycling on the failure of TBC, and proposed that the surface rumpling of the oxide layer resulted in a geometrical incompatibility with the TBC and led to separation at the TBC/TGO interface.

The plastic deformation of the bond coat resulted in a tensile stress applied on the bond coat and bond coat/TGO interface at peak temperature (1177 °C) (see chapter 7). The high amplitude tensile-compression fatigue caused microcracking of TGO. The micraceracks developed at grain boundaries of TGO. The accumulation and link of grain boundary microcracking resulted in separation of oxide grains.

### 5.3.2 INTERFACIAL STRENGTH

The interface of the TBC/TGO or/and the TGO/bond coat was damaged during the thermal test. The damage accumulation weakened the adhesive strength of the TBC to the

bond coat. The adhesive strength can be expressed by the curvature of the TBC coat (the deflective distance of TBC) when the specimen was mounted by epoxy. The shrinkage occurs during the curing of the epoxy because of the rearrangement of polymer molecules into the more compact mass as the curing reaction proceeds. The volumetric shrinkage for cast epoxy is of 1-5% (allick, 1993). The most curing shrinkage happens before gelation (Lee et. al., 1967), and it does not cause much stress on specimens since it is still a liquid. However, volumetric shrinkage after the epoxy gelation will lead to an out-of-plane stress on the TBC surface due to a good adhesion of epoxy to ceramic. Once out-of-plane stress is equal or greater than the adhesive strength of TBC to TGO, the interfacial separation occurs. Previous works (Evans, et al 1999; He, 1997) indicated that a critical size of interfacial separation would result in compressed thin file buckling. TBC buckling did not cause its breakage because of mounting, but it led TBC to bend.

The out-of plane stress on the TBC surface increased with the development of epoxy shrinkage during curing. The higher bending curvature of TBC implies that the interfacial separation of TBC occurred at an earlier curing stage. Therefore, the curvature of TBC (the deflective distance of the center of TBC) can be used to represent the adhesive strength of TBC. The results show that the interfacial adhesive strength decreased with increased thermal cycles, which is in agreement with the result measured by directly pull test (Gell, 1997).

#### 5.4 SUMMARY

The following summary can be made:

1. The TGO layer and the bond coat were subjected to high residual radial stresses during cooling from oxidation temperature. The residual stress was higher than the yielding strength of the bond coat and caused plastic deformation of the bond coat.
2. The minimum temperature at thermal cycling influenced the mechanism of plastic deformation of the bond coat and damage feature in the TGO layer. When specimens were cooled from peak temperature of thermal cycling to the temperatures 200 °C or room temperature, which are below BDT temperature (~300 °C) of the bond coat (NiAl), the grain boundaries slid and induced the stress concentration at the TGO/bond coat interface.
3. The stress concentration at the TGO/bond coat interface resulted in cracking the TGO layer. When specimens were cooled down to 500 °C at thermal cycling, which is above the BDT temperature of NiAl, the bond coat (NiAl) performed ductile deformation under high residual stress.
4. The cyclic deformation of the bond coat resulted in a rumpling of the bond coat and oxide. The cyclic thermal load led to microcracking in the TGO layer during thermal cycling.
5. The cracking, microcracking and surface rumpling in the TGO layer resulted in local loss in adhesion of the coating.

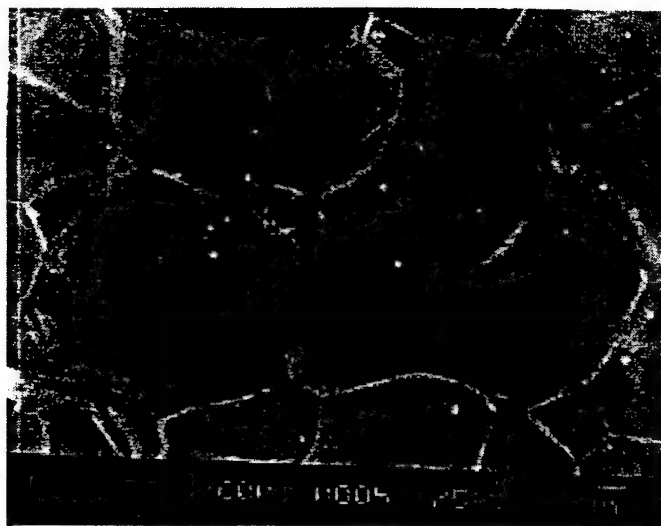


Figure 5.1 shows the micrograph of bond coat layer at untested condition.

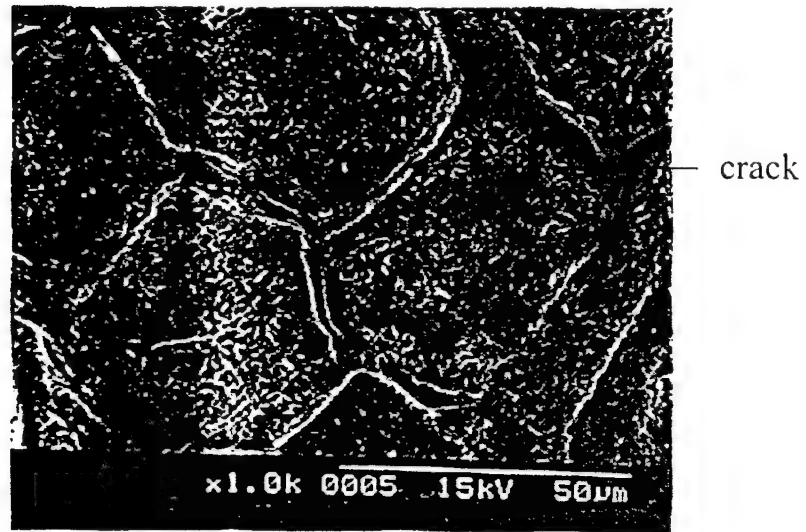


Figure 5.2(a) shows the top surface of type 2 specimen after 25 B cycles. Cracks formed at the impression of bond coat grain boundary.

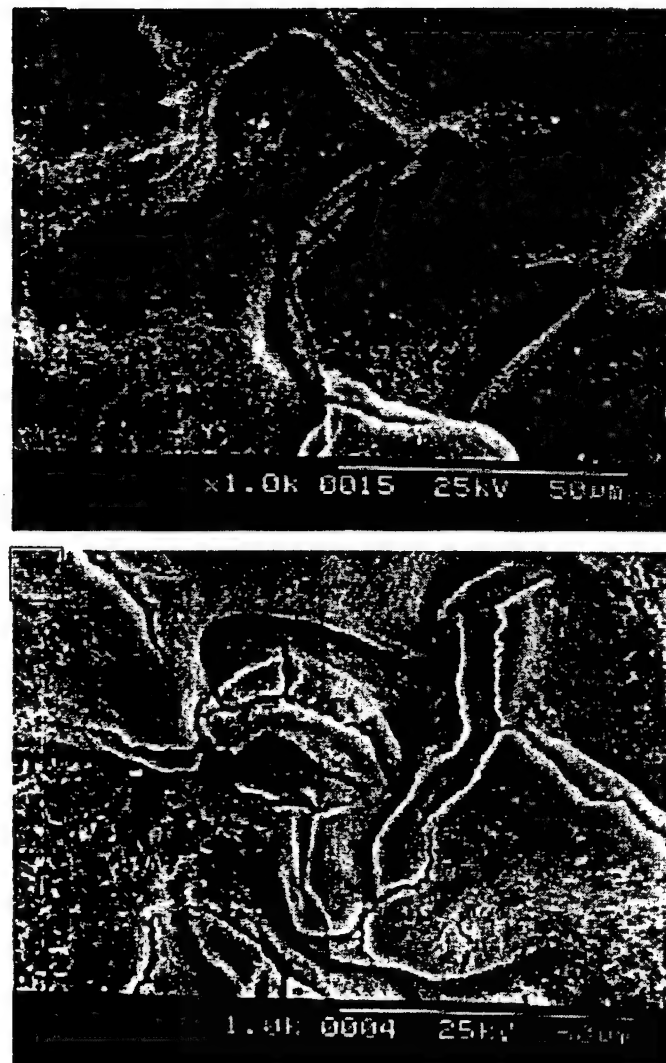


Figure 5.2 (continual) shows the top surface of type 2 specimen after 75 and 150 B cycles. Cracks increased and grew at the impression of bond coat grain boundary.

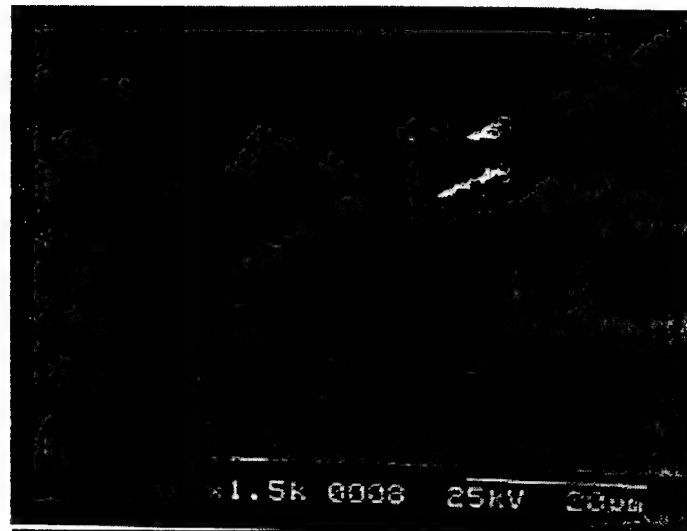


Figure 5.3 shows top surface of type 2 specimen after 175 B cycles. Oxide grew in TGO cracks and formed undulation around cracks.

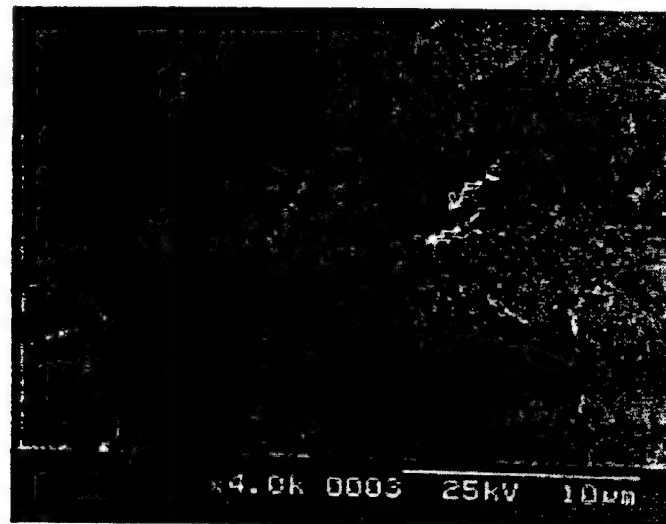


Figure 5.4 shows the fracture surface of TBCs after 180 B cycles. The cracks in TGO layer show same character as cracks in type 2 specimen.

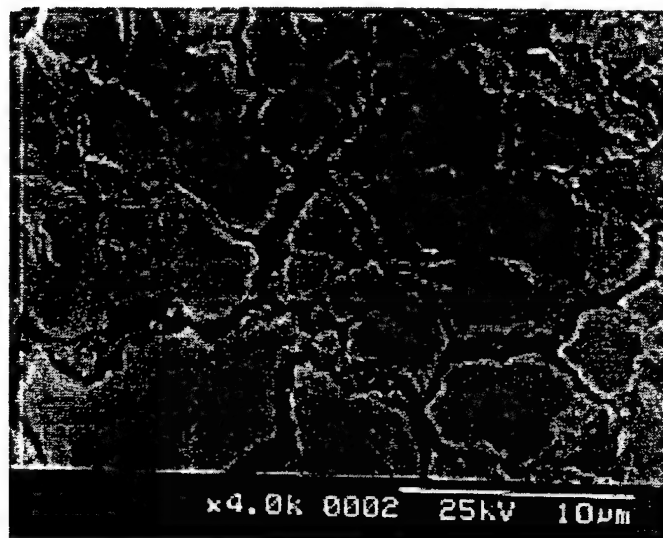


Figure 5.5 shows micocracks at oxide grain boundaries in type 2 specimens after high number of type B cycles (175 cycles)

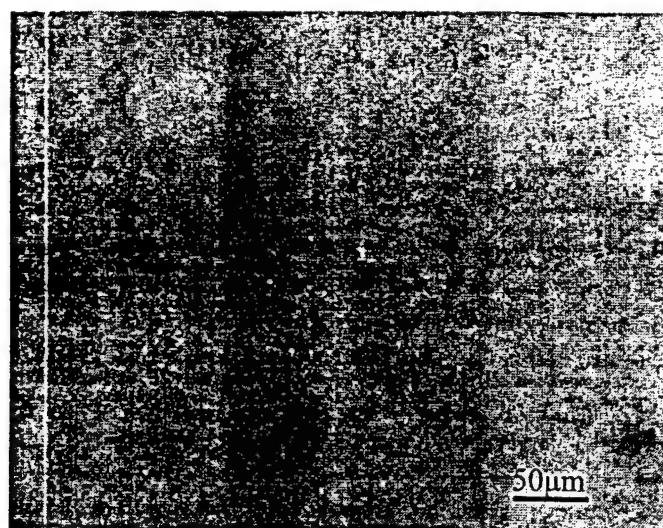


Figure 5.6 shows a top surface of a TBCs specimen after 150 B cycles. No crack can be seen.

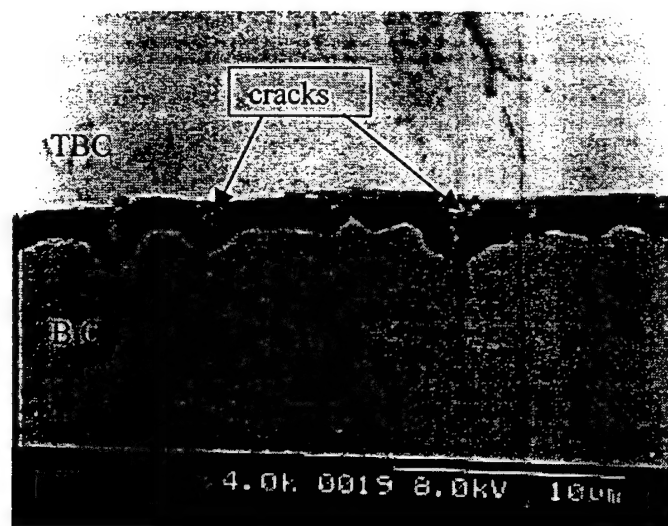


Figure 5.7 shows cracks in TGO layer of TBCs specimen after 2 B cycles. Those cracks were associated with sliding of grain boundary of bond coat.

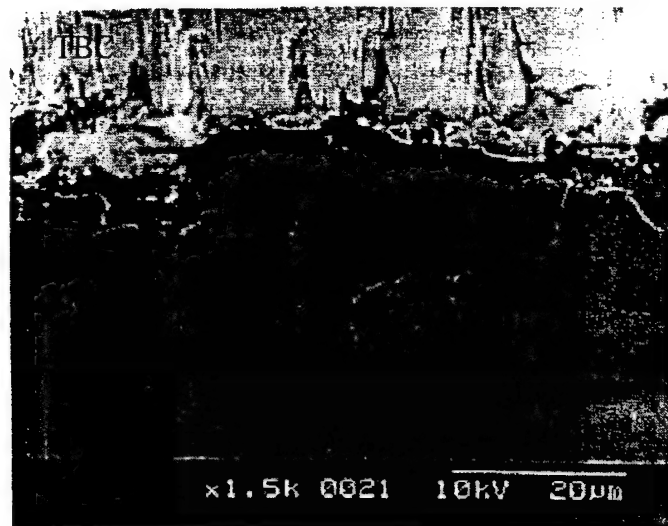


Figure 5.8 shows intergranular cracks of bond coat in a TBCs specimen after 110 B cycles.

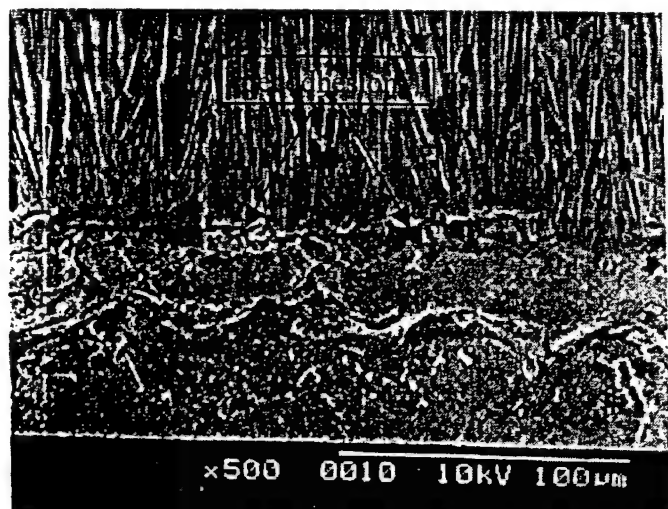


Figure 5.9 shows local decohesions at TBC/TGO interface in a type 3 specimen after 150 B cycles. But major delamination cannot not be found.

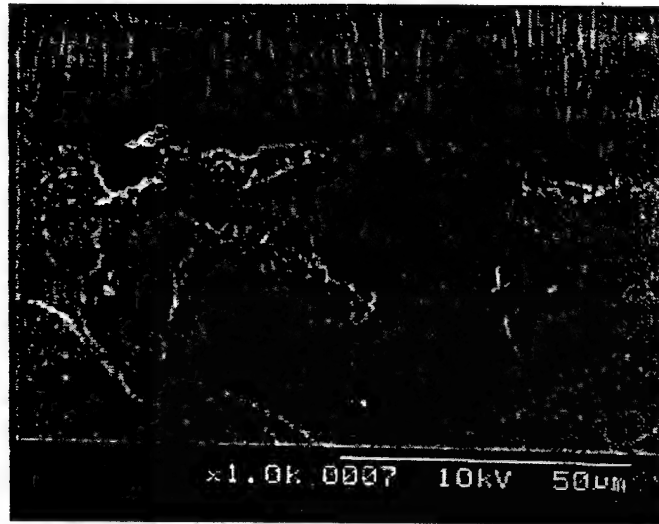


Figure 5.10 shows intergranular cracks of bond coat and decohesion at TBC/TGO interface in type 3 specimen after 150 B cycles

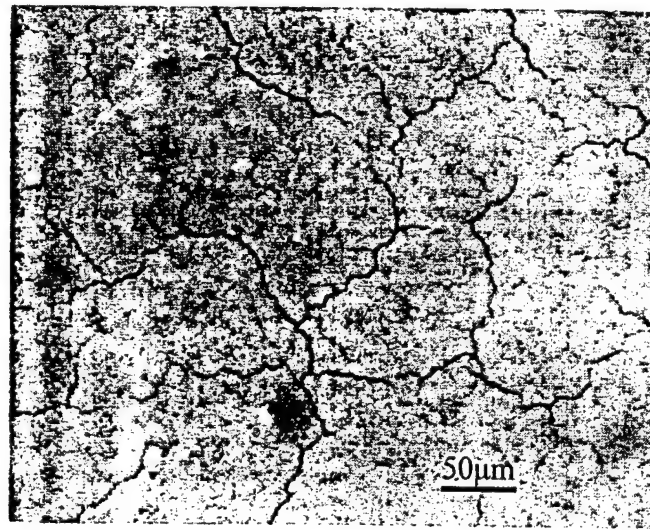


Figure 5.11 shows micrograph of top surface of a TBCs specimen, which was thermal cycled at type B to 50 cycles in air and then 350 cycles in vacuum. The cracks formed at thermal cycling in vacuum, and those cracks formed at impreesion of grain boundary of bond coat same as that seen in TGO.

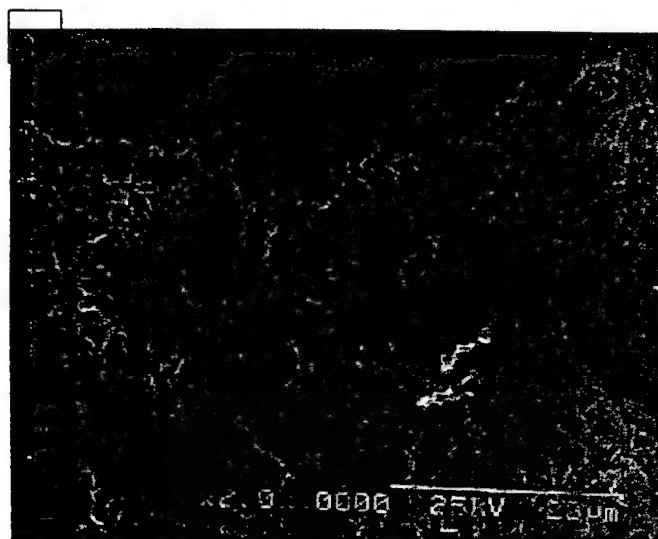
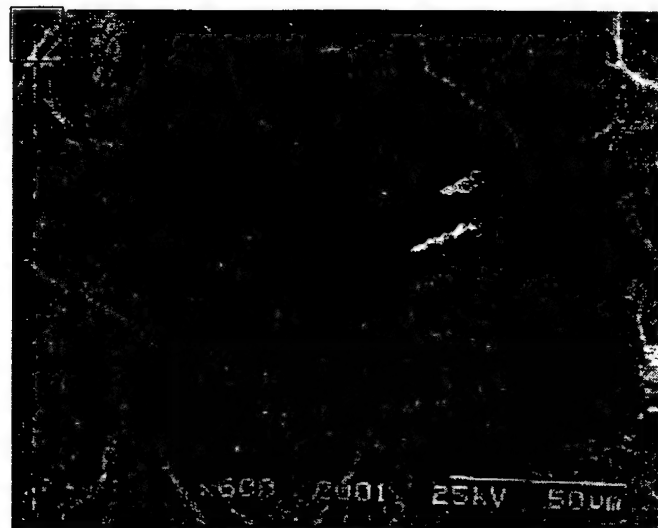


Figure 5.12 shows the micrographs of top surface of a type 2 specimen after 550 C cycles. Large crack are not seen as that found in type B test (a). But the oxide grain boundary separation (b) is found almost all over the TGO surface.

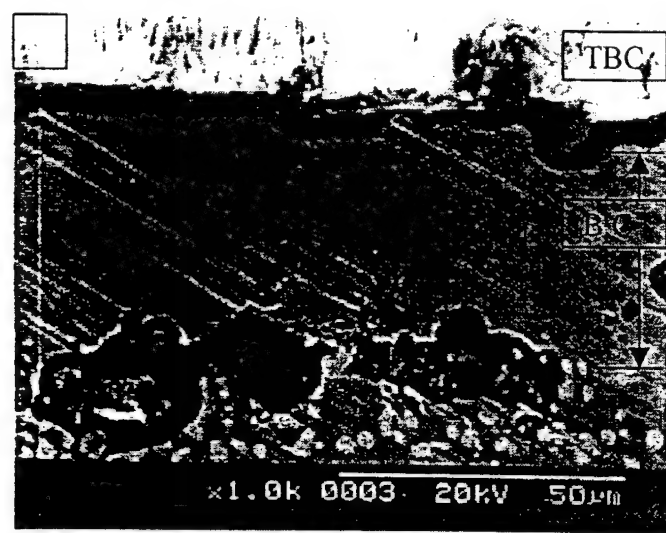
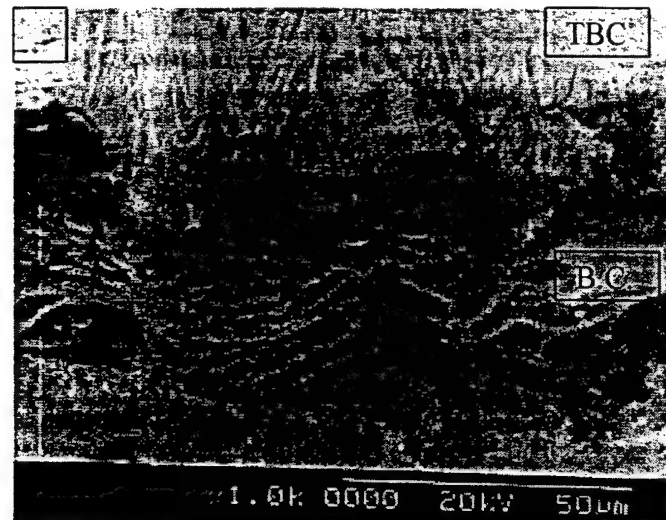


Figure 5.13 shows the cross section of type 3 (cut by half before test) after 250 C cycles. The deformation marks shows uniformly plastic deformation occurred in bond coat at C thermal cycling. (a) as-tested; (b) slightly polished.

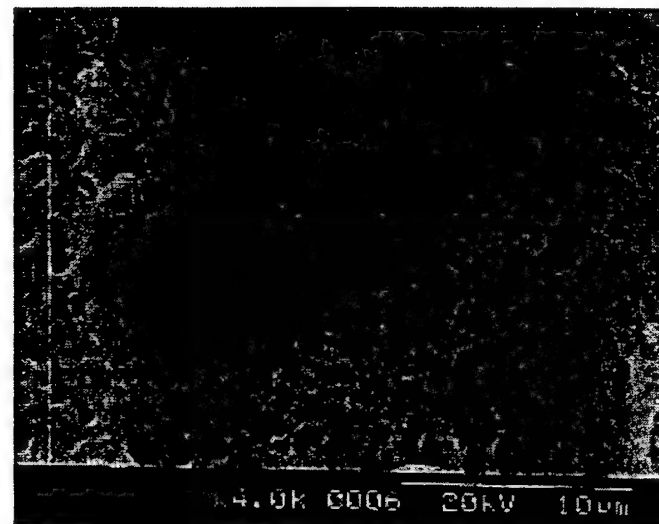


Figure 5.14 shows micrograph of top surface of a type 2 specimen after 150 hours isothermal exposure in air. There is not any crack at top surface of TGO.

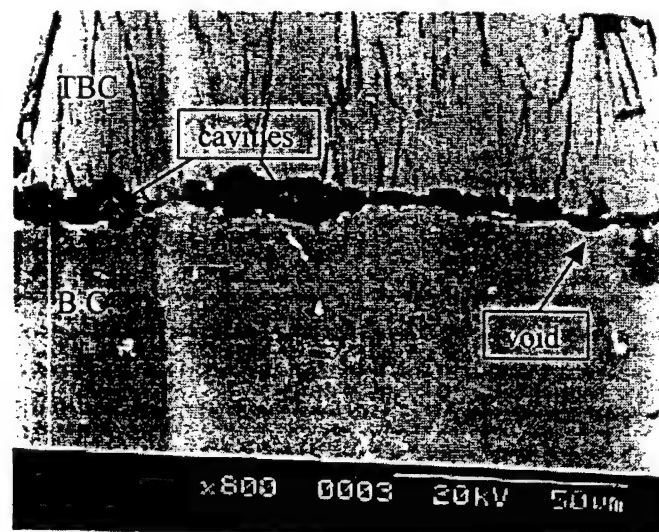


Figure 5.15 shows micrograph of the cross section of a TBCs specimen after 80 hours isothermal exposure in air. Voids and cavities formed at TGO/bond coat interface.

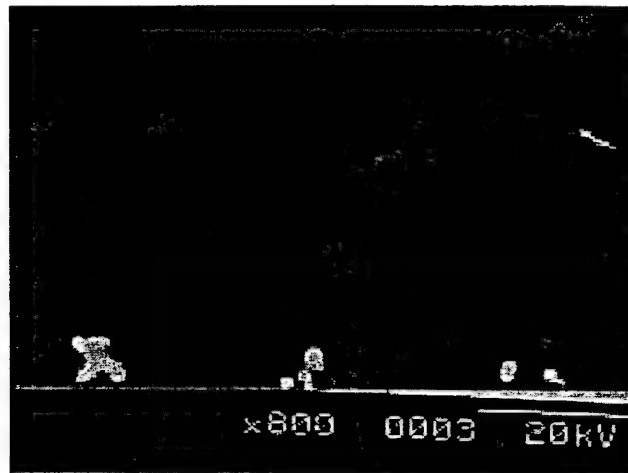


Figure 5.16 shows the cross section of a failed specimen after 180 hours isothermal exposure in air. Cavities grew bigger at TGO/bond coat interface.

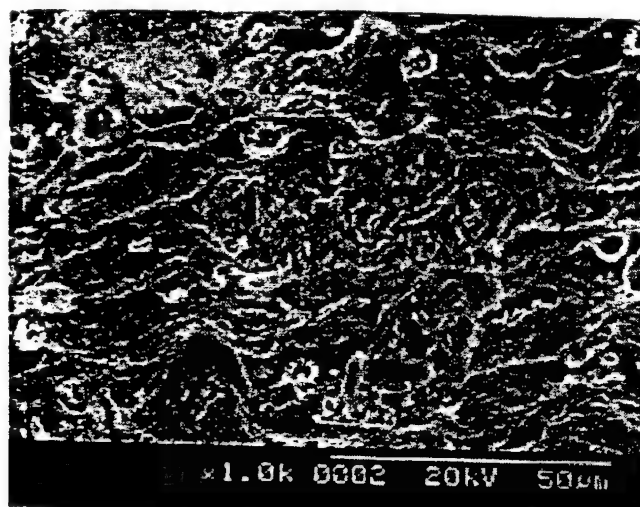


Figure 5.17 shows micrograph of the fracture surface of failed TBCs specimen after 180 hours isothermal exposure in air. Many voids and cavities formed at the fracture surface.

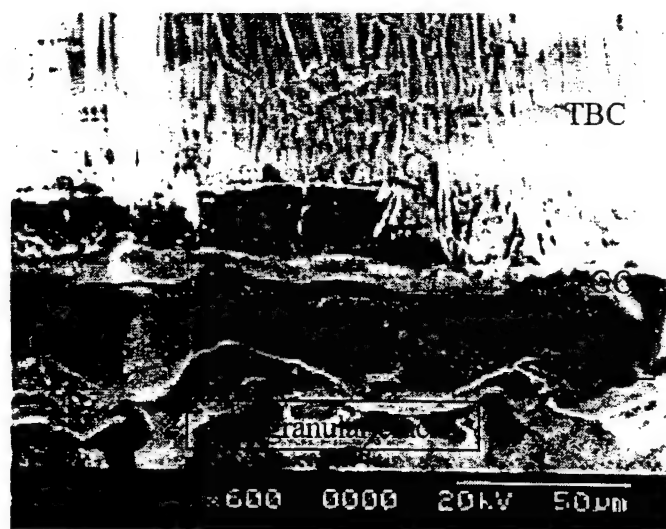


Figure 5.18 shows the cross section of a type 3 specimen after 150 hours isothermal exposure in air. TGO/bond coat separation was initiated by intergranular crack of bond coat.

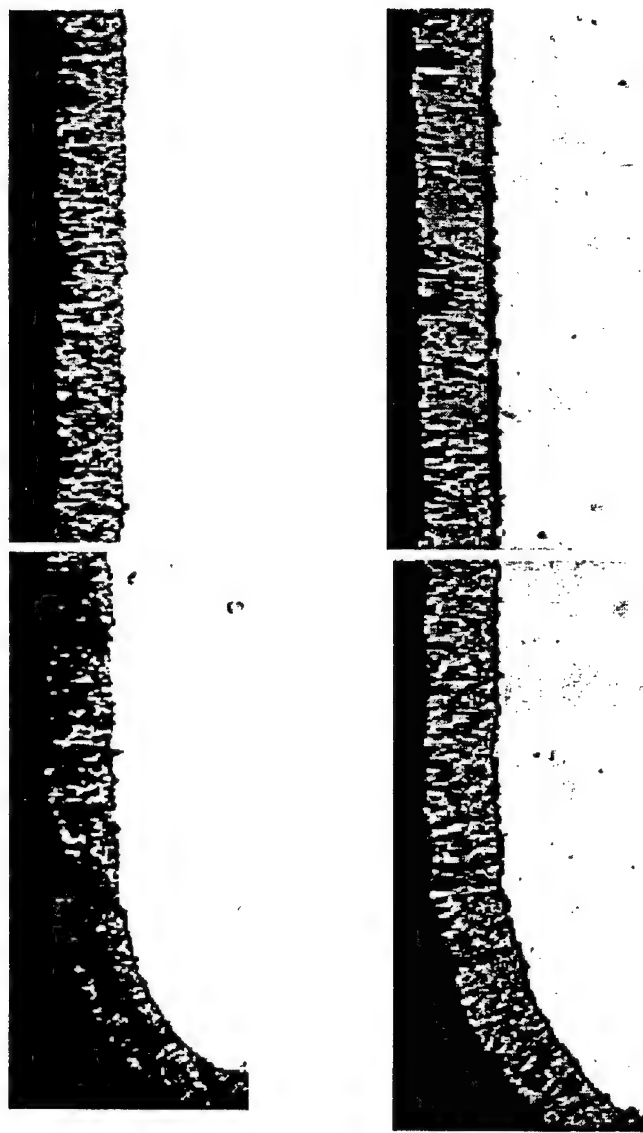


Figure 5.19 shows cross section of TBCs after various numbers of cycles of thermal cycle B. The specimens were mounted by epoxy.  
(a) there was no separation between TBC and bond coat after 50 cycles; (b) Separation between TBC and bond coat can be shown after 75 cycles

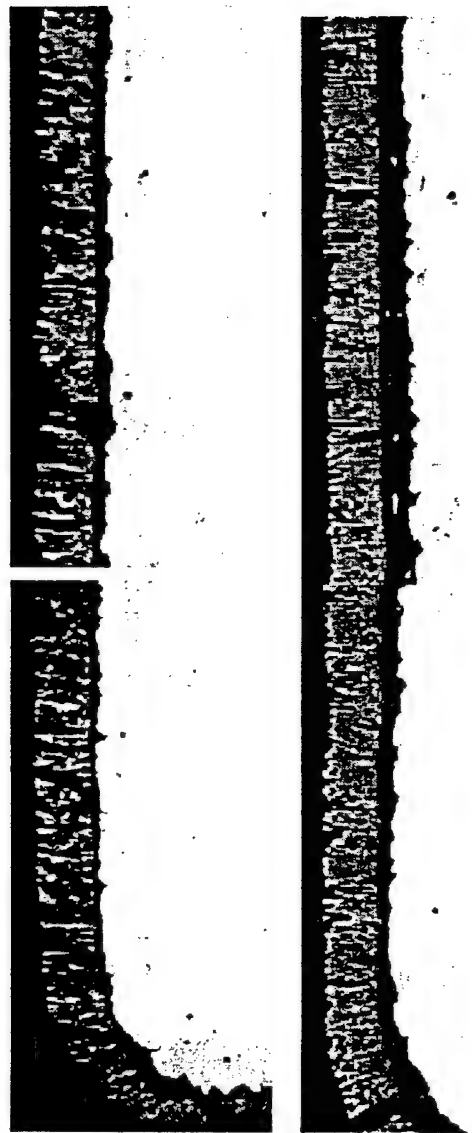


Figure 5.19 (continual) shows cross section of edge and center of TBCs after various numbers of cycles of thermal cycle B. The separation distance between TBC and bond coat increased with increased number of cycles. (a) 110 cycles; (b) 175 cycles.

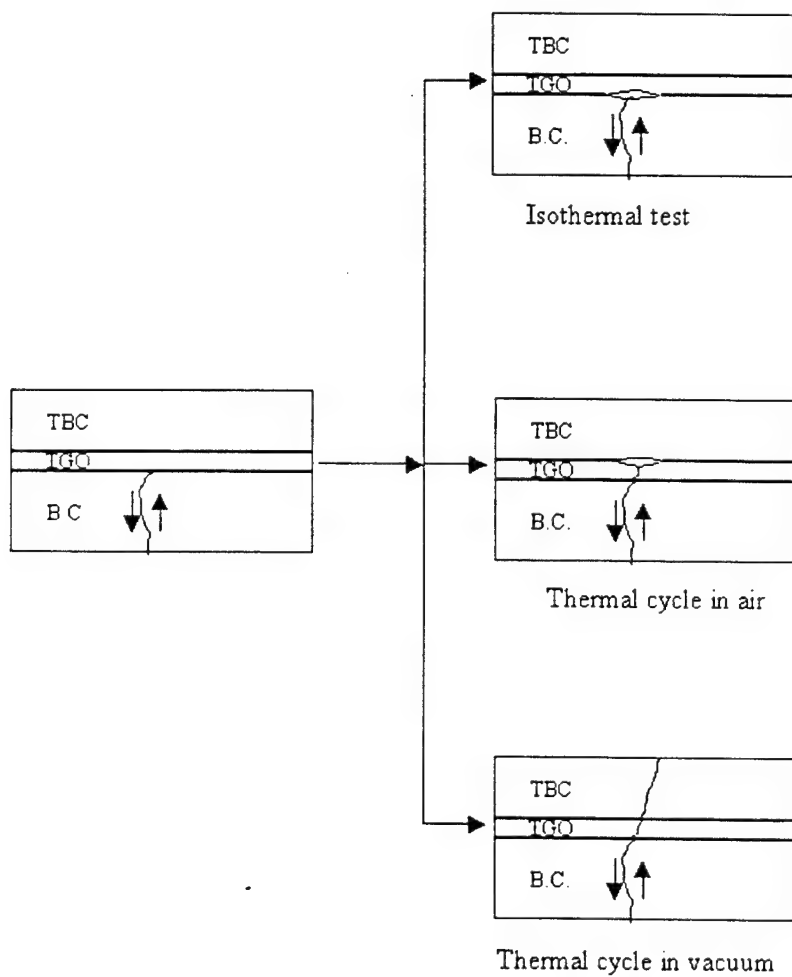


Figure 5.20 schematically shows the influence of interfacial strength on crack development induced by grain boundary sliding of bond coat in TBCs.

## 6.0 NONDESTRUCTIVE EVALUATION

The thermal barrier coatings fail due to the accumulation of progressive damage at the TBC/TGO interface, and/or TGO/bond coat interface. Direct put-off, indent and acoustic emission are currently used to characterize interface of coatings or thin film (Gell, 1997; Wang and Evans, 1998; Tolpygo and Clarke, 2000; Fu et. al., 2000). All of those are considered as destructive methods. Even acoustic emission is also a contact method. Thermal wave imaging as a non-contact evaluation method has high potential to monitor the health of TBCs in aircraft engines.

### 6.1 PRINCIPLE OF THERMAL WAVE IMAGING

In-a-Pulse-echo Thermal Wave IR Image System, a pulse of heat is launched to specimens by flash lamps and surface temperature distribution of the specimen is monitored as a function of time by an infrared camera.

The surface temperature of specimens increases very steeply during the exciting pulse. Then the deposited energy diffuses progressively into the specimen by conduction. Heat flux in the material is following the equation 6.1. Here only one dimension of heat flux is considered.

$$F = -\kappa \frac{dT}{dx} \quad (6.1)$$

Where  $F$  is heat flux;  $\kappa$  is thermal conductivity of the material;  $T$  is temperature at  $x$  direction of heat transportation.

The temperature distribution follows the thermal diffusion equation

$$\nabla^2 T(x,t) = \frac{1}{a} \frac{\partial T(x,t)}{\partial t} \quad (6.2)$$

where  $a$  is thermal diffusion coefficient, which can be expressed by two material parameters: the specific heat capacity  $c$ , and the density of the material  $\rho$ .

$$\alpha = \frac{\kappa}{\rho c} \quad (6.3)$$

The specimen is considered as semi-infinite body in this work since only a small amount of pulse heat energy is deposited to the specimen, and the initial temperature of the specimen is assumed to be zero. So we have initial and boundary conditions:

$$T(x,t) = 0 \quad (6.4)$$

$$T(\infty,t) = 0 \quad (6.5)$$

$$-\frac{\partial T(0,t)}{\partial x} + HT(0,t) = 0 \quad (6.6)$$

The solution (Luikov, 1968) of equation 6.2 at the initial and boundary conditions is

$$T(x,t) = \frac{Q}{\rho c (4\pi\alpha t)^{1/2}} e^{-\frac{x^2}{4\alpha t}} \quad t>0 \quad (6.7)$$

where the amount of heat is evolved by a pulse.

Therefore, the surface temperature after excited pulse follows this law:

$$\Delta T = \frac{Q}{\rho c \sqrt{4\pi\alpha t}} \quad (6.8)$$

Thermal wave imaging for non-destructive testing of materials is based on the fact that defects in a material generally have a thermal conductivity difference from that of the bulk materials. Heat, therefore, flows differently through the defect area than through the bulk. Differences in the heat flow result in differences in temperature distribution on the surface of the sample.

## 6.2 THERMAL CONTACT RESISTANCE CONCEPT IN BIMATERIAL

If the interface of a bimaterial is not a perfect bond, there are some non-contact spots at the interface. The remainder of the space between the non-contact surfaces may be filled with air or another fluid or may even be a vacuum. When heat flows from one solid to the other, heat flow paths converge toward the actual contact area since the thermal conductivities of solids are generally greater than those of fluids (Kakac and Yener, 1993). This creates an additional resistance to the heat flow at the interface. Figure 6.1 schematically shows the temperature drop at an interface due to thermal contact resistance.

At the interface of a bimaterial, a contact coefficient is defined as

$$h_c = \frac{Q/A}{\Delta T} \quad (6.9)$$

where  $Q/A$  is heat flux across the interface and  $\Delta T$  is the temperature drop. A thermal contact resistance can be defined as

$$R_c = \frac{1}{h_c A} \quad (6.10)$$

Therefore, the temperature discontinuity in the non-ideal interface between substrate and coating can be expressed as

$$T_c - T_s = R_c Q \quad (6.11)$$

If the interface separation is big enough, the IR camera is able to catch the temperature discontinuity as a distinguished area. Or the echo of the thermal waves produced by temperature discontinuity results in a slower heat flux in specimen.

The characteristic time of heat diffusion (Martinsons and Heuret, 1998) is

$$t \approx \frac{l^2}{\alpha} \quad (6.12)$$

where  $l$  is the thickness of the TBC coat and  $\alpha$  is the thermal diffusivity of TBC ( $5 \times 10^{-7} \text{ m}^2/\text{s}$ ).

### 6.3 EXPERIMENTAL ASPECTS

Regular TBC specimens (Type 1) were used in this chapter. The damage processes and failure at thermal test A or B were monitored by thermal wave imaging technique.

The setup of thermal wave imaging is shown in figure 6.2. It consists of flashlights, an IR camera, a computer and an intelligent system controller (ISC). The picture of Echo Therm ® 32 System Hardware used in this work is shown in figure 6.3. Both thermal wave image and surface temperature profiles were taken to monitor the health of TBC. The spatial resolution of images of the system is 0.5 mm in the working condition. In order to capture interface damage in TBCs, the images and surface temperature profile plots were taken at 0.004 s after flashing.

### 6.4 RESULTS AND DISCUSSION

#### 6.4.1 INTERFACE SEPARATION IN TBCS

Figure 6.4 shows a series of images of a TBC specimen at various numbers of thermal cycles. The results have shown that two interface separations occurred after only two cycles. The impurity of the metallic surface may result in early interface separations. The dimensions of the two separations are 8.255 mm x 2.8575 mm and 1.058 mm x 1.058 mm, respectively. But the specimen did not show any buckling until failure. Both of the interface separations did not propagate with increased cycles. This specimen failed at 167 cycles compared with the average TBC lifetime of 175 cycles. The results reveal that the

small manufactural defects do not have a significant effect on the lifetime of the disc specimen.

Figure 6.5 shows corresponding thermal wave signal amplitude profiles as a function of position across a line of the specimen. The analysis line was crossed through the interface separations (Figure 6.4). The signal amplitude of thermal wave represented the surface temperature of specimen. The undulations on the curves after two cycles show that the temperature of the interface separations was higher than temperature at rest area of the specimen. The average surface temperature of the specimen increased with thermal cycles.

The surface temperature of the specimen at the interface separation area and the non-defect area (as a reference) as a function of time was recorded by the system during thermal wave imaging (Figure 6.6). This result shows that the cooling rate of the surface temperature on the separation area was less than the reference area, which consisted of no interface separation.

Figure 6.7 shows a three-dimensional picture of the surface temperature of the specimen with manufactural defects at 0, 2, 165 thermal cycles and after failure at 167 thermal cycles, respectively. The interface separation can be identified by the 3-D surface temperature profile. The interface separations formed at 2 thermal cycles did not grow with increased thermal cycling, while a edge delamination occurred at 165 thermal cycles. Final failure occurred by linking edge delamination and interface separations, and propagation through the whole specimen.

## SSIVE DAMAGE IN TBCS

of thermal wave images and corresponding surface temperature profile plots. Normal TBC specimen were taken at various thermal cycles (0, 25, 50, 110, 141, 156 cycles) (Figure 6.8). The images show there was not a major interface separation in the TBCs until failure. The specimen failed at 156 cycles after overnight exposure to ambient air. The surface temperature profile plots indicates that the thermal wave signal amplitude increased rapidly from 0 thermal cycles to 25 thermal cycles (about 100% change). Then the thermal signal amplitude increased gradually with thermal cycles. The total change in thermal signal amplitude was about 150% until at 156 thermal cycles. The thermal wave signal amplitude rose sharply after failure. Figure 6.9 shows the relationship of surface temperature with the number of thermal cycles. It indicates that the thermal signal amplitude increases with increased number of cycles and reaches a steady value at a higher number of cycles.

The results from the thermal wave imaging method are in strong agreement with observations by microscopy. The TBC coat was bonded well to the substrate by a very thin oxide layer (Figure 6.10). The interface damage formed at only two cycles during thermal cycling (Figure 6.11). The damages (cracks) progressively grew with increased cycles (Figure 6.12). The progressive damage led local loss in adhesion of the coating and increases of thermal contact resistance in TBCs. Final failure occurred due to low interface fracture toughness and high thermal residual stresses (Mumm and Evans, 2000).

### 6.4.3 TBC BUCKLING AND SPALLING

The final failure processing of a TBC specimen was monitored by thermal wave imaging (Figure 6.13). The specimen was cooled down to 100 °C at room temperature following isothermal exposure at 1177 °C in air. Then the specimen was placed under the IR camera of thermal wave imaging and took images.

A small separation with size 1.4 mm in diameter formed at the beginning. The separation did not grow until the temperature reached room temperature. The separation suddenly grew and buckled at a moment between the two measurements. Unfortunately, the initial propagation of the interface separation was not obtained. The buckle propagation and spallation were monitored. The buckle grew in “telephone cord” morphology (Evans and Wang, 1998) instead of a circle. The side edge of the buckle was arrested. The width of the buckle along the strait edge was 4.27 mm that could be used to define the critical size for buckling (Choi et al 1999). For films subject to biaxial compression, the critical circular separation size  $b_b$  for buckling is (Evans et. al., 1997)

$$b_b = 1.11h \sqrt{\frac{E}{(1-\nu)^2 \sigma_b}} \quad (6.13)$$

where  $b_b$  is the critical separation radius,  $\sigma_b$  is compressive stress, E and  $\nu$  are Young's modulus and Poisson's ratio of the film, and h is its thickness.

The critical separation radius for TBC cooling from 1177 °C to room temperature is about 16 times the thickness of the TBC coat, which is 2.032 mm in radius or 4.064 mm in diameter (Nusier, 1997). This size is comparable to the width of buckle along propagation direction (4.27 mm) observed by thermal wave imaging.

Cracks formed at the middle of the buckle along the buckling propagation direction. Wang and Evans (1998) investigated the buckling processing of the thin film (TGO), and proposed that the bending deformations cause tensile stress in the TGO. If these stresses exceed the flexural strength of the thin film (alumina), cracks form. TBC has a very low tensional strength at the direction of the parallel TBC/substrate interface because of its columnar structure (Miller, 1989). TBC could easily crack when bending.

The spalling occurred when the deflection of the interface cracked into the TBC coat at the edges of the buckle. Whether a buckle either continues to propagate or fractures the TBC, which results in a spallation, depends on the ratio of the fracture toughness of the interface,  $\Gamma_i$  and the TBC coat,  $\Gamma_{TBC}$  as well as the mode mixity (He et al. 1998). That TBC spalled at the edge of the buckle rather than propagation along the direction perpendicular to the edge reveals that the interface was relatively tough in this case.

The propagation rate of the buckle can be measured by image subtracting (Figure 6.14). Time is assumed as 0 corresponds to the monument when the first image was taken. The images following the first one were subtracted by the first image and the size of shadow front of the propagation direction at each image was the propagation distance at that time. The two branches of the buckle were monitored. The propagation distances as a function of time was plotted in Figure 6.16. Both buckling branches grew at a relatively stable growth rate of  $\sim 1.46 \mu\text{m}/\text{min}$ .

The surface temperatures as a function of time were also monitored during TBC buckling and spalling (Figure 6.16). The surface temperatures at three small areas were measured. Area 1 was as a reference spot with no buckling, while Area 2 was the front of

the buckle at the beginning; Area 3 was the buckled area, which would spall later on. The surface temperature of Area 2 gradually rose when the buckling grew into this area and then decreased with time. The surface temperature at Area 3 shows the temperature steeply rose at TBC spalling. The surface temperature changes revealed the strain energy in TBCs transformed to heat energy while buckle and spallation occurred. The buckling was a gradual processing while the spalling happened suddenly.

Figure 6.17 shows a 3-demensional surface temperature profile and corresponding thermal wave image. The surface temperature on the buckle was much higher than the temperature at the non-buckle area.

## 6.5 SUMMARY

Following is a summary of the thermal wave imaging investigation of TBCs damage and failure processing:

1. Thermal wave imaging as a non-destructive and non-contact evaluation method shows a high potential to monitor the health of thermal barrier coatings. The large interface delamination can be captured by thermal wave imaging, while micro-decohesion can be represented by the higher thermal signal amplitude (surface temperature) of TBCs during imaging.
2. Manufacturing defects, such as impurity on metallic surface, could lead to interface separations in TBCs. However, the interface separations did not grow or buckle during thermal cycling until the last cycle to failure.

3. No major delamination was observed by thermal wave imaging in normal TBC specimens. Thermal signal amplitude (surface temperature) of TBCs increased with thermal cycling due to thermal contact resistance induced by interface damages.
4. The TBCs failed due to the buckling and spalling of TBC. The critical buckling size can be obtained by measuring the width of the buckle between the two straight sides. It was about 4.27 mm. The buckle propagated in "telephone cord" morphology at the rate of 1.46mm/min. Cracks formed at the middle of the buckles along the propagation direction. The spallation of TBC occurred between the cracks and edge of the buckle.
5. The buckling and spalling of TBC resulted in a rise of thermal signal amplitude due to energy release.

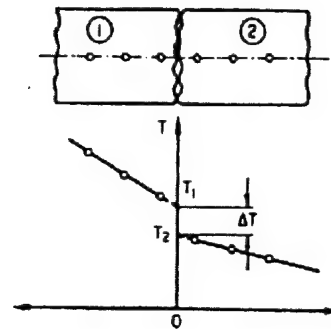


Figure 6.1 schematically shows the temperature drop at an interface due to thermal contact resistance

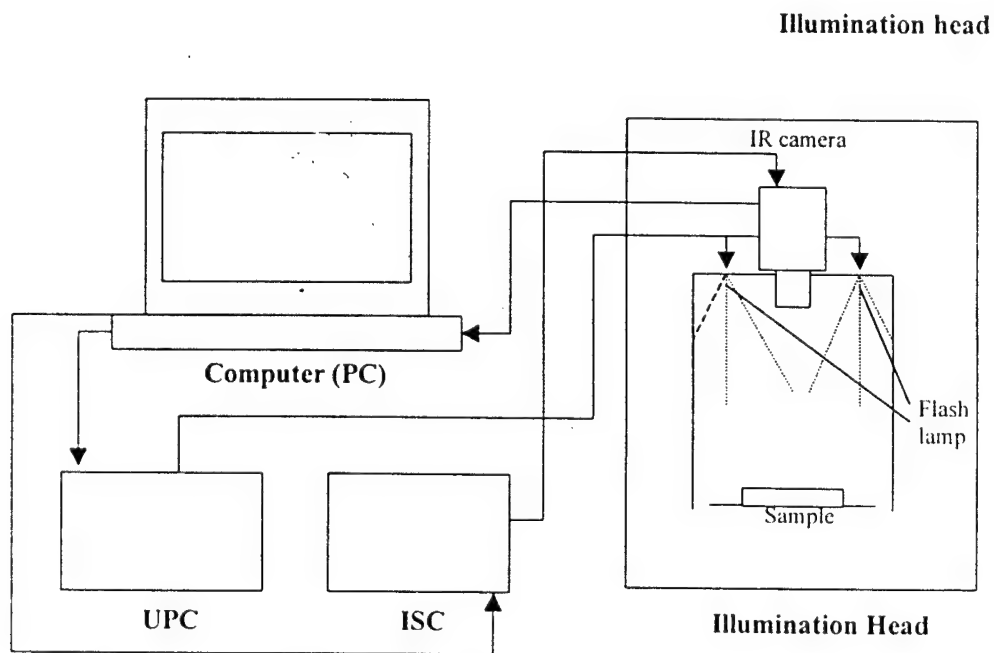


Figure 6.2 shows the working principle of thermal wave imaging

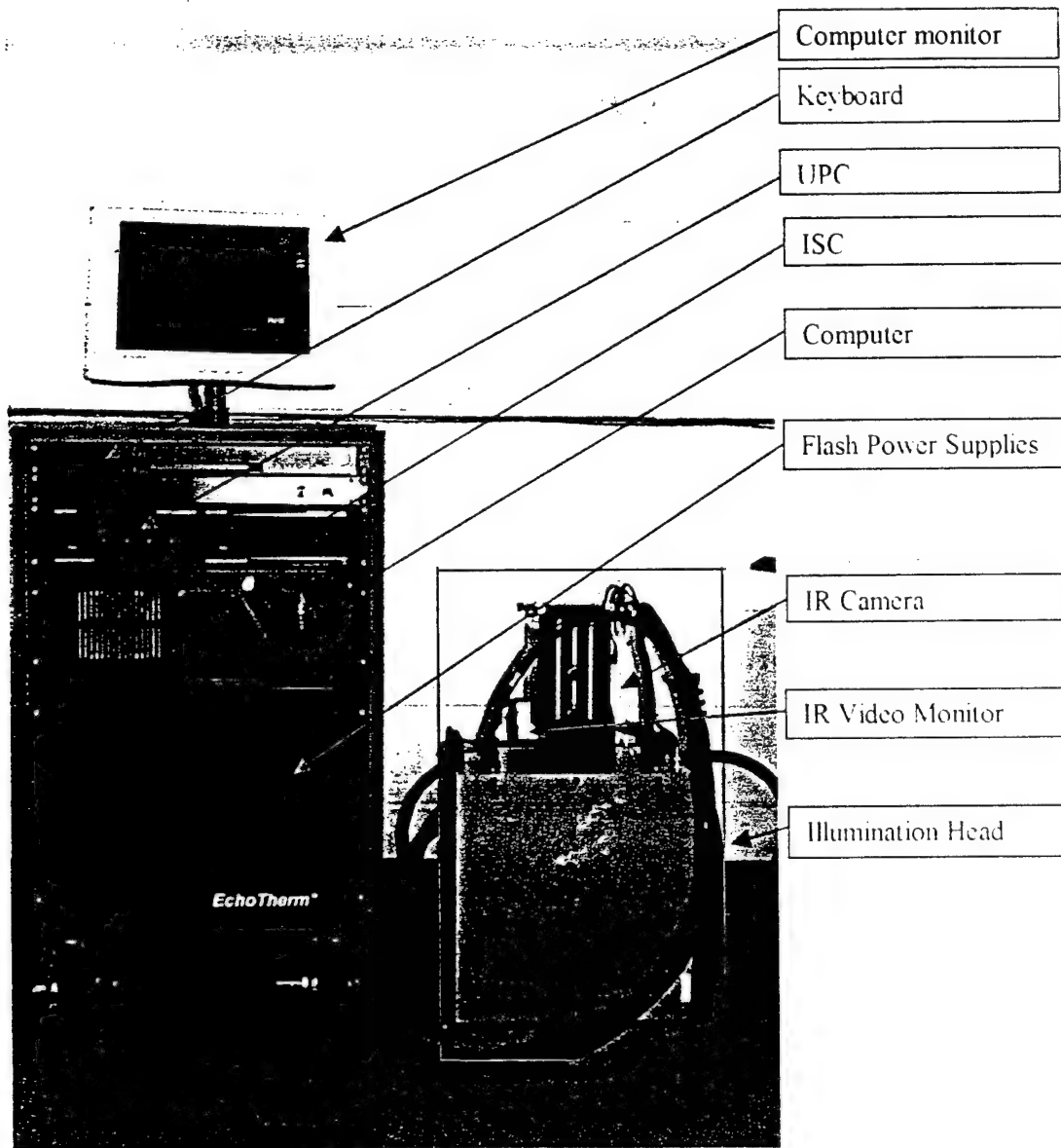


Figure 6.3 shows a typical Echothermal® 32 System Hardware

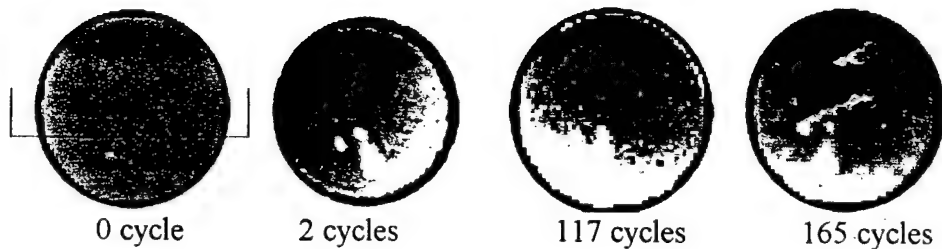


Figure 6.4 shows thermal wave images of TBCs at 0, 2, 117 and 165 cycles. Two interface separations formed after cycles and they did not grow with continuous thermal cycling.

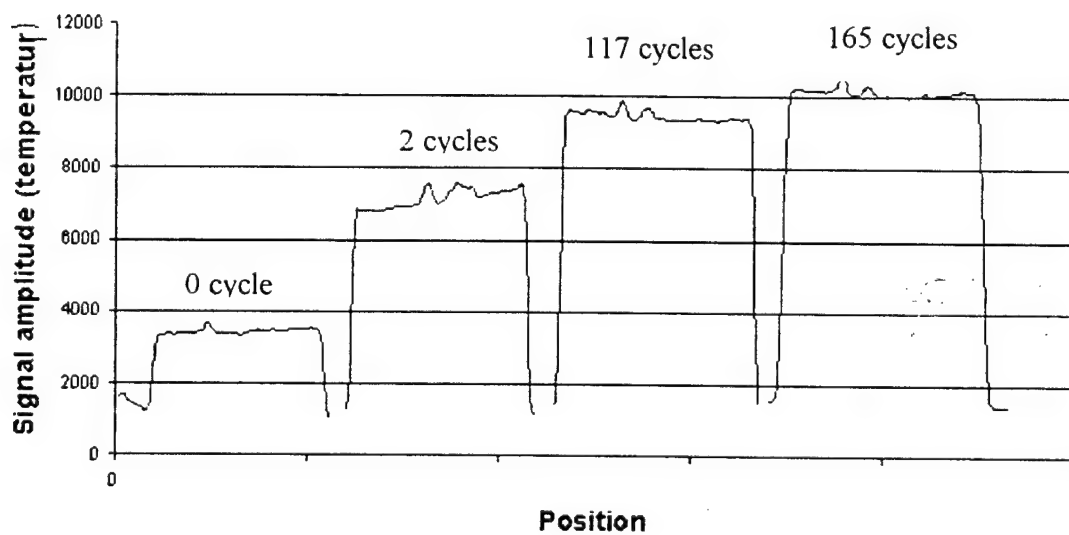


Figure 6.5 shows signal amplitude (temperature) vs position of the specimen at 0, 2, 117 and 165 cycles (sama specimen as in figure 6.4). The analysis position is shown in figure 6.4. The undulations of the curves are led by interface separation.

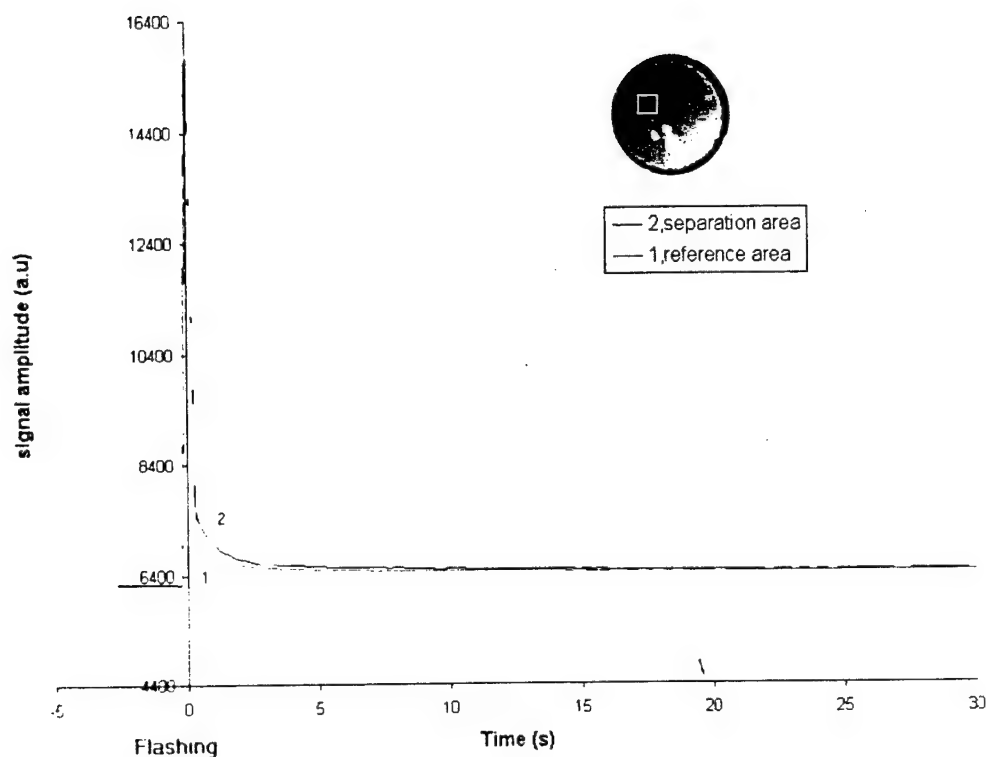


Figure 6.6 shows the surface temperature as a function of time during thermal wave imaging. Curve 1 and curve 2 represent the surface temperature of reference area and interface separation area, respectively.

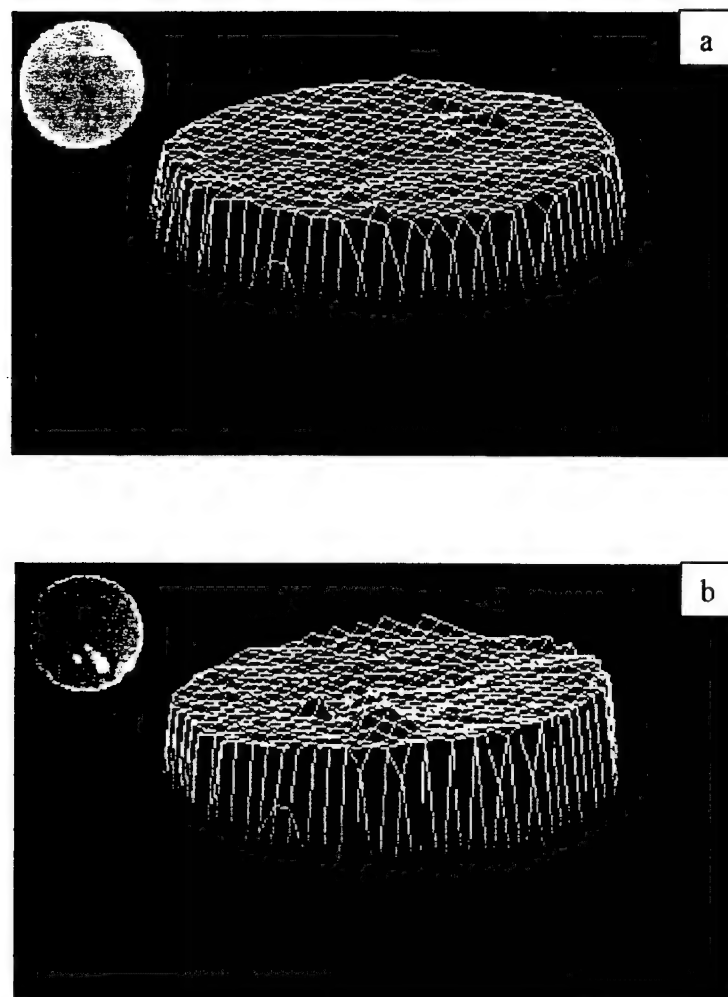


Figure 6.7 shows 3-D surface temperature distributions of the specimen with manufacturing defects at 0 cycle (a) and 2 cycles.

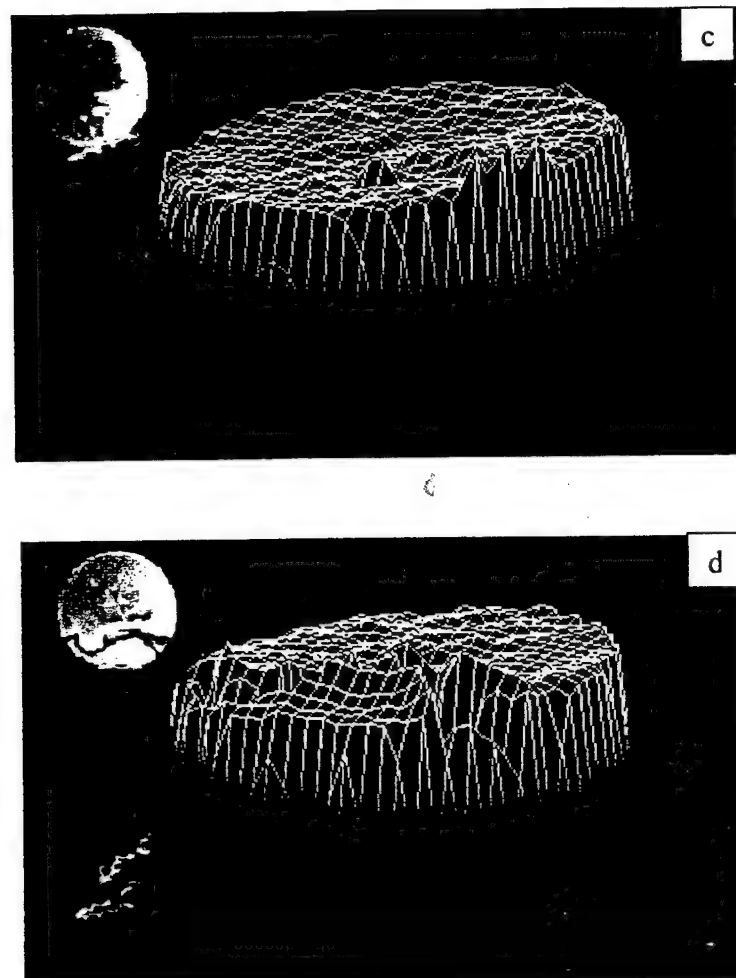


Figure 6.7 (continual) shows 3-D surface temperature distributions of the specimen with manufacturing defects at 165 cycles (a) and failure at 167 cycles.

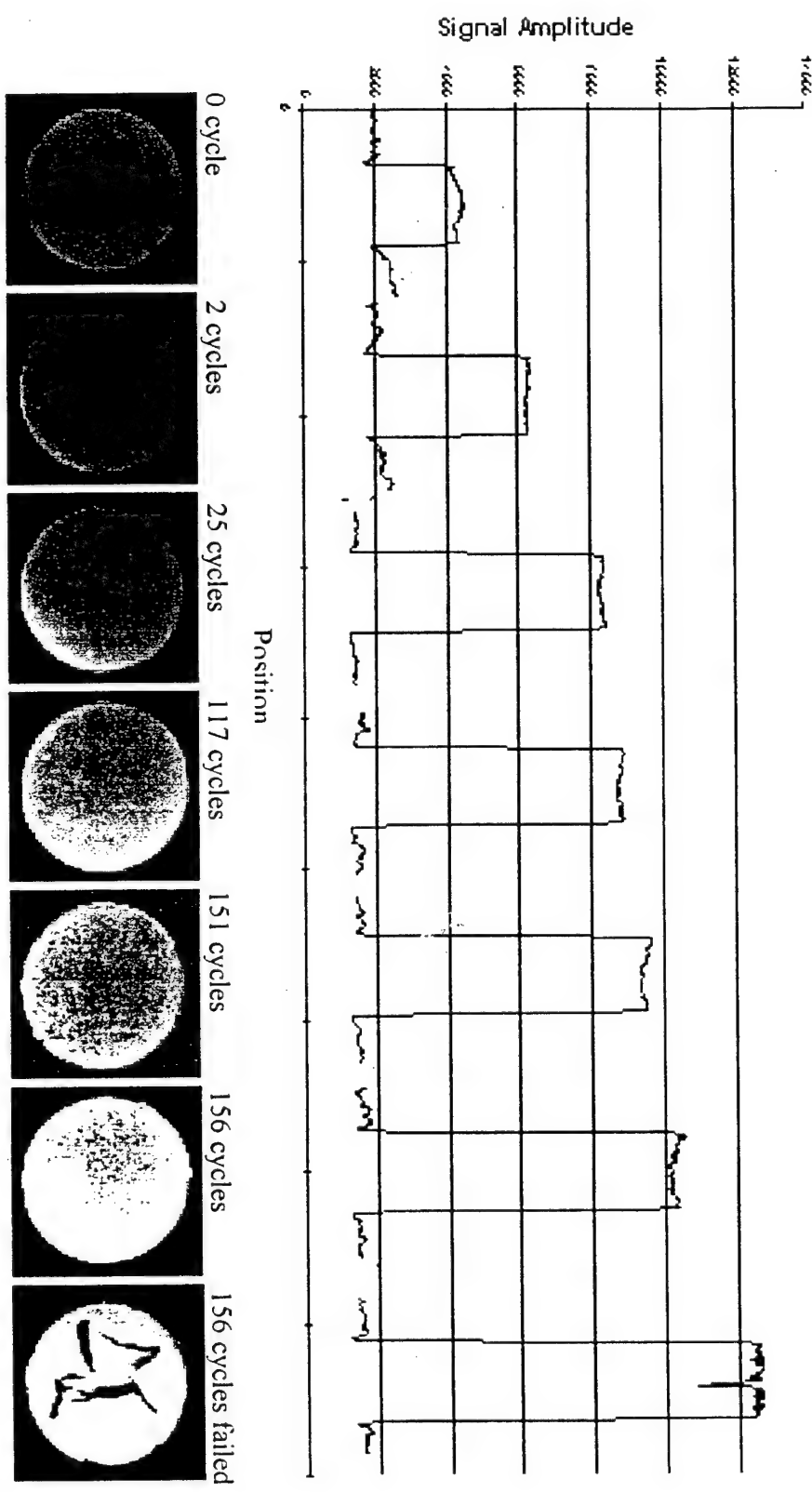


Figure 6.8 shows thermal wave images and corresponding surface temperature profile plots of a same TBCs specimen at 0, 2, 25, 117, 151, 156 and after failure at 156 cycles. The images shows there was not any delamination in the specimen until failure, while the surface temperature increased with thermal cycling.

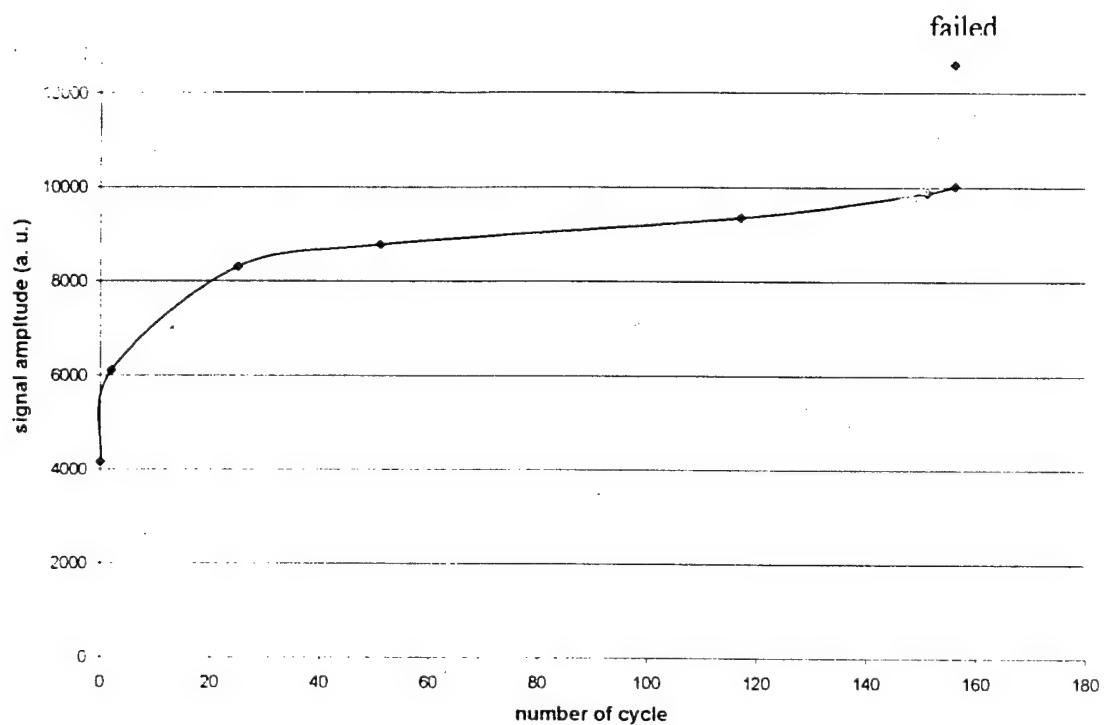


Figure 6.9 shows a relationship of thermal wave signal amplitude (surface temperature) and number of thermal cycles.

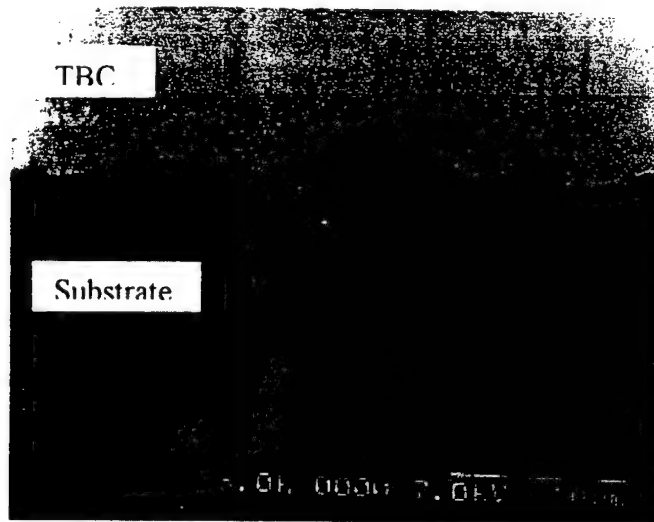


Figure 6.10 shows a cross section of an as-coated specimen. The TBC coat was perfectly bonded to substrate by an oxide layer.

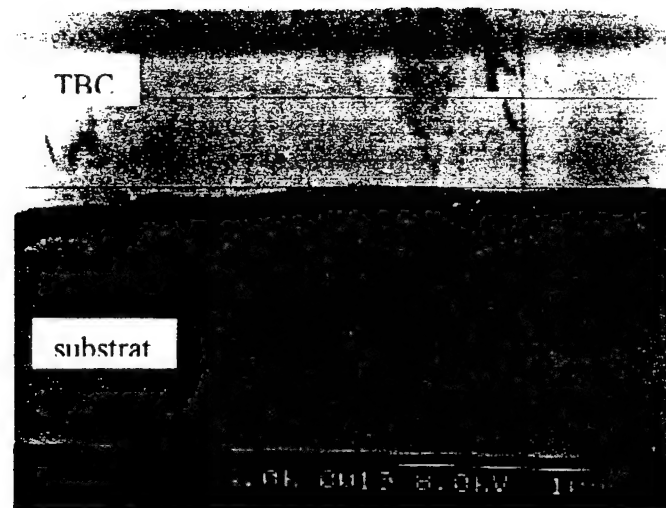


Figure 6.11 shows damages formed in oxide layer between TBC and substrate after only 2 thermal cycles.

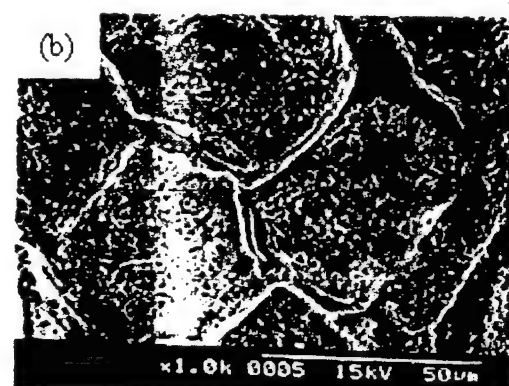


Figure 6.12 shows the damage evolution in oxide layer with increased thermal cycles  
(a) 0 cycle; (b) 25 cycles (c) 75 cycles; (d) 150 cycles.

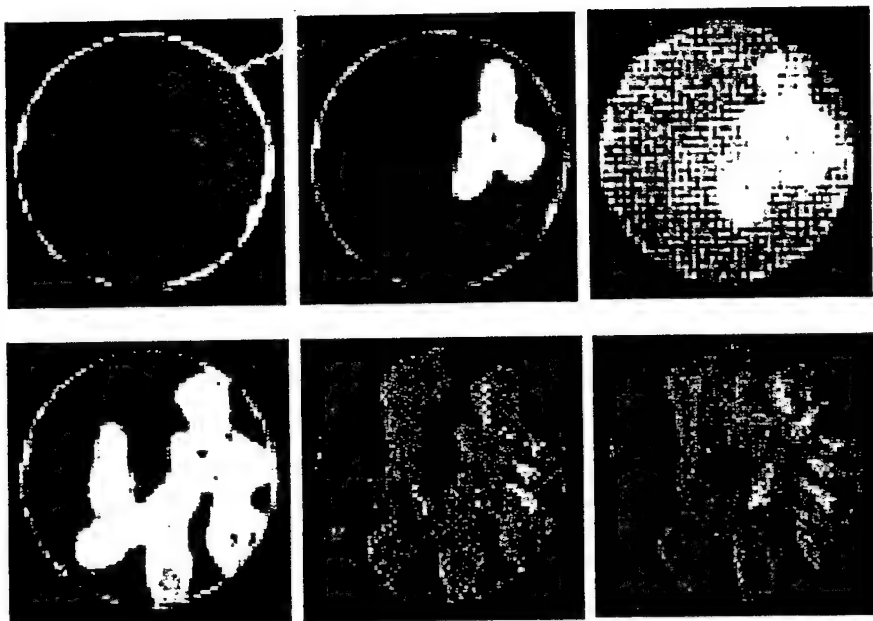


Figure 6.13 shows a processing of a separation propagating, buckling and spalling. A small separation formed during cooling. It grew and buckled at room temperature. The buckle propagated along the direction with higher curvature. Cracks formed at middle of buckle. Spalling occurred when interface crack deflected into TBC coat.

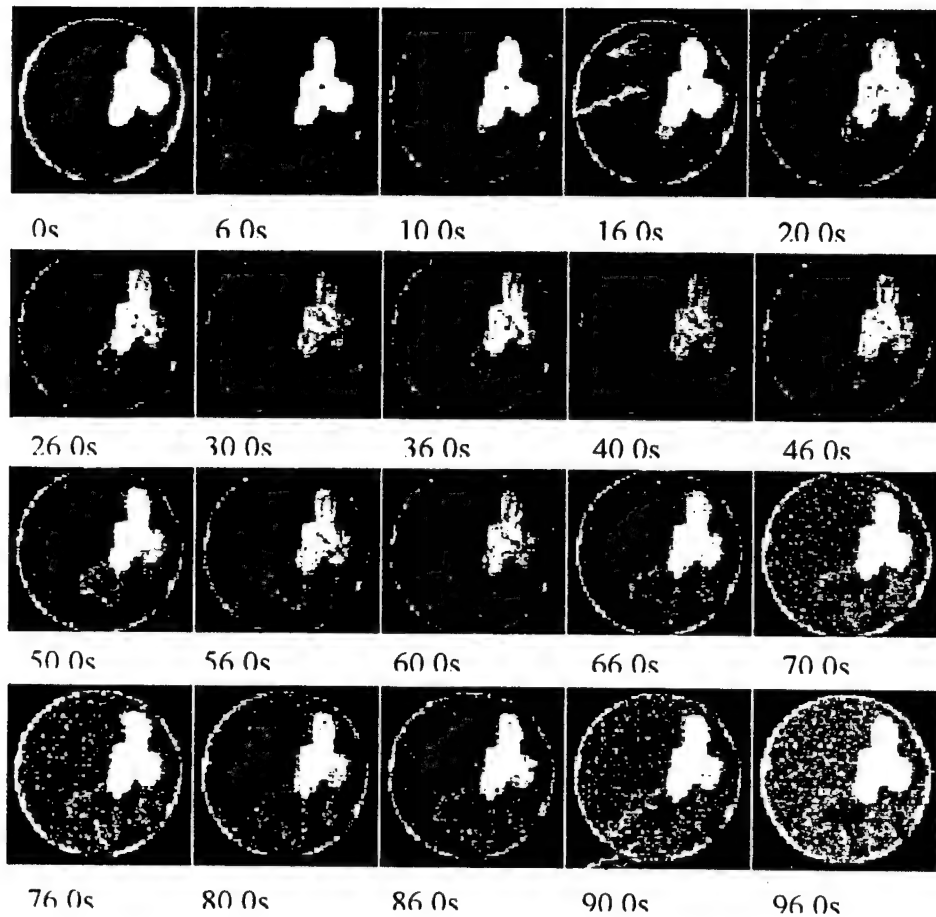


Figure 6.14 shows a series of subtraction images. The buckle propagation rate was monitored

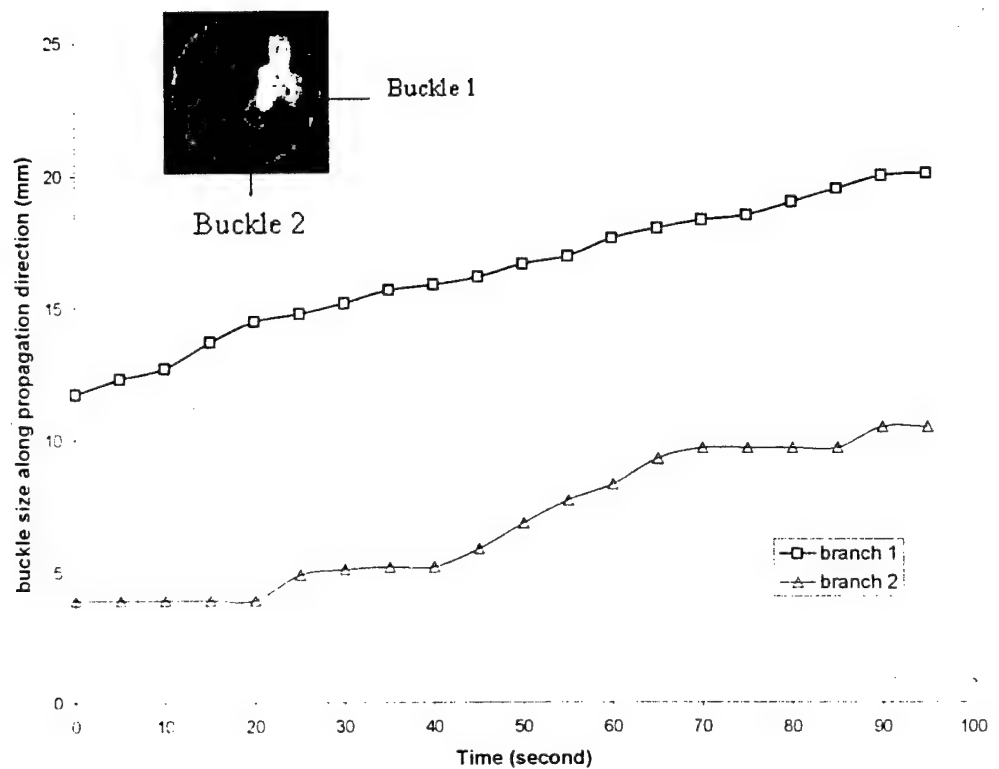


Figure 6.15 shows the buckling propagation distance as a function of time at room temperature (image showing in figure 6.14). The two branches of the buckle were monitored

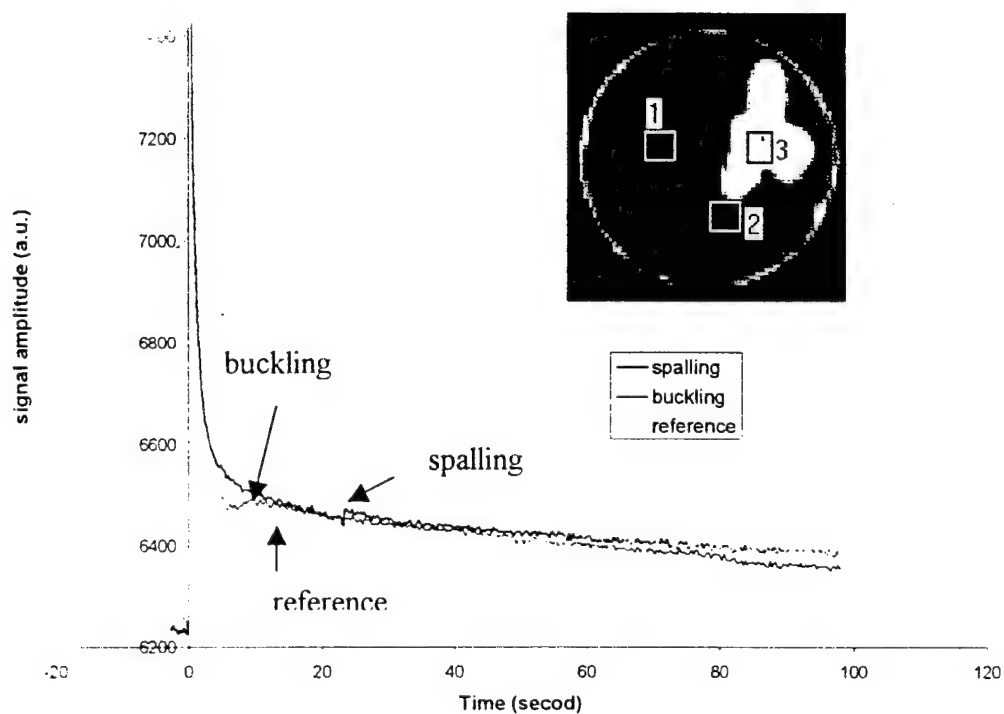


Figure 6.16 shows surface temperature feature at buckling area, spalling area and reference area, respectively. TBC buckling and spalling caused surface temperature rises.

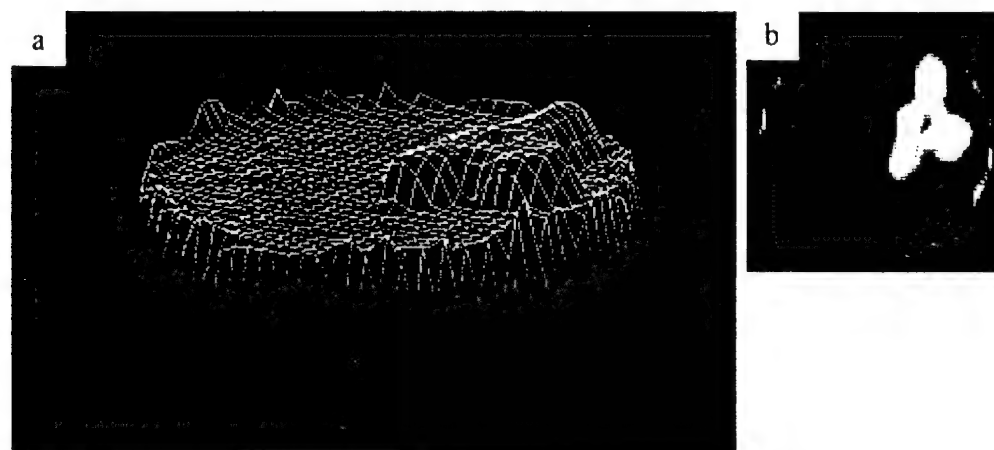


Figure 6.17 shows a 3-demensiun temperature distribution profile (a) with corresponding thermal wave image (b). The buckling area had a higher surface temperature.

## 7.0 FAILURE MODES

Spallation of TBC will result in a component temperature well in excess of the design temperatures. This can, consequently, result in a rapid and severe degradation of the component properties. The TBCs should be very dependable, so that a component can be designed with guaranteed protection of the TBCs. Currently most research on EB-PVD thermal barrier coatings are focused on failure mechanisms. Few papers published focus on the improvement of performance of TBCs. Even though a functional gradient coating concept has been proposed, it is difficult to practice. In this chapter, failure mode of TBCs and the key factors that influence its performance will be discussed. A proposal will be given to improve TBC performance by vacuum heat treatment.

## 7.1 EXPERIMENTAL PROCEDURE

Type 1 specimens were used to determine the lifetime of TBC and failure mode at various thermal tests. Vacuum heat treatment experiments were performed in vacuum quartz tube with a flat bottom, which kept heat from transforming to the TBCs specimen (Figure 7.1).

## 7.2 RESULTS AND DISCUSSION

The lifetimes of TBCs are shown in Table 7.1 at 4 thermal test conditions. The result reveals that the thermal test condition significantly influenced the total lifetime held at peak temperature. Thermal cycling led a shorter lifetime of TBCs, and higher frequency thermal cycling resulted in the shortest lifetime; for example, thermal test C for only 10 minutes holding at peak temperature. Reducing the peak temperature from 1177 °C to 1135 °C could increase the TBCs spallation lifetime by a factor of 2.4. More systematic work on the effect of peak temperature on TBCs spallation lifetime has been done by Nusei et. al. (1998). They showed that the peak temperature has a major effect on lifetime. According to finite element analysis, a 42 °C difference of peak temperature does not apparently influence the residual stresses in the TBC system. However the diffusivity of oxygen and aluminum highly dependents on temperature (see chapter 3). The oxidation dynamic controlled by diffusion of oxygen and aluminum also changes significantly if temperature changes. The results reveal that the diffusion of oxygen and aluminum is one of the major factors that influences the lifetime of TBCs.

Figure 7.2 shows the failure modes of TBC at the three thermal test conditions (thermal test A, B, and C), respectively. The results have shown that the holding time significantly affected the failure mode. The TBC finally failed by buckling, buckling propagation and spallation at long holding time thermal test (isothermal). The TBC buckled, and the buckle propagated through the whole sample at 45 minutes holding time thermal cycling. The buckle finally arrested at the edge of the sample but did not spall. Cracks formed in TBC coat during buckling propagation. The TBC failed by the whole

TBC piece separating from the substrate at the shortest holding time (10 minutes) thermal cycling.

Buckling and spallation failure consists of three steps (He, Evans and Hutchinson 1998).

(a) Buckling initiation: Buckling is explicitly defined. For films subject to biaxial compression, the critical separation radius,  $b_b$ , for axisymmetric buckling at stress (Evans et al, 1998), is:

$$b = 1.11h \sqrt{\frac{E}{(1-\nu^2)\sigma}} \quad (7.1)$$

where  $\sigma$  is the residual compressive stress,  $h$  is the thickness of coating,  $E$  and  $\nu$  are Young's modulus and Poisson's ratio of the coating.

(b) Buckle propagation: Buckle propagation inherently involves mode mixity effects and associated changes in the interface toughness. Here,  $\psi$  is used to represent the mixity angle with 0 referring to mode I and  $\pi/2$  to mode II. For a typical case, wherein the interfaces exhibit higher mode II than mode I toughness, there is a 'critical' stress  $\sigma_p$  above which buckles always propagate. This is given for axisymmetric buckles by:

$$\sigma_p = \phi \sqrt{\frac{E\Gamma_i^0}{1-\nu}} h \quad (7.2)$$

where  $\nu$  is Poisson's ratio,  $\Gamma_i^0$  the mode I interface toughness and  $\phi$  about 2.5.

(c) Spallation: The deflection of the interface crack into the film occurs in accordance with a kinking criterion. This criterion is dictated by the mode mixity and the ratio of the interface toughness,  $\Gamma_i^0$ , to that of the film,  $\Gamma_o$ . The spalling, rather than

continued propagation along the interface, happens when the interface is relatively tough. Then, the spall size is the same as the buckle size. At smaller interface toughness, the buckle propagates along the interface before it spalls.

According to the buckling and spallation theory, the interface toughness governs the failure mode and lifetime of TBCs. From failure modes at different thermal test profiles, it can be revealed that a shorter holding time of the thermal test profile led to lower interface toughness and shorter lifetime because cracks at the TBC/TGO interface and microcracks in the TGO layer formed at the shorter holding time thermal test (see chapter 4). Therefore, high fracture toughness of TGO layer and interfaces will help the TBC system to improve its performance.

Therefore, diffusion of oxygen and aluminum, as well as the bond strength of TBC to bond coat, are critical factors that influence the performance of TBCs.

Based on this understanding, vacuum heat treatment experiments were designed for TBC performance improvement. At first, a few experiments were performed to determine TBC performance in a vacuum. Table 7.2 summarizes the test condition. The specimens had been thermal tested at isothermal or thermal cycling condition before being thermal cycled in a vacuum. Various thicknesses of the TGO layer and damages (cracks and voids) were created at the pre-thermal test: 50 hours at test A, 120 hours at test A and 50 cycles at test B. Results of vacuum thermal cycling have shown the TBCs could not fail without further oxidation. Even serious damage existed in the TBCs for example, after isothermal exposure at 1177 °C for 120 hours, which the 80% lifetime had run out, the TBC could survived for another 200 thermal cycles at test B without failure.

Micrographs of TBC surface after thermal cycling in a vacuum are shown in Figure 7.3(a). Cracks in the TBC coat were formed during thermal cycling in a vacuum. The picture of a cross section of the sample (Figure 7.3(b)) shows that those cracks were always associated with grain boundaries of bond coat layer, which were similar with the cracks seen in TGO. It indicates that the bond coat grain boundary sliding led to crack TGO and extent to TBC layer (see chapter 4). Cracks at top TBC surface have not been seen in any normal thermal test specimen.

The microstructure of the top ceramic coat also changed after vacuum heat treatment. Figure 7.4 shows microstructures of the top and cross section of TBC before vacuum heat treatment. The top ceramic coat was a columnar structure with inter-columnar spacings before vacuum sintering treatment. However, the ceramic coating became porous, and the intercolumnar spacings were sintered and bridged to each other (Figure 7.5). The loss of intercolumnar spaces will result in an increase in in-plane elastic moduli of the TBC coating (Subramanian, 1999). The higher in-plane moduli of the top coat makes the TBC less susceptible to buckling at small initial debonds or interface flaws and therefore can have a beneficial influence in suppressing buckling-delamination (Choi, et al., 1999).

The Figures 7.6 and 7.7 show the comparison of microstructures of the cross-section of 50 B cycles in air and 50 B cycles in air plus 340 B cycles in vacuum. The thickness of TGO in both specimens was the same. However, there were voids and microcracks (Figure 7.6) in TGO or at interfaces before vacuum heat treatment, while TGO shows a high-density layer, few voids or microcracks could be found in TGO layer and interfaces. The figure 7.7 shows the crack where the TGO/bond coat interface had been partially healed. The alumina did not lose its adhesion to the bond coat even after

In normal thermal cyclic test, the alumina would lose during sample metallurgraph after 50 thermal cycles (see chapter 3). It indicates that adhesion to TBC and bond coat layers after vacuum heat treatment.

Voids and microcracks formed because of continued oxidation and thermal cycling. The research on alumina have shown that voids and microcracks in alumina could be healed at high temperatures by sintering (Flinn, et al., 2000, Moffatt, et al., 1996). Moffatt et al. (1996) also investigated the effect of oxidation on crack healing during high temperature annealing of alumina, and proposed that cracks can be healed by high temperature annealing of both alumina and an alumina composite, but oxidation at the crack plan reduced the effectiveness of the healing mechanism. Therefore, vacuum heat treatment is one of the methods to heal cracks in alumina. Sintering will result in an increase of alumina density by healing voids and cracks and result in an increase of strength and modulus (Flinn et. al., 2000). Therefore, the TGO layer becomes tougher and stronger after vacuum heat treatment.

The bond of both interfaces (TBC/TGO and TGO/bond coat) was improved by vacuum heat treatment. Most interfacial damages were healed during vacuum heat treatment. Figure 7.6 shows an interfacial crack where the TGO/bond coat had been partially healed. As per the binary phase diagram of  $ZrO_2$ - $Al_2O_3$ ,  $ZrO_2$  solid solution can be formed up to & mol%  $Al_2O_3$  even at  $1885^{\circ}C$  (Smyser, et al., 1996). Schilbe (2000) studied substrate alloy element diffusion in thermal barrier coatings. It was proposed that the increase of contact time between TBC and bond coat by TGO could result in the increase of intermixing or solid solutioning in TBC/TGO interface. Brickey and Lee (2000) investigated the microstructure of TBC/TGO interface in thermal barrier coatings

by transmission electron microscopy. They found that there were two bands of oxide grains adjacent to the TBC coat in thermal cycled specimens. One band contained  $ZrO_2$ -rich dispersoids the same as in an as-coated specimen; the other band was a  $ZrO_2$ -free layer. Porosity and cracks were associated with the interface between the bands. Therefore, the high density  $ZrO_2$ - $Al_2O_3$  solid solution layer can form at vacuum heat treatment without further damage by continuous oxidation.

The aluminum and oxygen transport mechanisms can be affected due to the  $Zr$  and  $Y$  diffusion to alumina layer (Huntz, 1988). The author reviewed the works of the effects of active elements (including  $Zr$  and  $Y$ ) on diffusion of aluminum and oxygen in alumina, which had been done by researchers. The results indicated that the active elements could modify the microstructure of alumina and influence the transport processes in alumina. He concluded that the beneficial effect of active elements is due to a decrease of either oxygen or aluminum diffusion.

The damages (voids and microcracks) in TBCs can be healed and diffusion mechanisms can also be changed at further oxidation process because of mass transport during the vacuum heat treatment. The TBCs will obtain benefits from the heat treatment.

In order to verify the improvement of performance of TBCs by vacuum heat treatment, a thermal cyclic test was performed after vacuum heat treatment. To prevent cracks in a TBC layer during vacuum heat treatment, a specimen after 50 cycles of thermal test B in air was vacuum isothermally sintered for 50 hours at 1177 C. Figure 7.8 shows no crack was formed after vacuum isothermal sintering. The specimen then was thermal cycled at thermal test B in air. The result shows the specimen can last another 237 cycles. The total life time exposure at peak temperature in air is 215.25

hours, which is an increase of ~68% in lifetime compared with non-vacuum heat treatment specimen.

### 7.3 SUMMARY

According to current results, the following can be summarized:

1. Interface fracture toughness plays a key role on TBCs failure mechanism. It governs the failure mode and lifetime of TBCs.
2. Without continued oxidation, TBCs cannot fail by thermal load alone.
3. Vacuum heat treatment can build a tougher interface and strengthen the TGO layer due to sintering.
4. The transport mechanisms of aluminum and oxygen at further oxidation change due to Zr and Y diffusion into alumina layer during vacuum heat treatment. The lifetime of TBCs can be significantly increased about 65% through the vacuum heat treatment.

TABLE 7.1 Lifetime of thermal barrier coatings at various thermal test conditions

Test type	No. of cycles in air	Total time at peak T in air (hrs)	Failure
A	1	170*	Yes
B	170	127.5*	Yes
C	550	91.7*	Yes
D	430	322.5	Yes

\* is average date from at least 5 specimens

TABLE 7.2 The effect of vacuum heat treatment on the lifetime of TBCs

Sample No.	No. of cycles in air	Total time at peak T in air (hrs)	No. of cycles in vacuum	Total time at peak T in vacuum (hrs)	No. of cycles in air after post-treatment	Failure
1	50 B*	37.5	340 B	255	0	No
2	1 A	50	150 B	112.5	0	No
3	1 A	120	200 B	150	0	No
4	50 A	37.5	1 A	50	237 B	Yes

A: test was performed at thermal test profile A in figure 2.2

B: test was performed at thermal test profile B in figure 2.2



Figure 7.1 shows a TBC specimen in a vacuum quartz tube with a flat bottom.

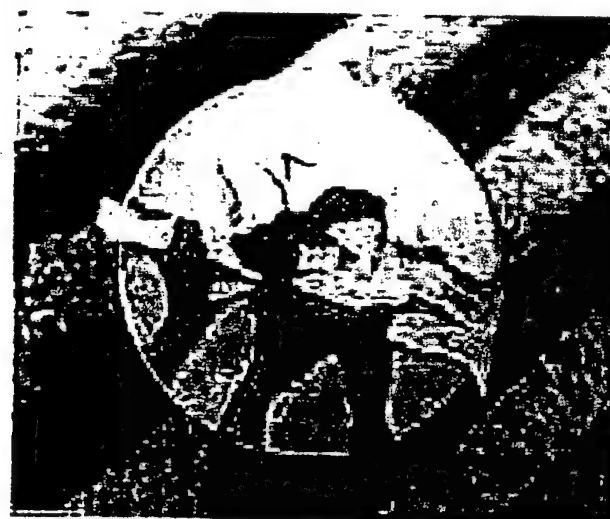


Figure 7.2(a) shows TBC failure mode at thermal test A (isothermal test).

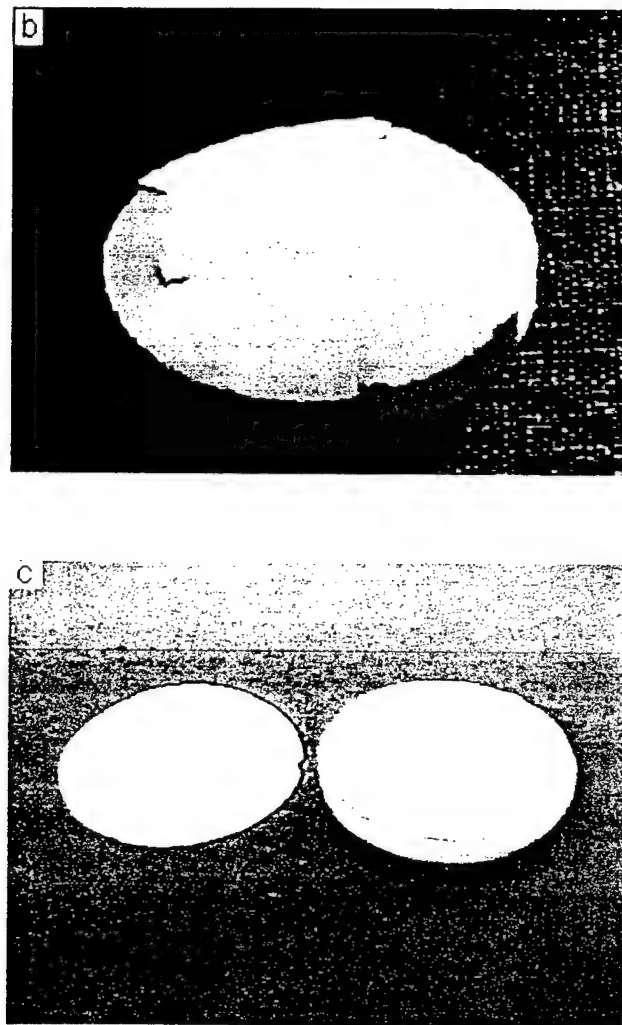


Figure 7.2 (continue) shows TBC failure mode at thermal test B (b) and thermal test C (c).

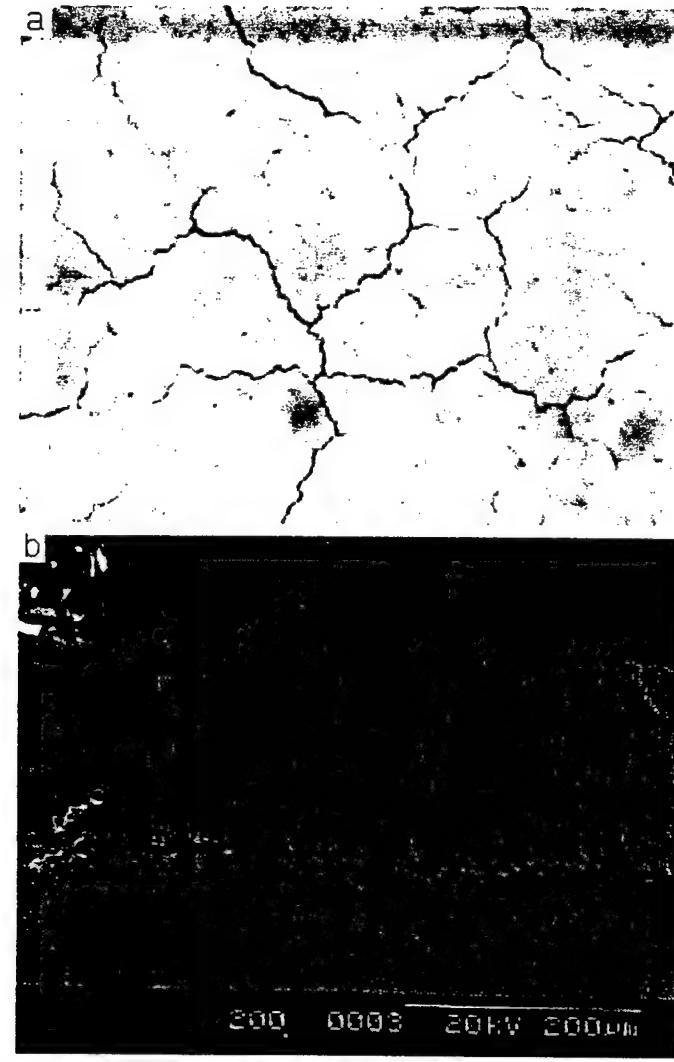


Figure 7.5 shows top surface and cross section of TBC after 50 cycles in air and 340 cycles in vacuum at thermal test B. TBC cracks always associated with grain boundaries of the bond coat.

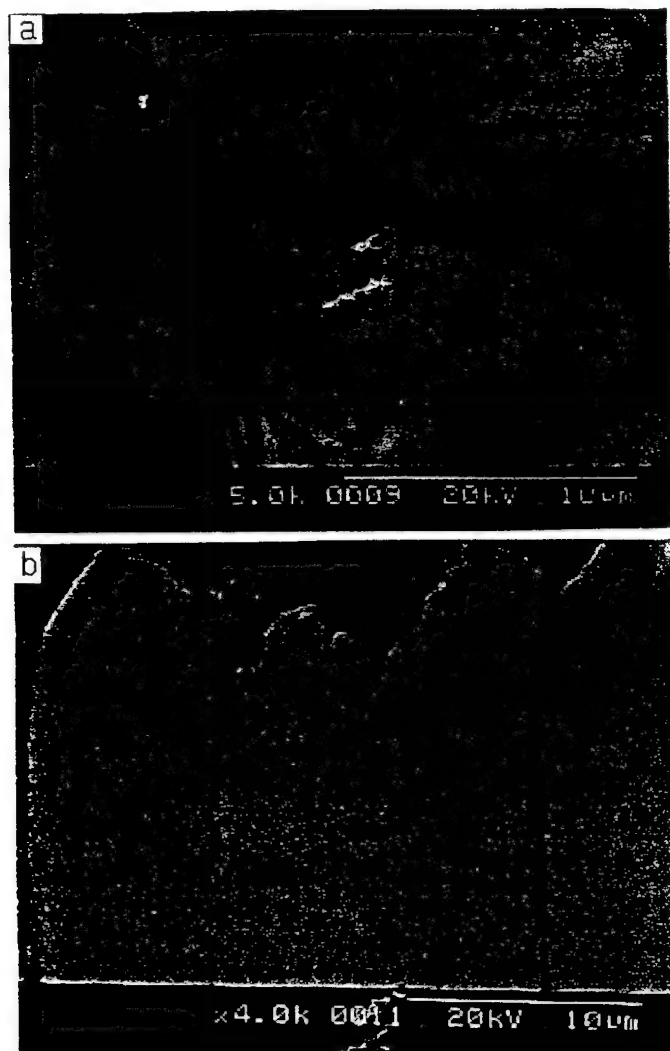


Figure 7.3 shows top (a) and cross section(b) of TBC after 50 cycles at thermal test B.

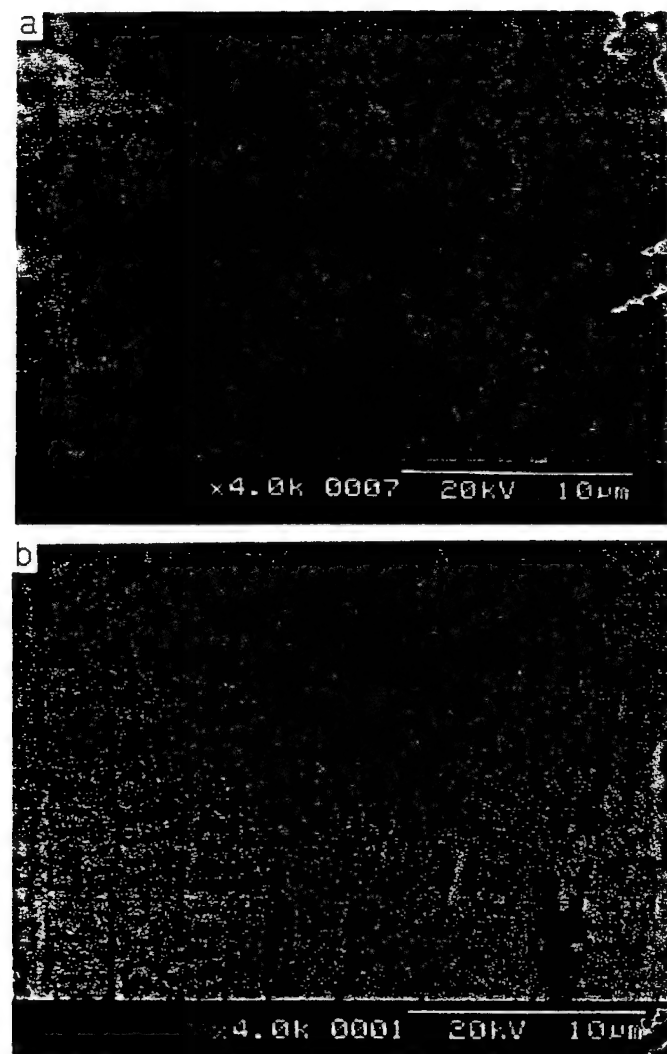


Figure 7.4 shows top (a) and cross section of TBC after 340 cycles at thermal test B in vacuum



Figure 7.6 shows there were many voids and microcracks in TGO and interfaces after 50 cycles in air at thermal test B.

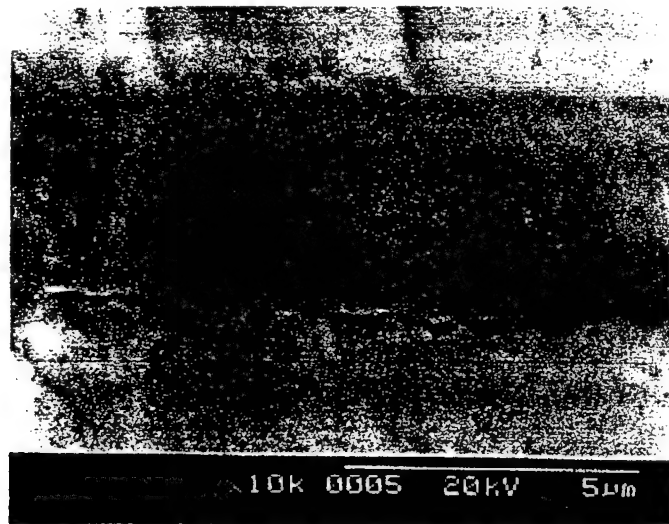


Figure 7.7 shows TGO layer and interfaces of TBC/TGO and TGO/bond coat after 50 cycles in air and 340 cycles in vacuum at thermal test B.

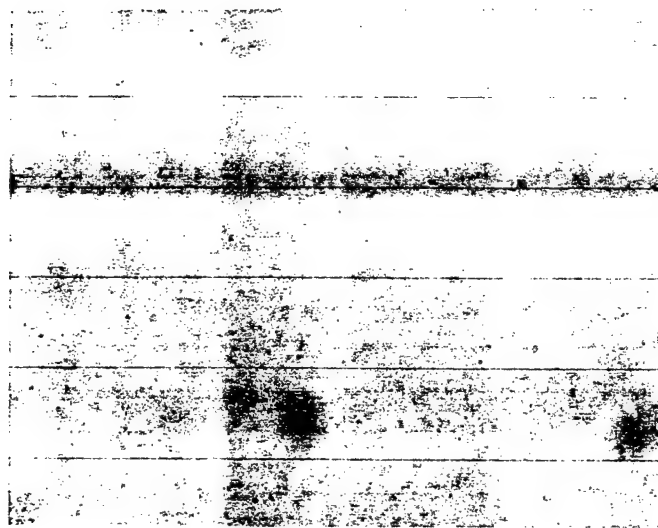


Figure 7.8 shows the top surface of TBC after isothermal vacuum heat treatment. There is no crack at TBC surface.

## 8.0 SUMMARY AND CONCLUSIONS

### 8.1 SUMMARY

The following conclusions can be reached based on current results:

(1) The optical microscope, a scanning electron microscope and x-ray diffraction methods were utilized to characterize the microstructure and damage in the TBC system. The microstructure of the bond coat changed from high aluminum concentration  $\beta$ -(Ni, Pt)Al phase, which has a very good oxidation resistance, to  $\beta$ -(Ni, Pt)Al plus  $\gamma'$ -(Ni, Pt)<sub>3</sub>Al dual phase microstructure due to oxidation and interdiffusion between the bond coat and the substrate during the thermal test in air. The volume fraction and distribution of precipitates  $\gamma'$ -(Ni, Pt)<sub>3</sub>Al strongly depended on thermal test conditions. Higher temperature and higher frequency thermal cycling resulted in higher volume fraction of  $\gamma'$ -(Ni, Pt)<sub>3</sub>Al. The microstructure change influenced the oxidation behaviors of the bond coat. Less protective oxide (Ni-rich) formed on  $\gamma'$ -(Ni, Pt)<sub>3</sub>Al due to depletion of aluminum, and the oxide scale on  $\gamma'$ -(Ni, Pt)<sub>3</sub>Al had less adhesion to the bond coat.

(2) The TGO layer and bond coat was subjected to high residual radial stresses during cooling from oxidation temperature. The high residual stress exceeded the yielding strength of the bond coat and caused plastic deformation of the bond coat. The minimum temperature at thermal cycling influenced the mechanism of plastic deformation of the bond coat and damage feature in the TGO layer. When specimens were cooled from the peak temperature of thermal cycling to the temperatures 200 °C or room temperature, which are below BDT temperature (~300 °C) of the bond coat (NiAl), the grain boundaries slid and induced the stress concentration at the TGO/bond coat

stress concentration at the TGO/bond coat interface resulted in cracking. When specimens were cooled down to 500 °C at thermal cycling, which is the temperature of NiAl, the bond coat (NiAl) performed ductile deformation under the high residual stress. The cyclic deformation of the bond coat resulted in a rumpling of the bond coat and oxide. The cyclic thermal load led microcracking in the TGO layer during thermal cycling. The evolution of cracking, microcracking and surface rumpling in TGO layer resulted in local loss in adhesion of the coating during thermal cycling.

(3) Thermal wave imaging technique as non-destructive and non-contact method was successfully used to monitor the health of TBC. The results reveal that there was no major delamination in TBC specimens during thermal tests, instead of increase of thermal signal amplitude of TBCs with number of cycles. When the increase of the thermal signal amplitude tended to be very slow, it indicated TBC was close to failure. The increase of the thermal signal amplitude contributed to an increase of thermal contact resistance in the TBC system, which was induced by micro-decohesions at interfaces. The TBC finally failed by buckling and spalling. However, buckling, buckle propagation and spalling performed in very short time compared to the whole lifetime of TBC. It was proposed that the buckling and spalling processes were final events at thermal tests and did not control the lifetime of TBC. The formation and evolution of micro-decohesion was the key failure mechanism of TBC for long term thermal cycling.

## REFRENCES

ABAQUS, 1998, Hibbit, Karlsson and Sorensen, Inc.

Ali, M. Y., Nusier, S. Q. and Newaz, G. M., 2001, "Transient Residual Stress Calculation In a Four-Layer Cylindrical TBC-Superalloy System", the International J. of Solids and Structures, pp.3329-3341.

Ali, M. Y., Chen, X. and Newaz, G. M., 2001, "Thermally Grown Oxide (TGO) Development Under Thermal Cycling-II: Implication Of Failure Mode", submitted to J. materials science.

Balmain, J., Loudjani, M.K. and Huntz, 1997, "Microstructural And Diffusional Aspects Of The Growth Of Alumina Scales On Nial", Materials science and engineering, Vol. A224, pp.87-100.

Basuki, E., Crosky, A. and Gleeson, B., 1997, "Interdiffusion Behaviour In Aluminide-Coated Rene 80H At 1155 °C", Materials science and engineering", Vol. A224, pp. 27-32.

Bayer, F., Fischer-Buhner, J. and Gottstein, G., 1999, "Mechanisms Of Compatible Deformation In Nial-Bicrystals", Intermetallic, pp. 467-78.

Birks, N., Meier, G. H. and Pettit, F. S., 1994, "Forming Continuous Alumina Scales to Protect Superalloys" JOM., Dec. pp42-46.

Birks, N., Meier, G. H. and Pettit, F. S., 1987, "High-Temperature Corrosion Resistance", J. of Metals. Dec., pp. 28-31.

Brickey, M.R., and Lee, J.L., 2000, "Structural And Chemical Analysis Of A Thermal Grown Oxide Scale In Thermal Barrier Coatings Containing A Platinum-Nickel – Aluminide Bondcoat", Oxidation of metals, Vol. 54, pp.237-254.

Chan, K. S., 1997, "A Mechanics-Based Approach to Cyclic Oxidation", Metallurgical and Materials Transactions A, Vol. 28, pp. 411-422.

Chang, G. C., Phucharoen, W., and Miller, R. A., 1987, " Finite Element Thermal Stress Solutions for Thermal Barrier Coatings", Surface and Coatings Technology, 32, 307-325.

Chen, X. and Newaz, G. M., 2001, "Oxidation and Damage of EB-PVD Thermal Barrier Coating under Thermal Cycling" J. of Materials Science letter, pp. 93-95.

Chen, X. and Newaz, G. M., 2001, "Damage Assessment In Thermal Barrier Coatings Using Thermal Wave Imaging Technique", surface and coatings technology, submit.

Chaudhury, Z.A., Newaz, G.M., Nusier, S.Q., Ahmed, H. and Thomas, R.L., 1999, "Chronological Evaluation Of Interfacial Damage In TBC Due To Thermal Cycling", J. material science, Vol. 34, pp. 2475-2481.

Chaudhury, Z.A.; Newaz, G.M.; Nusier, S.Q.; Ahmed, T., 1997, "Interfacial Damage In EB-PVD Thermal Barrier Coatings Due To Thermal Cycling", Materials Science & Engineering, Vol. A231, pp. 34-41

Choi, S.R., Hutchinson, J.W., and Evans, A.G., 1999, "Delamination Of Multiplayer Thermal Barrier Coatings", Mechanics of materials, Vol. 31, No. 7, pp. 431-447.

Christensen, R. J., Lipkin, D. M. and Clarke, D. R., 1996, " Nondestructive Evaluation Of The Oxidation Stresses Through Thermal Barrier Coatings Using C3+ Piezospectroscopy", Appl. Phys. Lett. Vol. 69, No. 9, pp. 3354-3356.

Doychak, J., 1994, "Oxidation Behavior Of High-Temperature Intermetaalics",  
Intermetallic Compounds: Vol. 1, Principles, Edited by Westbrook, J. H. and Fleischer,  
R.L., Published by Jone Wiley & Sons Ltd., pp. 977-991.

Ebrahimi, F., and Hoyle, T.G., 1997, "Brittle-Toductile Trasition In Polycrystalline  
Nial", Acta Meter. Vol. 45, pp. 4193-4204.

Evans, A. G., Crumley, G. B. and Demaray, R. E., 1983, "On the Mechanical Behavior  
of Brittle Coatings and Layers," Oxidation of Metals, Vol. 20, No. 5/6,pp. 193-214.

Evans, A. G., and Hutchinson, J. W., 1984, " On the Mechanics of Delamination and  
Spalling in Compressed Films", Int. J. Solids and structures, Vol. 20, No. 5, pp. 455-466.

Evans, A. G. He, M. Y., and Hutchinson, J. W., 1997. "Effect of Interface Undulations  
on the Thermal Fatigue of Thin Films and Scales on Metal Substrates", Acta Mater. Vol.  
45, No. 9. pp. 3543-3554.

Evans, A. G. Hutchinson, J. W., and He, M. Y., 1999, " Micromechanics Model for  
the Detachment of Residually Compressed Brittle Films and Coatings" Acta Mater.. Vol.  
47. No. 5. Pp. 1513-1522.

Evans, A.G., Hutchinson, J.W. and Wei, Y., 1999, "Interface Adhesion: Effects Of  
Plasticity And Segregation", Acta mater., Vol. 47, pp4093-4113.

Evans, H. E., 1989, "Cracking and Spalling of Protective Oxide Layers." J. of  
Materials Science and Engineering, A120, pp. 139-146.

Favro, L. D.. Kuo, P. K., and Thomas, R. L., "Real-Time Thermal Wave Imaging".  
Non-Destructive Evaluation (NDE). Volume II, PTR Prentice Hall, Englewood Cliffs.

NJ07632.

Felten, E. J. and Pettit, F. S., 1976, "Development, Growth and Adhesion of  $\text{Al}_2\text{O}_3$  on Platinum-Aluminum Alloys", Oxidation of Metals, Vol. 10, No. 3, pp. 189-223.

Flinn, B.D., Bordia, R.K., Zimmermann, A. and Rodel, J., 2000, "Evolution Of Defect Size And Strength Of Porous Alumina Dueing Sintering", J. of the European ceramic society, Vol., 20, pp. 2561-2568.

Fu, L., Khor, K.A., Hg, H.W. and Teo, T.N., 2000, "Non-Destructive Evaluation Of Plasma Sprayed Functionally Graded Thermal Barrier Coatings", Surface and Coatings Technology Vol.130, pp. 233.

Gell, M., Vaidyanathan, K. Barber, B. Cheng, J. and Jordan, E. 1999, " Mechanism Of Spallation In Platinum Aluminide/Electron Beam Physical Vapor-Deposited Thermal Barrier Coatings" Metallurgical and Materials Transactions A Vol. 30A, Feb. pp427-435.

Gell, M., Jordan, K. Vaidyanathan, McCarron, K., Barber, Y.H., Sohn and Tolpygo, V.K.. 1999, "Bond Strength, Bond Stress And Spallation Mechanisms Of Thermal Barrier Coatings", Surface and coatings technology, Vol. 120-121, pp. 53-60.

Gobel M., Rahmel, A., Schutze, M., Schorr, M. and Wu, W.T., 1994, "Interdiffusion Between The Platinum-Modified Aluminide Coating RT 22 Nickel-Based Single-Crystal Superalloys At 1000 And 1200 C", Materials at high temperatures, Vol. 12, pp.301-309.

Gomes, J.F., Monteiro, J.M. and Vaz, M.A.P., 2000, "NDI Of Interfaces In Coating Systems Using Digital Interferometry", Mechanics of materials, Vol. 32, pp. 837-843.

He, M. Y., Evans, A. G. and Hutchinson, J. W., 1998, "Effects of Morphology on the Decohesion of Compressed Thin Films" Materials Science and Engineering A245 pp. 168-181.

Janssen, M.M.P., 1973, "Diffusion In The Nickel-Rich Part Of The Ni-Al System At 1000 C To 1300 C; Ni<sub>3</sub>Al Layer Growth, Diffusion Coefficients, And Interface Concentrations", Metallurgical transaction, Vol. 4, pp.1623-1633.

Jones, R. L. 1996, " Thermal Barrier Coatings", Metallurgical and Ceramic Protective Coatings, Edited by Stern, K. H., Published by Chapman & Hall, London. ISBN 0 412 54440 7. pp213.

Kakac, S. and Yener, Y., 1993, " Heat Conduction", Taylor & Francis, pp. 58.

Lee, H., and Neville, K., 1967, "Handbook Of Epoxy Resins", Published by McGraw-Hill, Inc.

Luikov, A.V., 1968, "Analytical Heat Diffusion Theory", Academic press New York and London, pp. 381.

Maldague, X.P.V., 1994, "Infrared Methodology And Technology", Gorgon and breach science publishers, pp.49.

Martinsons, C. and Heuret, M., 1998, "Recent Progress In The Measurement Of The Thermal Properties Of Hard Coatings", Thin solid films, Vol. 317, pp. 455.

Miere, S. M. Nissley, D. M. and Sheffler, K. D. 1991 "Thermal Barrier Coating Life Prediction Model Development" NASA-CA-1891111.

Meier, S. M., Nissley, D. M., Sheffler, K. D. and Cruse, T. A., 1992, "Thermal Barrier Coating Life Prediction Model Development," J. of Engineering for Gas Turbines and Power, Vol 114, pp. 258-263.

Miller, R. A. and Lowell, C. E., 1993 "Failure Mechanisms of Thermal Barrier Coating Exposed to Elevated Temperature," Thin Solid Film, Vol. 99, pp. 265-270.

1984, "Oxidation Based Model for Thermal Barrier Coating Life", J. of  
Society, Vol. 67, No.8, pp. 517-521.

1993, Acta Metall Mater, Vol. 41, pp.649.

Miracle, D.B., 1991, Acta Metall Mater, Vol. 37, pp.1457.

Moretto, P. and Bressers, J., 1996, "Thermo-Mechanical Fatigue Degradation Of A  
Nickel-Aluminide Coating On A Single-Crystal Nickel-Based Alloy", J. of materials  
science, pp. 4817-4829.

Mumm, D.R., and Evans, A.G., 2000, "On The Role Of Imperfections In The Failure  
Of A Thermal Barrier Coating Made By Electron Beam Deposition" Acta Mater., Vol.  
48, pp. 1815-1827.

Nesbitt, J. A. and Barrett, C. A., 1993, "Predicting the Oxidation-Limited Lifetime of  
NiAl". Structure Intermetallics edited by Darolia, R. et. al., published by MSA, pp.601-  
609.

Nesbitt, J. A.. Vinarcik, E. J., Barrett, C. A. and Doychak, J., "Diffusion Transport And  
Predicting Oxidative Failure During Cyclic Oxidation Of Nial Alloys", Materials Science  
and Engineering, A153, pp. 561-566.

Newaz, G. M., Nusier, S. Q. and Chaudhury, Z. A., 1998, " Damage Accumulation  
Mechanisms in Thermal Barrier Coatings", ASME J. Materials and Technology, April,  
pp.149-153.

Newaz, G., 2000, "Progress Report On Effect Of Damage Processes On Spallation Life  
In Thermal Barrier Coatings", Presented to AFOSR, Grant # F49620-98-1-0390.

Noebe, R.D.. Cullers, C.L. and Bowman, R.R., 1992, J. Mater. Res., Vol. 7, pp. 605.

Nusier, S. Q., and Newaz, G. M., 2000 "Growth Of Interfacial Cracks In A TBC/Superalloy System Due To Oxide Volume Induced Internal Pressure And Thermal Loading" International J. of Solids and Structures" No. 37. Pp. 2151-2166.

Nusier, S. Q., and Newaz, G. M., 1998 "Analysis Of Interfacial Cracks In A TBC/Superalloy System Under Thermalmechanical Loading", J. engineering for gas turbines and power, Vol. 120, pp. 819.

Nusier, S.Q., Newaz, G. M., Chaudury, Z. A., Chen, X. and Khan, J. M., 1998, "Effect of Different Thermal Cycles on TBC Spallation Lifetime", paper presented at IMECE'98, Anaheim, CA.

Nusier, S. Q., 1997 "Damage Accumulation and Failure in Thermal Barrier Coatings", Ph.D. dissertation. Wayne State University. Detroit, MI.

Nusier, S.Q., Newaz, G. M. and Chaudury, Z. A., 2000, "Experimental And Analytical Evaluation Of Damage Processes In Thermal Barrier Coatings", International Journal of Solids and Structures. Vol.37, Issue 18, pp. 2495-2506.

Pettit, F.S., 1967, "Oxidation Mechanisms For Nickel-Aluminum Alloys At Temperatures Between 900 °C And 1300 °C", Transactions of the metallurgical society of AIME, Vol.. 239, pp. 1296-1305.

Sergo, V and Clarke, D. R., 1998 "Observation of Subcritical Spall Propagation of a Thermal Barrier Coating", J. Am. Ceram. Soc., Vol. 81. No. 12. Pp.3237-3242.

Rickerby, H.M., Sridhar, N., and Abbas, N.M., 1998, "Failure Mechanism Of A Thermal Barrier Coating Systm On A Nickel-Base Superalloy", J. of materials science, Vol. 33, pp. 681-686.

Robert E. Reed-Hill, 1973, "Physical Metallurgy Principles, Second Edition", Published by D. VAN NOSTRAND COMPANY, New York, pp.378-427.

Roul, B.K., Sahu, D.R., Mohanty, S., Mohanty, B.C., and Singh, S.K., 2001, "Sintering Of Al-Zr Based Oxide Ceramics Using Thermal Plasma", Materials chemistry and physics, Vol. 67, pp. 151-156.

Schaeffer, J., Kim, G.M., Meier, G.H. and Pettit, F.S., 1988, "The Effects Of Precious Metals On The Oxidation And Hot Corrosion Of Coatings", The Role Of Active Elements In The Oxidation Behaviour Of High Temperature Metals And Alloys, edited by Lang, E., Published by Elsevier Applied Science, pp. 231-267.

Schilbe, J.E., 2000, "Substrate Alloy Element Diffusion In Thermal Barrier Coatings". Surface and coatings technology, Vol. 133-134, pp35-39.

Smialek, J., 1978, "Oxide Morphology And Spalling Model For Nial", Metallurgical transaction, Vol. 9A, pp.309-320.

Smigelskas, A.D., and Kirkendall, E.O., 1941, Trans. AIME, Vol., pp.130.

Soechting, F. O., 1995, "A Design Prospective on Thermal Barrier Coating", Proceedings of Conference, March 27-29, NASA Lewis Research Center, Ohio, pp.1-15.

Suo, Z., 1995, "Wrinkles of the Oxidation Scale on an Aluminum-Coating Alloy at High Temperature", J. of Mechanics of Physics and Solids, Vol. 43, No. 6, 829-846.

Tolpygo, V.K., and Clarke, D.R., 2000, "Spalling Failure Of Alumina Film Grown By Oxidation. II. Decohesion Nucleation And Growth", Materials science and engineering, Vol. A278, pp. 151-161.

Tolpygo, V.K., and Clarke, D.R., 2000, "Surface Rumpling Of A (Ni, Pt)Al Bond Coat Induced By Cyclic Oxidation", *Acta Mater.* Vol. 48, pp. 3283-3293.

Tien, J. K. and Pettit, F. S. 1972 " Mechanism of Oxidation Adherence on Fe-25Cr-4Al(Y or Sc) Alloys" *Metallurgical Transactions*, Vol. 3. Jun. pp. 1587-1599.

Unal, O., Mitchell, T.E. and Heuer, A.H., 1994, "Microstructures of Y<sub>2</sub>O<sub>3</sub>-Stabilized ZrO<sub>2</sub> Electron Beam Phsical Vapor Deposition on Ni-Base Superalloy", *J. of American Ceramic Society*, Vol. 74, pp. 1310-1320.

Wang, J.S. and Evans, A.G., 1999, "Effects Of Strain Cycling On Buckling, Cracking And Spalling Of A Thermally Grown Alumina On A Nickel-Based Bond Coat", *Acta mater.*, Vol. 47, pp. 699-710.

Wang, J.S. and Evans, A.G., 1999, "Measurement And Analysis Of Buckling And Buckle Propagation In Compressed Oxide Layer On Superalloy Substrates", *Acta Mater.*, Vol. 46, pp. 4993-5005.

Wright, P.K., and Evans, A.G., 1999, "Mechanisms Governing The Performance Of Thermal Barrier Coatings", *Current Opinion In Solid State And Materials Science*, No. 4, pp. 255-265.

Zhu, D. and Miller, R. A. 1996, "Evaluation of Oxidation Damage in Thermal Barrier Coating Systems", NASA 1.15-107360.

Zhu, D., Miller, R.A., Nagarj, B.A., and Bruce, R.W., 2001, " Thermal Conductivity Of EB-PVD Thermal Barrier Coatings Evaluated By A Steady-State Laser Heat Flux Technique", *Surface And Coatings Technology*, Vol. 138, pp. 1-8.